

FIRST PRINCIPLES STUDY ON THE EFFECTS OF VACANCIES AND  
Mg DOPING ON THE PHYSICAL PROPERTIES OF  $\text{CuAlO}_2$ ,  $\text{AgAlO}_2$ ,  
 $\text{CuCrO}_2$ , AND  $\text{AgCrO}_2$  TRANSPARENT CONDUCTOR OXIDES

by

James A. Shook, A.S., B.S.

A thesis submitted to the Graduate Council of  
Texas State University in partial fulfillment  
of the requirements for the degree of  
Master of Science  
with a Major in Physics  
August 2018

Committee Members:

Luisa Scolfaro, Chair

Alex Zakhidov

Nikoleta Theodoropoulou

**COPYRIGHT**

by

James A. Shook

2018

## **FAIR USE AND AUTHOR'S PERMISSION STATEMENT**

### **Fair Use**

This work is protected by the Copyright Laws of the United States (Public Law 94-553, section 107). Consistent with fair use as defined in the Copyright Laws, brief quotations from this material are allowed with proper acknowledgement. Use of this material for financial gain without the author's express written permission is not allowed.

### **Duplication Permission**

As the copyright holder of this work, I, James A. Shook, authorize duplication of this work, in whole or in part, for educational or scholarly purposes only.

## **DEDICATION**

For Clyde, Fiona, Isaac, Rosie, Stella, Penny, Mia, Ricky, Julian, Zelda, and Bonnie.

## ACKNOWLEDGEMENTS

It is with much gratitude that I thank my thesis advisor, Dr. Luisa Scolfaro, for her unwavering support, deep insight, and profound patience. It is simply fact that this thesis could not have been completed without her guidance. For the many times that I was involved in a particularly challenging aspect of this work, Dr. Scolfaro's deep insights and exacting ability to portray conceptual topics in a lucid way proved indispensable. I would like to thank my thesis committee, Drs. Alex Zakhidov and Nikoleta Theodoropoulou, for their time and guidance. I would also like to thank all of the above not just for helping me to navigate the greatest work I have ever achieved, but for also making me an all-around better physicist through their lecture courses that I had the pleasure and privilege of attending – most of the time. These instructors truly inspire with the depth of not only their knowledge, but their sincere and earnest desire to see their students succeed. Additionally, I would like to thank two of Dr. Scolfaro's former students, Drs. Pablo Borges and John Petersen, who were invaluable in helping me understand the subtleties of the Vienna Ab Initio Simulation Package, as well as making me aware of all of the post-processing tools for handling the output data. My thesis would have been dead in the water had these two individuals not shared with me the experiences they had with similar problems in their own research, and what they did to move past it. Also, I would like to thank Eric Welch, for providing an excellent springboard to discuss density functional theory and the VASP code. Our discussions often provided me with perspectives on my research I may not have had otherwise. To the physics department at Texas State at-large, and namely Drs. David Donnelly, Wilhelmus Geerts, and Hunter Close, thank you for fostering such a supportive and

welcoming environment in which all of us, as students and physicists, may better ourselves. Finally, I would like to thank my mother and father, Deborah and Kevin, who's help I've needed in many ways more times than I would like to admit, and who have been there for me more times than I will ever remember.

This material is based upon work supported by, or in part by, the U. S. Army Research Laboratory and the U. S. Army Research Office under contract/grant number W911NF1510394.

## TABLE OF CONTENTS

	Page
ACKNOWLEDGEMENTS . . . . .	v
LIST OF TABLES . . . . .	ix
LIST OF FIGURES . . . . .	xi
ABSTRACT . . . . .	xvii
CHAPTER	
1. INTRODUCTION AND MOTIVATION . . . . .	1
2. THEORETICAL FUNDAMENTALS AND METHODS . . . . .	6
2.1. Crystal Structures of XTO . . . . .	6
2.2. Density Functional Theory . . . . .	10
2.2.1. Many body problem. . . . .	10
2.2.2. Hohenberg-Kohn theorem. . . . .	15
2.2.3. Hatree-Fock equations. . . . .	18
2.2.4. Kohn-Sham equations. . . . .	21
2.2.5. The exchange and correlation energy: the local density approximation (LDA), generalized gradient approximation (GGA), Hubbard correction (U), hy- brid functional, and modified Becke-Johnson (MBJ) potential. . . . .	23
2.3. Determination of the Ground State Electron Charge Density. . . . .	31
2.3.1. The projector-augmented wave (PAW) method and pseudopotentials. . . . .	31
2.3.2. The Vienna Ab Initio Simulation Package (VASP). . . . .	33
2.4. Beyond the VASP Code. . . . .	37
2.4.1. The Birch-Murnaghan equation of state. . . . .	37
2.4.2. Hole effective masses and the method of band un- folding. . . . .	39
2.4.3. Optical properties. . . . .	45
2.5. Computational Methodology . . . . .	49
2.5.1. Supercell Scheme. . . . .	52

3. STRUCTURAL, ELECTRONIC, AND OPTICAL PROPERTIES OF PURE XTO . . . . .	54
3.1. Introduction . . . . .	54
3.2. Structural Properties . . . . .	55
3.3. Electronic Properties . . . . .	62
3.4. Hole Effective Masses . . . . .	78
3.5. Optical Properties . . . . .	79
3.6. Summary of Results . . . . .	85
4. NATIVE DEFECTS IN XTO: X AND O VACANCIES . . . . .	86
4.1. Introduction . . . . .	86
4.2. Structural Properties . . . . .	86
4.3. Electronic Properties . . . . .	87
4.4. Hole Effective Masses . . . . .	100
4.5. Optical Properties . . . . .	100
4.6. Summary of Results . . . . .	110
5. MAGNESIUM IMPURITIES IN XTO . . . . .	111
5.1. Introduction . . . . .	111
5.2. Structural Properties . . . . .	111
5.3. Electronic Properties . . . . .	112
5.4. Hole Effective Masses . . . . .	118
5.5. Optical Properties . . . . .	119
5.6. Summary of Results . . . . .	121
6. CONCLUSIONS AND PERSPECTIVES . . . . .	123
REFERENCES . . . . .	127

## LIST OF TABLES

Table	Page
3.1	The optimized lattice constants of CAO using PBE. . . . . 55
3.2	The optimized lattice constants of AAO using PBE. . . . . 56
3.3	The XAO total energies normalized by the number of atoms in each unit cell, $E_{\text{tot}}/\text{atom}$ , using PBE. . . . . 58
3.4	The XCO total energies normalized by the number of atoms in each unit cell, $E_{\text{tot}}/\text{atom}$ , using PBE. . . . . 59
3.5	The 2H XTO Hubbard corrections, where $\epsilon_{\infty}$ is the static dielectric constant, $U_{\text{unscr}}$ is the unscreened Hubbard parameter in vacuum, and $U_{\text{scr}} = U_{\text{unscr}}/\epsilon_{\infty}$ is the screened Hubbard parameter in the crystal, using PBE. . . . . 61
3.6	The optimized lattice constants, $a$ and $c$ , the ratio $u = c/a$ , X-O and T-O bond lengths, $d_{\text{X-O}}$ and $d_{\text{T-O}}$ respectively, ground state bulk modulus, $B_0$ , and pressure derivative of the ground state bulk modulus, $\partial B/\partial P$ of XTO using PBE+U. . . . . 62
3.7	The high symmetry points used in the paths through the Brillouin zones of each polymorph expressed as fractional coordinates of the respective reciprocal lattice vectors. . . . . 64
3.8	The XAO band gaps using PBE, where $E_{\text{g-opt}}^{\text{ind}}$ and $E_{\text{g-opt}}^{\text{dir}}$ are the indirect and direct gaps obtained in this work, and $E_{\text{g-exp}}^{\text{ind}}$ and $E_{\text{g-exp}}^{\text{dir}}$ are the respective experimental values from the literature. . . . . 67
3.9	The direct band gaps, $E_{\text{g-dir}}^{\text{CAO}}$ and $E_{\text{g-dir}}^{\text{AAO}}$ , for CAO and AAO respectively, calculated using PBE, PBE+U, PBE+MBJ, PBE+MBJ+U, and HSE06. . . . . 68
3.10	The 2H XTO band gaps using PBE+U, where $E_{\text{g-opt}}^{\text{ind}}$ and $E_{\text{g-opt}}^{\text{dir}}$ are the indirect and direct gaps respectively. . . . . 69
3.11	The hole effective masses for XTO using the primitive cell model and PBE+U, in units of $m_e$ , the free electron mass. . . . . 78

3.12	Other theoretical hole effective masses for XTO from literature, in units of $m_e$ , the free electron mass. . . . .	79
3.13	The hole effective masses for XTO using the supercell scheme, in units of $m_e$ , the free electron mass. . . . .	79
3.14	The static dielectric constants, $\epsilon_\infty$ , and refractive indices, $n$ , in the directions a, b, and c, corresponding to the primitive lattice vectors $\mathbf{b}_1$ , $\mathbf{b}_2$ , and $\mathbf{b}_3$ , of 2H XTO modeled in the primitive cell using PBE+U. . . . .	80
4.1	The X-O and T-O bond lengths, $d_{X-O}$ and $d_{T-O}$ respectively, of X- and O- vacant XTO in the PBE+U method. . . . .	87
4.2	The hole effective masses for X- and O-vacant XTO using PBE+U, in units of $m_e$ , the free electron mass. . . . .	100
4.3	The static dielectric constants, $\epsilon_\infty$ , and refractive indices, $n$ , in the directions a, b, and c, corresponding to the primitive lattice vectors $\mathbf{b}_1$ , $\mathbf{b}_2$ , and $\mathbf{b}_3$ , of X- and O- vacant XTO modeled in the primitive cell using PBE+U. . . . .	101
5.1	The X-O and T-O bond lengths, $d_{X-O}$ and $d_{T-O}$ respectively, of Mg-doped XTO in the PBE+U method. . . . .	111
5.2	The hole effective masses for Mg-doped XTO using the supercell scheme, in units of $m_e$ , the free electron mass. . . . .	118
5.3	The static dielectric constants, $\epsilon_\infty$ , and refractive indices, $n$ , in the directions a, b, and c, corresponding to the primitive lattice vectors $\mathbf{b}_1$ , $\mathbf{b}_2$ , and $\mathbf{b}_3$ , of Mg-doped XAO in the PBE+U method. . . . .	119

## LIST OF FIGURES

Figure	Page
1.1 XTO crystal structures for the a) $\alpha$ -2H, b) $\alpha$ -3R, and c) $\beta$ polymorphs.	2
2.1 XTO unit cells. . . . .	8
2.2 XTO Brillouin zones. . . . .	10
2.3 2H XTO $2 \times 2 \times 2$ supercell. . . . .	53
3.1 Total crystal energies normalized by the number of atoms in each unit cell versus the volume of the unit cell normalized by each relaxed volume for a) CAO and b) AAO using PBE. . . . .	57
3.2 Total crystal energies normalized by the number of atoms in each unit cell versus the volume of the unit cell normalized by each relaxed volume for a) CCO and b) ACO using PBE. . . . .	60
3.3 Brillouin zone paths through the a) hexagonal, b) rhombohedral, and c) orthorhombic unit cells used in calculating the electronic band structure. . . . .	63
3.4 Band structures and DOS of the a) $\alpha$ -2H, b) $\alpha$ -3R <sub>CH</sub> , c) $\alpha$ -3R <sub>R</sub> , and d) $\beta$ CAO polymorphs using PBE, where the Fermi energy, $E_F$ , is set to zero and is defined as the maximum energy of a valence electron in the ground state. . . . .	65
3.5 Band structures and DOS of the a) $\alpha$ -2H, b) $\alpha$ -3R <sub>CH</sub> , c) $\alpha$ -3R <sub>R</sub> , and d) $\beta$ AAO polymorphs using PBE, where the Fermi energy, $E_F$ , is set to zero and is defined as the maximum energy of a valence electron in the ground state. . . . .	66
3.6 The electronic band structure for 2H CAO calculated using PBE, PBE+U, PBE+MBJ, PBE+MBJ+U, and HSE06, where the Fermi energy, $E_F$ , is set to zero and is defined as the maximum energy of a valence electron in the ground state. . . . .	68

3.7	The electronic band structure for 2H AAO calculated using PBE, PBE+U, PBE+MBJ, PBE+MBJ+U, and HSE06, where the Fermi energy, $E_F$ , is set to zero and is defined as the maximum energy of a valence electron in the ground state. . . . .	69
3.8	2H CCO band structures in the a) non-magnetic (NM), b) spin-up ferromagnetic (FM), c) spin-down ferromagnetic, d) spin-up antiferromagnetic (AFM), and e) spin-down antiferromagnetic configurations using PBE, where the Fermi energy, $E_F$ , is set to zero and is defined as the maximum energy of a valence electron in the ground state. . . . .	70
3.9	2H ACO band structures in the a) non-magnetic (NM), b) spin-up ferromagnetic (FM), c) spin-down ferromagnetic, d) spin-up antiferromagnetic (AFM), and e) spin-down antiferromagnetic configurations using PBE, where the Fermi energy, $E_F$ , is set to zero and is defined as the maximum energy of a valence electron in the ground state. . . . .	70
3.10	The electronic band structure and density of states for a) CAO, and b) AAO using PBE+U, where the Fermi energy, $E_F$ , is set to zero and is defined as the maximum energy of a valence electron in the ground state. . . . .	72
3.11	The electronic band structure and density of states for AFM a) CCO, and b) ACO using PBE+U, where the Fermi energy, $E_F$ , is set to zero and is defined as the maximum energy of a valence electron in the ground state. . . . .	73
3.12	The folded electronic band structure of the a) CAO, b) AAO, c) CCO, and d) AAO supercells using PBE+U, where the Fermi energy, $E_F$ , is set to zero and is defined as the maximum energy of a valence electron in the ground state. . . . .	75
3.13	The electronic band structure of the primitive cell (solid black lines) and the supercell in the primitive cell representation (red x's) for a) CAO, b) AAO, c) CCO, and d) ACO using PBE+U, where the Fermi energy, $E_F$ , is set to zero and is defined as the maximum energy of a valence electron in the ground state. . . . .	76
3.14	Charge density contour plots for a) CAO, b) AAO, c) CCO, and d) ACO supercells using PBE+U. . . . .	77

3.15	Frequency dependence of the a) real component of the complex dielectric function, b) imaginary component of the complex dielectric function, c) refractive index, d) extinction coefficient, e) optical conductivity, f) absorption coefficient, g) reflectivity, and e) loss function of CAO. . . . .	81
3.16	Frequency dependence of the a) real component of the complex dielectric function, b) imaginary component of the complex dielectric function, c) refractive index, d) extinction coefficient, e) optical conductivity, f) absorption coefficient, g) reflectivity, and e) loss function of AAO. . . . .	82
3.17	Frequency dependence of the a) real component of the complex dielectric function, b) imaginary component of the complex dielectric function, c) refractive index, d) extinction coefficient, e) optical conductivity, f) absorption coefficient, g) reflectivity, and e) loss function of CCO. . . . .	83
3.18	Frequency dependence of the a) real component of the complex dielectric function, b) imaginary component of the complex dielectric function, c) refractive index, d) extinction coefficient, e) optical conductivity, f) absorption coefficient, g) reflectivity, and e) loss function of ACO. . . . .	84
4.1	Charge density contour plots for a) Cu-vacant CAO, b) O-vacant CAO, c) Ag-vacant AAO, and d) O-vacant AAO $2 \times 2 \times 2$ supercells using PBE+U. . . . .	90
4.2	Charge density contour plots for a) Cu-vacant CCO, b) O-vacant CCO, c) Ag-vacant ACO, and d) O-vacant ACO $2 \times 2 \times 2$ supercells using PBE+U. . . . .	91
4.3	The electronic band structure and density of states for Cu-vacant CAO using PBE+U, where the Fermi energy, $E_F$ , is set to zero and is defined as the maximum energy of a valence electron in the ground state. . .	92
4.4	The electronic band structure and density of states for Ag-vacant AAO using PBE+U, where the Fermi energy, $E_F$ , is set to zero and is defined as the maximum energy of a valence electron in the ground state. . .	93

4.5	The electronic band structure and density of states for Cu-vacant CCO using PBE+U, where the Fermi energy, $E_F$ , is set to zero and is defined as the maximum energy of a valence electron in the ground state. . .	94
4.6	The electronic band structure and density of states for Ag-vacant ACO using PBE+U, where the Fermi energy, $E_F$ , is set to zero and is defined as the maximum energy of a valence electron in the ground state. . .	95
4.7	The electronic band structure and density of states for O-vacant CAO using PBE+U, where the Fermi energy, $E_F$ , is set to zero and is defined as the maximum energy of a valence electron in the ground state. . .	96
4.8	The electronic band structure and density of states for O-vacant AAO using PBE+U, where the Fermi energy, $E_F$ , is set to zero and is defined as the maximum energy of a valence electron in the ground state. . .	97
4.9	The electronic band structure and density of states for O-vacant CCO using PBE+U, where the Fermi energy, $E_F$ , is set to zero and is defined as the maximum energy of a valence electron in the ground state. . .	98
4.10	The electronic band structure and density of states for O-vacant ACO using PBE+U, where the Fermi energy, $E_F$ , is set to zero and is defined as the maximum energy of a valence electron in the ground state. . .	99
4.11	Frequency dependence of the a) real component of the complex dielectric function, b) imaginary component of the complex dielectric function, c) refractive index, d) extinction coefficient, e) optical conductivity, f) absorption coefficient, g) reflectivity, and e) loss function of Cu-vacant CAO. . . . .	102
4.12	Frequency dependence of the a) real component of the complex dielectric function, b) imaginary component of the complex dielectric function, c) refractive index, d) extinction coefficient, e) optical conductivity, f) absorption coefficient, g) reflectivity, and e) loss function of Ag-vacant AAO. . . . .	103
4.13	Frequency dependence of the a) real component of the complex dielectric function, b) imaginary component of the complex dielectric function, c) refractive index, d) extinction coefficient, e) optical conductivity, f) absorption coefficient, g) reflectivity, and e) loss function of Cu-vacant CCO. . . . .	104

4.14	Frequency dependence of the a) real component of the complex dielectric function, b) imaginary component of the complex dielectric function, c) refractive index, d) extinction coefficient, e) optical conductivity, f) absorption coefficient, g) reflectivity, and e) loss function of Ag-vacant ACO. . . . .	105
4.15	Frequency dependence of the a) real component of the complex dielectric function, b) imaginary component of the complex dielectric function, c) refractive index, d) extinction coefficient, e) optical conductivity, f) absorption coefficient, g) reflectivity, and e) loss function of O-vacant CAO. . . . .	106
4.16	Frequency dependence of the a) real component of the complex dielectric function, b) imaginary component of the complex dielectric function, c) refractive index, d) extinction coefficient, e) optical conductivity, f) absorption coefficient, g) reflectivity, and e) loss function of O-vacant AAO. . . . .	107
4.17	Frequency dependence of the a) real component of the complex dielectric function, b) imaginary component of the complex dielectric function, c) refractive index, d) extinction coefficient, e) optical conductivity, f) absorption coefficient, g) reflectivity, and e) loss function of O-vacant CCO. . . . .	108
4.18	Frequency dependence of the a) real component of the complex dielectric function, b) imaginary component of the complex dielectric function, c) refractive index, d) extinction coefficient, e) optical conductivity, f) absorption coefficient, g) reflectivity, and e) loss function of O-vacant ACO. . . . .	109
5.1	Charge density contour plots for Mg-doped a) CAO, b) AAO, c) CCO, and d) ACO $2 \times 2 \times 2$ supercells using PBE+U. . . . .	113
5.2	The electronic band structure and density of states for Mg-doped CAO using PBE+U, where the Fermi energy, $E_F$ , is set to zero and is defined as the maximum energy of a valence electron in the ground state. . .	114
5.3	The electronic band structure and density of states for Mg-doped AAO using PBE+U, where the Fermi energy, $E_F$ , is set to zero and is defined as the maximum energy of a valence electron in the ground state. . .	115

5.4	The electronic band structure and density of states for Mg-doped CCO using PBE+U, where the Fermi energy, $E_F$ , is set to zero and is defined as the maximum energy of a valence electron in the ground state. . .	116
5.5	The electronic band structure and density of states for Mg-doped ACO using PBE+U, where the Fermi energy, $E_F$ , is set to zero and is defined as the maximum energy of a valence electron in the ground state. . .	117
5.6	Frequency dependence of the a) real component of the complex dielectric function, b) imaginary component of the complex dielectric function, c) refractive index, d) extinction coefficient, e) optical conductivity, f) absorption coefficient, g) reflectivity, and e) loss function of Mg-doped CAO. . . . .	120
5.7	Frequency dependence of the a) real component of the complex dielectric function, b) imaginary component of the complex dielectric function, c) refractive index, d) extinction coefficient, e) optical conductivity, f) absorption coefficient, g) reflectivity, and e) loss function of Mg-doped AAO. . . . .	121

## ABSTRACT

The need for well understood, commercially available *p*-type transparent conducting oxides for incorporation into basic transparent semiconducting devices alongside their already well understood and available *n*-type counterparts for application in technologies such as solar cells and capacitive touchscreens motivates this first principles study on the effects of Cu and O vacancies and Mg doping on the intrinsically poor *p*-type character of CuAlO<sub>2</sub>, AgAlO<sub>2</sub>, CuCrO<sub>2</sub>, and AgCrO<sub>2</sub>. Density functional theory based calculations using the projector augmented-wave functions along with the generalized gradient approximation to the exchange and correlation energy as implemented by the Vienna Ab Initio Simulation Package are used to study the total crystal energy of the three known polymorphs of CuAlO<sub>2</sub> and AgAlO<sub>2</sub> in order to determine the most stable polymorph in the ground state. Additionally, three simple magnetic configurations are considered for CuCrO<sub>2</sub> and AgCrO<sub>2</sub> in the context of total energy of the ground state for the purpose of choosing a specific polymorph and magnetic configuration to be the framework within which the doped and defect systems will be studied. Different functional approaches to the exchange and correlation energies are also considered in order to accurately reproduce the structural properties and the band gap. The 2H delafossite polymorph is determined to be one of the most stable polymorphs and is the focus of this work as it is the least studied of the delafossites. The simple antiferromagnetic configuration is chosen to model magnetic effects in CuCrO<sub>2</sub> and AgCrO<sub>2</sub> due to it having one of the lowest ground state total energies and also containing the most semiconductor like behavior of the magnetic configurations considered. A  $2 \times 2 \times 2$  supercell scheme is employed to model 6.25% Cu and Ag vacancies, 3.13% O

vacancies, and 6.25% Mg doping replacing Al and Cr, from which structural properties, electronic properties, hole effective masses, and optical properties are obtained and compared to the pristine crystal in order to offer predictions on the effectiveness of the mentioned native defects and dopant on increasing the conductivity and maintaining transparency in all transparent conducting oxides studied in this work. Comparisons between the results obtained in this work and previous experimental and other theoretical results are made, when available. Many of the properties predicted here are immediately testable via experimentation.

## 1. INTRODUCTION AND MOTIVATION

Transparent conducting oxides (TCOs) are an exciting class of materials for solid state physicists and materials scientists due to their semiconducting nature and large direct band gaps of more than 3.0 eV. The applicability of TCOs to technologies such as flat panel displays, capacitive touch screens, and photovoltaic cells establishes the need for complementarity between the well documented and commercially available *n*-type TCOs and poorly-understood *p*-type TCOs. Furthermore, the demand for viable *p*-type TCOs motivates the search for a means to delocalize the O-2*p* states which result in poor electrical conductivity in *p*-type TCOs by limiting shallow acceptors and causing large hole effective masses. CuAlO<sub>2</sub>, AgAlO<sub>2</sub>, CuCrO<sub>2</sub>, and AgCrO<sub>2</sub> (XTO, X = Cu, Ag, T = Al, Cr) show promise as *p*-type TCOs due to the presence of X-3*d*/4*d* states, which hybridize with O-2*p* states and delocalize valence states close to the valence band maximum (VBM) [1].

XTO is fabricated as small crystals using either solid-state reactions [2–5] or pulsed laser deposition [6, 7] and as thin films using spin-coating via sol-gel [8, 9] or by sputtering techniques [10, 11]. Such techniques can introduce native defects in the crystal structure, such as copper and oxygen vacancies, interstitials, or on-site replacements, which can lead to significant modifications to the electronic structure (and by extension, other material properties) [12]. X vacancies are believed to be the source of *p*-type conductivity in XTO, as they act as hole donors and introduce shallow acceptor states [13]. However, the mechanisms of their formation and the full impact of these defects is still not well understood.

XTO is known to exist as three polymorphs: two delafossites ( $\alpha$ -2H with space group symmetry  $P6_3/mmc$  and  $\alpha$ -3R with space group symmetry  $R\bar{3}m$ ) characterized by planes of T atoms separated by XO<sub>2</sub> dumbbells in a hexagonal crystal structure with an ABAB(ABCABC) staking order for the 2H(3R)

phase [2–9, 11, 14, 15], and one orthorhombic ( $\beta$ ) crystal structure characterized by tetrahedral  $XO_4$  and  $TO_4$  with O commonly shared between X and T and space group symmetry [16]  $Pna2_1$ . Of these three polymorphs, illustrated [17] in Fig. 1.1, the delafossites – 3R specifically – are the most thoroughly studied. First principles calculations predict the 3R polymorph to have a lower formation enthalpy than the 2H at pressures lower than 15.4 GPa, at which point the 2H polymorph has a lower formation enthalpy, indicating a possible phase transition from the 3R to the 2H polymorph at that pressure, with mechanical instability predicted at 26.2(27.8) GPa for the 3R(2H) polymorph [18]. An irreversible phase transition from the 3R polymorph at a pressure of  $35 \pm 2$  GPa at room temperature has been observed experimentally, however, the identity of the new phase could not be determined and the 2H polymorph is not supported by the data [14]. X-ray diffraction measurements have been used to report that 3R is the most common polymorph grown during fabrication, at times with traces of the 2H polymorph in crystals as well [3].

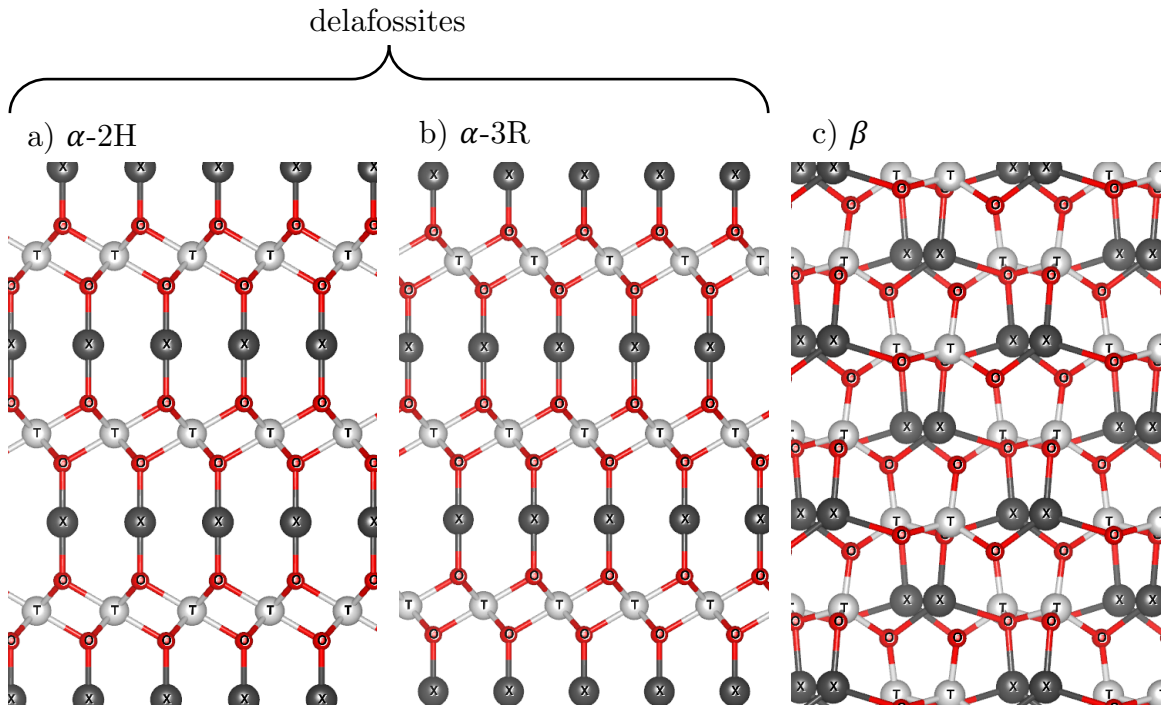


Figure 1.1: XTO crystal structures for the a)  $\alpha$ -2H, b)  $\alpha$ -3R, and c)  $\beta$  polymorphs.

3R CuAlO<sub>2</sub> is the most well understood of the mentioned TCOs, with an indirect band gap ranging from 1.65 – 2.99 eV [7, 10, 13, 19–22], a direct (optical) band gap of 3.01 – 3.9 eV [7, 10, 13, 19–22], hole mobility of 3 cm<sup>2</sup> V<sup>-1</sup> s<sup>-1</sup> in the  $a - b$  plane and 0.11 – 0.12 cm<sup>2</sup> V<sup>-1</sup> s<sup>-1</sup> perpendicular to the plane [13], a Seebeck coefficient [7, 19] of  $2.14 \times 10^{-6} - 6.7 \times 10^{-4}$  V K<sup>-1</sup>, and a Hall coefficient of 0.23 cm<sup>3</sup> C<sup>-1</sup>, which gives a hole concentration [7] of  $2.7 \times 10^{19}$  cm<sup>-3</sup>. Although Liu *et al.* report a lower hole concentration of  $3.52 \times 10^{16}$  cm<sup>-3</sup> for 3R CuAlO<sub>2</sub>, that concentration increases to  $1.79 \times 10^{18}$  cm<sup>-3</sup> upon 6.25% Mg doping (replacing Al), and gives a conductivity of  $8.0 \times 10^{-2}$  Ω<sup>-1</sup> cm<sup>-1</sup>. It has also been predicted using first principles calculations that in-plane tensile strain can enhance hole mobility and transparency of 3R CuAlO<sub>2</sub> [23]. Additionally, predictions have been made for 2H CuAlO<sub>2</sub> concerning thermal conductivity and the figure of merit as functions of temperature [24].

Studies concerning α AgAlO<sub>2</sub> report a higher direct band gap (3.6 eV) and lower optical absorption than α CuAlO<sub>2</sub> within the visible portion of the spectrum, but similar or lower conductivity and predict through first principles calculations that this behavior is due to fewer Ag-4*d* states near the valence band maximum compared to Cu-3*d* states in CuAlO<sub>2</sub> [25]. Additionally, it has been demonstrated by measuring the photocatalytic properties of AgMO<sub>2</sub> (M = Al, Ga, In) and performing first principles calculations that α AgAlO<sub>2</sub> resulted in a more dispersed valence band and higher photocatalytic activity as compared to the orthorhombic polymorph [26]. A first principles study predicts that Ag vacancies in 3R AgAlO<sub>2</sub> have a lower formation enthalpy than Cu vacancies in 3R CuAlO<sub>2</sub> [27]. First principles studies also predict the optical properties of 2H CuAlO<sub>2</sub> and AgAlO<sub>2</sub>, including the dielectric functions, refractive index, extinction coefficient, optical conductivity and absorption coefficient [24, 28]. The band gap of β AgAlO<sub>2</sub> has been measured as 2.83 eV and has been determined to be an indirect gap [29].

The experimental direct band gap of  $\alpha$  CuCrO<sub>2</sub> has been reported as 2.95 – 3.3 eV [30–34]. Studies involving Mg doping have shown the effectiveness of stacking layers of  $\alpha$  CuCr<sub>0.93</sub>Mg<sub>0.07</sub>O<sub>2</sub> (CCMO) and Ag using magnetron sputtering to optimize the optoelectronic properties dependent on shorter Ag deposition times and thicker CCMO layers [11]. One first principles study of co-doping N on O-site and Mg on Cr-site 2H CuCrO<sub>2</sub> predicts enhanced *p*-type conductivity over single doping N or Mg separately, due to more hole states existing above the Fermi level [35]. An experimental indirect band gap of 2.58 eV and direct band gap of 3.11 eV has been reported by Lim, Desu, and Rastogi for CuCr<sub>0.93</sub>Mg<sub>0.07</sub>O<sub>2</sub> thin films [36]. Additionally, they report a range in conductivity of 0.6 – 1  $\Omega^{-1}$  cm<sup>-1</sup>, and an approximate hole concentration of  $2 \times 10^{19}$  cm<sup>-3</sup>. Frontzek report an antiferromagnetic helical spin structure in a single crystal of CuCrO<sub>2</sub> below 23.6 K by means of a neutron diffraction study, in which each Cr atom spin is rotated by  $2\pi/3$  with respect to the nearest neighboring Cr atom spin [37].

Finally, a study on 3R AgCr<sub>1-x</sub>Mg<sub>x</sub>O<sub>2</sub> ( $x = 0.04 - 0.20$ ) has determined a band gap of 3.41 – 3.66 eV, which increases as  $x$  increases, and that hole concentration and mobility increase as  $x$  increases from 0.04 to 0.12, giving values for conductivity of  $3.1 \times 10^{-3} - 67.7 \times 10^{-3}$   $\Omega^{-1}$  cm<sup>-1</sup> [15].

Although some properties may be well understood for CuAlO<sub>2</sub>, and *p*-doping has been demonstrated to be effective for CuAlO<sub>2</sub>, CuCrO<sub>2</sub> and AgCrO<sub>2</sub>, the relation/dependence of materials’ properties – primarily electrical conductivity – to native defects like vacancies and interstitials and *p*-doping both through cation deficiency and replacement of T with Mg is still not well understood.

First-principles studies using density functional theory (DFT) are known to be very reliable and powerful in predicting physical properties of semiconductor materials. Here, a first principles study using DFT is conducted to investigate the effects of Cu/Ag and O vacancies and Mg-doping on the structural, electronic, and

optical properties of  $\text{CuAlO}_2$ ,  $\text{AgAlO}_2$ ,  $\text{CuCrO}_2$ , and  $\text{AgCrO}_2$ .

What follows is a discussion of the theory on crystal structures, the foundations of DFT and other necessary physics required for this work along with the computational methodology in chapter 2. Then, in chapters 3 through 5, the results of the investigation will be presented, including discussion of the XTO crystals physical parameters, electronic band structure and density of states, and the charge densities, hole effective masses, and optical properties of 2H-XTO in the pristine, Mg-doped and O-vacant configurations. Lastly, in chapter 6, general conclusions and summarizing remarks will be made and perspectives will be discussed.

## 2. THEORETICAL FUNDAMENTALS AND METHODS

### 2.1. Crystal Structures of XTO

In order to calculate the ground state electron density – which is the crux of first principles calculations and will be thoroughly discussed in section 2.2 – the crystal structure must be treated in an appropriate theoretical framework. For an idealized crystal, there are some number of symmetry operations that may be performed on the structure such that it is left invariant. For this reason, it is possible to construct an atomic basis within a lattice such that replicating the chosen lattice and basis, known as a unit cell, throughout space using only linear translations reproduces the original crystal structure [38]. Translations of the unit cell,  $\mathbf{T}$ , correspond to moving from one point in the lattice to another via linear combinations of primitive lattice vectors,  $\mathbf{a}_1$ ,  $\mathbf{a}_2$ , and  $\mathbf{a}_3$ , such that

$$\mathbf{T} = x\mathbf{a}_1 + y\mathbf{a}_2 + z\mathbf{a}_3 \quad (2.1.1)$$

where  $x$ ,  $y$ , and  $z$  are integers and  $\mathbf{a}_1$ ,  $\mathbf{a}_2$ , and  $\mathbf{a}_3$  span  $\mathbb{R}^3$ . Thus,

$$\{\mathbf{T} \mid \mathbf{T} \in (x\mathbf{a}_1 + y\mathbf{a}_2 + z\mathbf{a}_3) \wedge x, y, z \in \mathbb{Z} \wedge \mathbf{a}_1, \mathbf{a}_2, \mathbf{a}_3 \in \text{span}(\mathbb{R}^3)\} \quad (2.1.2)$$

represents all points in the crystal lattice. Expressed in the canonical basis for  $\mathbb{R}^3$ , the lattice vectors are

$$\begin{aligned} \mathbf{a}_1 &= a_{1x}\hat{\mathbf{x}} + a_{1y}\hat{\mathbf{y}} + a_{1z}\hat{\mathbf{z}} \\ \mathbf{a}_2 &= a_{2x}\hat{\mathbf{x}} + a_{2y}\hat{\mathbf{y}} + a_{2z}\hat{\mathbf{z}} \\ \mathbf{a}_3 &= a_{3x}\hat{\mathbf{x}} + a_{3y}\hat{\mathbf{y}} + a_{3z}\hat{\mathbf{z}} \end{aligned} \quad (2.1.3)$$

where all components are real numbers. The  $i^{\text{th}}$  atomic position in the atomic basis is constructed as a linear combination of the lattice vectors:

$$\mathbf{r}_i = j\mathbf{a}_1 + k\mathbf{a}_2 + l\mathbf{a}_3 \quad (2.1.4)$$

with  $0 \leq j, k, l \leq 1$ .

$\alpha$ -2H XTO, one of the delafossite polymorphs, is modeled using an 8-atom hexagonal primitive cell. The primitive lattice vectors for this cell are

$$\begin{aligned} \mathbf{a}_1 &= a\hat{\mathbf{x}} \\ \mathbf{a}_2 &= -\frac{1}{2}a\hat{\mathbf{x}} + \frac{\sqrt{3}}{2}a\hat{\mathbf{y}} \\ \mathbf{a}_3 &= c\hat{\mathbf{z}} \end{aligned} \quad (2.1.5)$$

with  $|\mathbf{a}_1| = |\mathbf{a}_2|$ . The other delafossite polymorph,  $\alpha$ -3R XTO, is modelled using either a 12-atom hexagonal conventional cell with lattice vectors

$$\begin{aligned} \mathbf{a}_1 &= a\hat{\mathbf{x}} \\ \mathbf{a}_2 &= -\frac{1}{2}a\hat{\mathbf{x}} + \frac{\sqrt{3}}{2}a\hat{\mathbf{y}} \\ \mathbf{a}_3 &= c'\hat{\mathbf{z}} \end{aligned} \quad (2.1.6)$$

where  $|\mathbf{a}_1| = |\mathbf{a}_2|$  and  $c' > c$ , or a 4-atom rhombohedral primitive cell, which when expressed as a linear combination of the conventional cell lattice vectors takes the form

$$\begin{aligned} \mathbf{a}'_1 &= \frac{2}{3}\mathbf{a}_1 + \frac{1}{3}\mathbf{a}_2 + \frac{1}{3}\mathbf{a}_3 \\ \mathbf{a}'_2 &= -\frac{1}{3}\mathbf{a}_1 + \frac{1}{3}\mathbf{a}_2 + \frac{1}{3}\mathbf{a}_3 \\ \mathbf{a}'_3 &= -\frac{1}{3}\mathbf{a}_1 - \frac{2}{3}\mathbf{a}_2 + \frac{1}{3}\mathbf{a}_3 \end{aligned} \quad (2.1.7)$$

and simplifies to

$$\begin{aligned}
 \mathbf{a}'_1 &= \frac{1}{2}a\hat{\mathbf{x}} + \frac{\sqrt{3}}{6}a\hat{\mathbf{y}} + \frac{1}{3}c'\hat{\mathbf{z}} \\
 \mathbf{a}'_2 &= -\frac{1}{2}a\hat{\mathbf{x}} + \frac{\sqrt{3}}{6}a\hat{\mathbf{y}} + \frac{1}{3}c'\hat{\mathbf{z}} \\
 \mathbf{a}'_3 &= -\frac{\sqrt{3}}{3}a\hat{\mathbf{y}} + \frac{1}{3}c'\hat{\mathbf{z}}
 \end{aligned}
 \tag{2.1.8}$$

in the canonical basis, where  $|\mathbf{a}'_1| = |\mathbf{a}'_2| = |\mathbf{a}'_3|$ . Finally, the lattice vectors of the unit cell for the orthorhombic  $\beta$  XTO polymorph are

$$\begin{aligned}
 \mathbf{a}_1 &= a\hat{\mathbf{x}} \\
 \mathbf{a}_2 &= b\hat{\mathbf{y}} \\
 \mathbf{a}_3 &= c\hat{\mathbf{z}},
 \end{aligned}
 \tag{2.1.9}$$

with  $a \neq b \neq c$ , and the unit cell contains 16 atoms. The unit cells for  $\alpha$ -2H,  $\alpha$ -3R, and  $\beta$  XTO are illustrated [17] in Fig. 2.1.

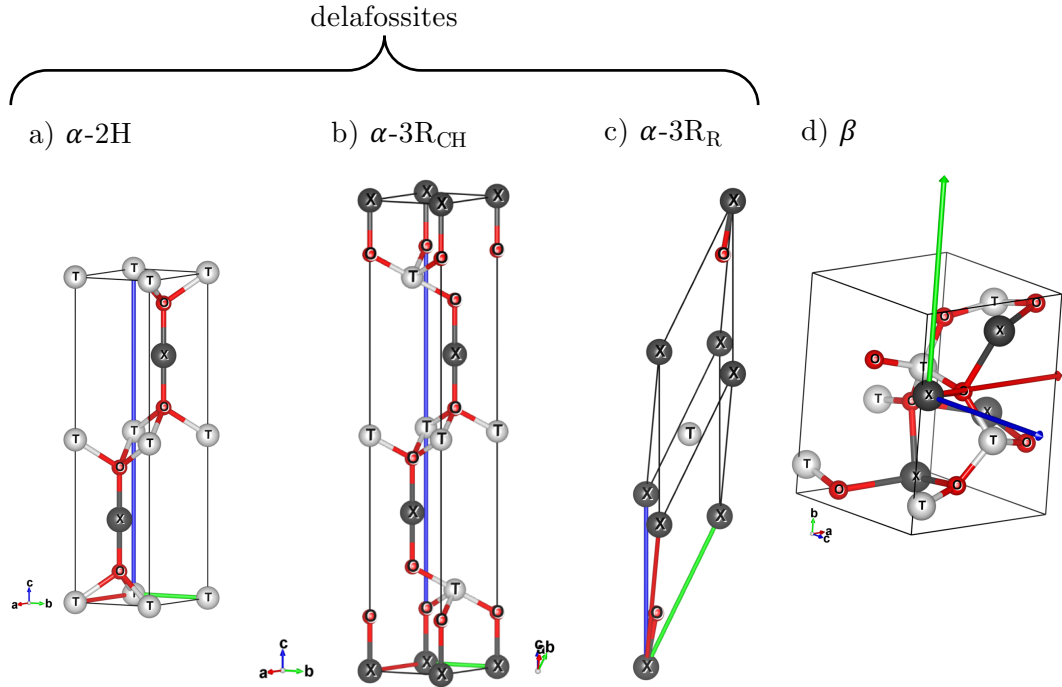


Figure 2.1: XTO unit cells.

The above mathematical framework models the crystal structure in real space. However, since the charge density that satisfies the Schrödinger equation within the crystal is of interest, it is advantageous to transform the real space unit cell into a reciprocal-space cell that exists within a reciprocal lattice with vectors

$$\mathbf{b}_p = 2\pi \frac{\mathbf{a}_q \times \mathbf{a}_r}{\mathbf{a}_1 \cdot \mathbf{a}_2 \times \mathbf{a}_3} \quad (2.1.10)$$

corresponding to a cyclic permutation acting on the indices  $p$ ,  $q$ , and  $r$  [38]. The domain of this new space – which is still  $\mathbb{R}^3$  but is now spanned by  $\mathbf{b}_1$ ,  $\mathbf{b}_2$ , and  $\mathbf{b}_3$  – corresponds to the wave number,  $\mathbf{k}$ , of the carriers in the charge density, and allows for dispersion relations for material properties of the crystal to be determined as a function of the wave number of the carriers in the crystal modeled in this space.

The reciprocal lattice of a hexagonal(orthorhombic) space lattice is also hexagonal(orthorhombic), giving similar unit cells centered at the origin – Brillouin zones (BZ) – in the reciprocal space, but the same cannot be said for a rhombohedral lattice. In converting the rhombohedral space lattice into a reciprocal space lattice, the BZ takes an appearance similar –but not identical – to a body-centered cubic lattice with lattice vectors that are perpendicular to the three hexagonal edges that run along one of the two largest hexagonal faces. Fig. 2.2 illustrates the BZs of  $\alpha$  and  $\beta$  XTO [39, 40].

Since the crystal structure is periodic in this way, so too is the potential that arises from the nuclei in the atomic basis. The Bloch theorem guarantees that for any periodic potential there exists a single-orbital wave function,  $\phi_{n\mathbf{k}}(\mathbf{r})$ , such that

$$\phi_{n\mathbf{k}}(\mathbf{r}) = e^{i\mathbf{k}\cdot\mathbf{r}} u_{n\mathbf{k}}(\mathbf{r}) \quad (2.1.11)$$

where  $n$  is the energy band number,  $\mathbf{k}$  is a wave number in the band, and  $u_{n\mathbf{k}}(\mathbf{r})$  is the part of the Bloch function with the same periodicity of the crystal [38, 41].

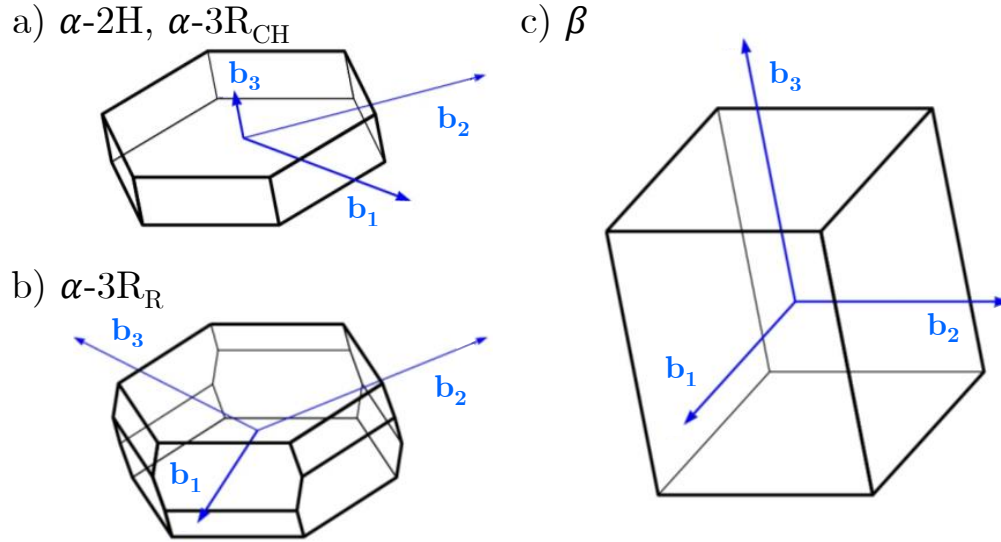


Figure 2.2: XTO Brillouin zones.

## 2.2. Density Functional Theory

The task of obtaining the ground state charge density of a crystal is formidable and involves solving for the forces acting between the nuclei and electrons, but it is also necessary in order to determine the crystal's ground state energy and subsequently all other physical properties [42]. For this reason, it is vital to understand the nature of the problem, how it may be simplified, and how those simplifications allow for the problem to be solved without loss of appreciable accuracy. What follows, then, is a discussion of finding the charge density as viewed in the context of the many body problem, the theorem that guarantees that a solution can be found, the formalism used to find it, and the algorithm used to employ that formalism in numerical calculations.

**2.2.1. Many body problem.** As stated, determining a crystal's ground state charge density can be treated as solving a many body problem. Classically, the total energy of the crystal,  $E$ , is a sum of the crystal's kinetic energy,  $T$ , and potential energy,  $V$ ,

$$E_{\text{tot}} = T + V. \quad (2.2.1)$$

For a system with  $N$  electrons and  $M$  nuclei, the kinetic energy of the crystal is the sum of the individual kinetic energies of each electron and nuclei

$$T = \frac{m_e}{2} \sum_{i=1}^N v_i^2 + \frac{1}{2} \sum_{j=1}^M m_j v_j^2, \quad (2.2.2)$$

where  $m_e$  and  $m_j$  are the electron mass and the mass of the  $j^{\text{th}}$  nuclei, and  $v_i$  and  $v_j$  are the  $i^{\text{th}}$  electron and  $j^{\text{th}}$  nuclei speeds, respectively. Similarly, the crystal potential energy is the sum of all the potentials arising from the presence of each individual electron and nucleus. The total potential can be expressed as a sum of the potentials arising from electron-electron interaction,  $V_{ee}$ , nuclei-nuclei interaction,  $V_{nn}$ , and nuclei-electron interaction,  $V_{ne}$ , as

$$V = V_{ee} + V_{nn} + V_{ne}. \quad (2.2.3)$$

Note that in this study potentials external to the crystal are not considered.

Treating the electrons and nuclei simply as point particles [43], an electron with charge,  $e$ , separated from another electron by some distance,  $r_{ee}$ , interacts with a Coulomb energy, written in the SI units as

$$E_{ee} = \frac{e^2}{4\pi\epsilon_0 r_{ee}}, \quad (2.2.4)$$

identical nuclei in the crystal separated by a distance,  $r_{nn}$ , experience a repulsion with energy

$$E_{nn} = \frac{Z^2 e^2}{4\pi\epsilon_0 r_{nn}}, \quad (2.2.5)$$

where  $Z$  is the atomic number, and a nucleus and electron separated by distance  $r_{ne}$  possess a potential energy

$$E_{ne} = \frac{Z e^2}{4\pi\epsilon_0 r_{ne}}. \quad (2.2.6)$$

Thus, the total crystal potential is

$$V = \frac{e^2}{8\pi\epsilon_0} \left[ \sum_{i \neq j}^N \frac{1}{|\mathbf{r}_i - \mathbf{r}_j|} + \sum_{k \neq l}^M \frac{Z_k Z_l}{|\mathbf{R}_k - \mathbf{R}_l|} + 2 \sum_{i=1}^N \sum_{k=1}^M \frac{Z_k}{|\mathbf{r}_i - \mathbf{R}_k|} \right]. \quad (2.2.7)$$

Replacing the right-hand side of Eqn. 2.2.1 with Eqns. 2.2.2 and 2.2.7 give the total crystal energy as

$$E_{\text{tot}} = \frac{m_e}{2} \sum_{i=1}^N v_i^2 + \frac{1}{2} \sum_{j=1}^M m_j v_j^2 + \frac{e^2}{8\pi\epsilon_0} \left[ \sum_{i \neq j}^N \frac{1}{|\mathbf{r}_i - \mathbf{r}_j|} + \sum_{k \neq l}^M \frac{Z_k Z_l}{|\mathbf{R}_k - \mathbf{R}_l|} + 2 \sum_{i=1}^N \sum_{k=1}^M \frac{Z_k}{|\mathbf{r}_i - \mathbf{R}_k|} \right]. \quad (2.2.8)$$

The classically derived total crystal energy in Eqn. 2.2.8 is insufficient because it does nothing to address the non-local wave functions that will comprise the sought-after charge density. However, the classical interpretation of the total energy can be rectified with quantum mechanics by replacing the classical definitions of kinetic and potential energies with their quantum mechanical operators

$$\hat{T} = -\frac{\hbar^2}{2m_e} \sum_{i=1}^N \nabla_i^2 - \frac{1}{2} \sum_{j=1}^M \frac{\nabla_j^2}{m_j}, \quad (2.2.9)$$

$\hat{V}_{\text{ee}}$ ,  $\hat{V}_{\text{nn}}$ , and  $\hat{V}_{\text{ne}}$ . The potential operators retain the form of their classical counterparts. Now the total crystal energy takes the form of the Hamiltonian

$$\hat{H} = -\frac{\hbar^2}{2m_e} \sum_{i=1}^N \nabla_i^2 - \frac{1}{2} \sum_{j=1}^M \frac{\nabla_j^2}{m_j} + \frac{e^2}{8\pi\epsilon_0} \left[ \sum_{i \neq j}^N \frac{1}{|\mathbf{r}_i - \mathbf{r}_j|} + \sum_{k \neq l}^M \frac{Z_k Z_l}{|\mathbf{R}_k - \mathbf{R}_l|} + 2 \sum_{i=1}^N \sum_{k=1}^M \frac{Z_k}{|\mathbf{r}_i - \mathbf{R}_k|} \right]. \quad (2.2.10)$$

The wave function of the electron charge density,  $\Psi$ , satisfies the Schrödinger

equation with the Hamiltonian of Eqn. 2.2.10:

$$\hat{H}\Psi = E_{\text{tot}}\Psi. \quad (2.2.11)$$

In Hartree atomic units, which from the US National Institute of Standards and Technology database (<http://physics.nist.gov/cuu>), are

$$\begin{aligned} 1 \text{ Ha} &= 27.2114 \text{ eV} = 4.3597 \times 10^{-18} \text{ J}, \\ 1 \text{ bohr} &= 0.529177 \text{ \AA} = 0.529177 \times 10^{-10} \text{ m}, \\ 1 \text{ a. u. of mass} &= 9.10938291 \times 10^{-31} \text{ kg}. \end{aligned} \quad (2.2.12)$$

and are used for the remainder of this work unless otherwise stated, Eqn. 2.2.11 takes the form

$$\begin{aligned} \left[ -\sum_{i=1}^N \frac{\nabla_i^2}{2} - \sum_{j=1}^M \frac{\nabla_j^2}{2m_j} + \frac{1}{2} \sum_{i \neq j}^N \frac{1}{|\mathbf{r}_i - \mathbf{r}_j|} + \frac{1}{2} \sum_{k \neq l}^M \frac{Z_k Z_l}{|\mathbf{R}_k - \mathbf{R}_l|} + \sum_{i=1}^N \sum_{k=1}^M \frac{Z_k}{|\mathbf{r}_i - \mathbf{R}_k|} \right] \Psi \\ = E_{\text{tot}}\Psi. \end{aligned} \quad (2.2.13)$$

At this point it is convenient to remember that the desired electron charge density is confined to a crystal. In the ground state, the kinetic energy of the electrons far surpasses the kinetic energy of the nuclei due to the nuclei having masses that are drastically larger than the electron mass and velocities that are much smaller. The dominance of the electron kinetic energy results in the second term on the left-hand side of 2.2.13 approaching zero. Thus, it will be assumed that the nuclei remain stationary – an assumption known as the Bohr-Oppenheimer approximation. Additionally, the fixed positions of the nuclei result in  $V_{\text{nn}}$

remaining constant, allowing for the definition a new energy

$$E = E_{\text{tot}} - \frac{1}{2} \sum_{k \neq l}^M \frac{Z_k Z_l}{|\mathbf{R}_k - \mathbf{R}_l|}, \quad (2.2.14)$$

such that Eqn. 2.2.13 becomes

$$\left[ - \sum_{i=1}^N \frac{\nabla_i^2}{2} + \frac{1}{2} \sum_{i \neq j}^N \frac{1}{|\mathbf{r}_i - \mathbf{r}_j|} + \sum_{i=1}^N \sum_{k=1}^M \frac{Z_k}{|\mathbf{r}_i - \mathbf{R}_k|} \right] \Psi = E \Psi. \quad (2.2.15)$$

The third term in the sum on the left-hand side of Eqn. 2.2.15 is an external potential to the electron charge density due to the nuclei

$$V_n(\mathbf{r}) = \sum_k^M \frac{Z_k}{|\mathbf{r} - \mathbf{R}_k|}. \quad (2.2.16)$$

Eqns. 2.2.15 and 2.2.16 imply that the Hamiltonian now takes the form

$$\hat{H}(\mathbf{r}_1, \mathbf{r}_2, \dots, \mathbf{r}_N) = - \sum_{i=1}^N \frac{\nabla_i^2}{2} + \frac{1}{2} \sum_{i \neq j}^N \frac{1}{|\mathbf{r}_i - \mathbf{r}_j|} + \sum_{i=1}^N V_n(\mathbf{r}_i) \quad (2.2.17)$$

which is known as the many-electron Hamiltonian and can be simplified further to

$$\hat{H}(\mathbf{r}_1, \mathbf{r}_2, \dots, \mathbf{r}_N) = \sum_{i=1}^N \hat{H}_0(\mathbf{r}_i) + \frac{1}{2} \sum_{i \neq j}^N \frac{1}{|\mathbf{r}_i - \mathbf{r}_j|} \quad (2.2.18)$$

where

$$\hat{H}_0(\mathbf{r}) = V_n(\mathbf{r}) - \frac{\nabla^2}{2} \quad (2.2.19)$$

is known as the single-electron Hamiltonian.

The wave function that satisfies the Schrödinger equation arising from the many-electron Hamiltonian is a function of the positions of the electrons in the crystal

$$\Psi = \Psi(\mathbf{r}_1, \mathbf{r}_2, \dots, \mathbf{r}_N), \quad (2.2.20)$$

thus, the probability of finding one electron in the crystal at position  $\mathbf{r}$  is

$$P(\mathbf{r}_1 = \mathbf{r}) = \int |\Psi(\mathbf{r}_1, \mathbf{r}_2, \dots, \mathbf{r}_N)|^2 d\mathbf{r}_1 d\mathbf{r}_2 \dots d\mathbf{r}_N, \quad (2.2.21)$$

where the limits of integration are over the volume within the crystal where the measurement takes place. If the measurement for the position of the electron is over the entire volume crystal, then  $P(\mathbf{r}_1 = \mathbf{r}) = 1$ . The electron charge density,  $n(\mathbf{r})$ , at  $\mathbf{r}$  corresponds to finding any electron at  $\mathbf{r}$ :

$$n(\mathbf{r}) = P(\mathbf{r}_1 = \mathbf{r}) + P(\mathbf{r}_2 = \mathbf{r}) + \dots + P(\mathbf{r}_N = \mathbf{r}). \quad (2.2.22)$$

Substituting Eqn. 2.2.21 into Eqn. 2.2.22 yields

$$n(\mathbf{r}) = N \int |\Psi(\mathbf{r}_1, \mathbf{r}_2, \dots, \mathbf{r}_N)|^2 d\mathbf{r}_1 d\mathbf{r}_2 \dots d\mathbf{r}_N, \quad (2.2.23)$$

and implies that

$$\int n(\mathbf{r}) d\mathbf{r} = N. \quad (2.2.24)$$

**2.2.2. Hohenberg-Kohn theorem.** The many-electron Hamiltonian implies that the external potential due to the nuclei must be exactly known in order to determine the total crystal energy. However, at this point it is not guaranteed that this is even possible, nor is there any guarantee that the determined  $V_n(\mathbf{r})$  will be unique. It was the work of Hohenberg and Kohn [44] in 1964 to prove a very useful result concerning the external potential from nuclei and the relationship between the electron charge density and the total crystal ground state energy that serve as the pillars of density functional theory (DFT).

In general, the total crystal energy is

$$E = \langle \Psi | \hat{H} | \Psi \rangle, \quad (2.2.25)$$

where  $\hat{H}$  is Eqn. 2.2.18. The crystal structure fixes all terms in the many-electron Hamiltonian arising from the external potential from the nuclei and in this way the total crystal energy only depends on the wave function corresponding to the electron charge density. The energy is then a functional,  $F$ , of the wave function such that

$$E = F[\Psi]. \quad (2.2.26)$$

The Hohenberg-Kohn theorem takes the result of Eqn. 2.2.26 a step further and states that the total ground state energy of the crystal,  $E_0$ , is a functional of the ground state electron charge density,  $n_0(\mathbf{r})$ ,

$$E_0 = F_0[n_0(\mathbf{r})]. \quad (2.2.27)$$

The proof of this result hinges on the fact that the ground state energy must be the lowest energy of the system. Introducing the notation

$$\hat{W} = \frac{1}{2} \sum_{i \neq j}^N \frac{1}{|\mathbf{r}_i - \mathbf{r}_j|} \quad (2.2.28)$$

allows the ground state energy to be expressed as

$$E_0 = \langle \Psi | \sum_{i=1}^N V_{n_0}(\mathbf{r}_i) | \Psi \rangle + \langle \Psi | \hat{T} + \hat{W} | \Psi \rangle, \quad (2.2.29)$$

where  $\hat{T}$  is the simplified fixed-nuclei kinetic energy operator from 2.2.9 and  $V_{n_0}(\mathbf{r})$  is the external potential that dictates the ground state charge density. The outer product on the sum in Eqn. 2.2.29 can be re-expressed using Eqns. 2.2.23 and 2.2.24 such that the ground state energy is

$$E_0 = \int d\mathbf{r} n_0(\mathbf{r}) V_{n_0}(\mathbf{r}) + \langle \Psi | \hat{T} + \hat{W} | \Psi \rangle, \quad (2.2.30)$$

If it is assumed, for the purpose of creating a contradiction, that there is another, distinct,  $V_n(\mathbf{r})$ , such that  $V_n(\mathbf{r}) \neq V_{n_0}(\mathbf{r})$  and  $V_n(\mathbf{r})$  has ground state wave function  $\Psi'$ , ground state energy  $E'$ , ground state Hamiltonian  $\hat{H}'$ , and still gives the same ground state charge density  $n_0(\mathbf{r})$ , then  $E'$  is not the ground state energy of the wave function  $\Psi$  and it must be true that

$$\langle \Psi | \hat{H}' | \Psi \rangle > E'. \quad (2.2.31)$$

Putting Eqn. 2.2.31 into the form of 2.2.30 gives

$$\int d\mathbf{r} n_0(\mathbf{r}) V_n(\mathbf{r}) + \langle \Psi | \hat{T} + \hat{W} | \Psi \rangle > E'. \quad (2.2.32)$$

Summing Eqns. 2.2.30 and 2.2.32 gives

$$E_0 - E' > \int d\mathbf{r} n_0(\mathbf{r}) [V_{n_0}(\mathbf{r}) - V_n(\mathbf{r})]. \quad (2.2.33)$$

Since no consideration was given to distinguish  $V_{n_0}(\mathbf{r})$  from  $V_n(\mathbf{r})$ , the same reasoning can be given, starting from Eqn. 2.2.30, for  $V_n(\mathbf{r})$  and  $E'$ , yielding

$$E' - E_0 > \int d\mathbf{r} n_0(\mathbf{r}) [V_n(\mathbf{r}) - V_{n_0}(\mathbf{r})]. \quad (2.2.34)$$

Finally, summing Eqns. 2.2.33 and 2.2.34 gives the desired contradiction

$$0 > 0, \quad (2.2.35)$$

and thus the ground state electron charge density uniquely determines the external potential of the nuclei. Since the external potential is the only undetermined quantity of the many-electron Hamiltonian, *i.e.* the ground state energy is a functional of the ground state wave function, then it must be true that solving the

ground state charge density gives a unique external potential and allows for the total ground state energy to be determined

$$n_0(\mathbf{r}) \rightarrow V_{n_0}(\mathbf{r}) \rightarrow \Psi \rightarrow E_0 \Rightarrow n_0(\mathbf{r}) \rightarrow E_0 \Rightarrow E_0 = E_0 [n_0(\mathbf{r})], \quad (2.2.36)$$

proving that the total ground state crystal energy is a functional of the ground state charge density.

**2.2.3. Hartree-Fock equations.** It is empowering to know that there is a total ground state energy that can be obtained from the ground state electron charge density, but in order to develop an algorithm that will allow for the determination of the ground state charge density, a few more strategic approximations will be required. The problem can be simplified significantly by eliminating the Coulomb potential in Eqn. 2.2.29. Doing so eliminates any interaction between electrons in the crystal. The Hamiltonian of Eqn. 2.2.18 reduces to the single-electron Hamiltonian summed over all electrons, thus the single-electron Schrödinger equation is

$$\sum_{i=1}^N \hat{H}_0(\mathbf{r}_i) \Psi = E \Psi. \quad (2.2.37)$$

Since the electrons do not interact, it is beneficial to assume that the wave function can be expressed as a product solution of  $N$  single-electron wave functions

$$\Psi(\mathbf{r}_1, \mathbf{r}_2, \dots, \mathbf{r}_N) = \phi(\mathbf{r}_1) \phi(\mathbf{r}_2) \dots \phi(\mathbf{r}_N), \quad (2.2.38)$$

giving Eqn. 2.2.37 the form

$$\sum_{i=1}^N \hat{H}_0(\mathbf{r}_i) \phi(\mathbf{r}_1) \phi(\mathbf{r}_2) \dots \phi(\mathbf{r}_N) = E \phi(\mathbf{r}_1) \phi(\mathbf{r}_2) \dots \phi(\mathbf{r}_N). \quad (2.2.39)$$

Each single-electron wave function  $\phi(\mathbf{r}_i)$  returns energy  $\varepsilon_i$  when acted upon by the  $i^{\text{th}}$  single-electron Hamiltonian

$$\hat{H}_0(\mathbf{r}_i)\phi(\mathbf{r}_i) = \varepsilon_i\phi(\mathbf{r}_i) \quad (2.2.40)$$

which along with Eqn. 2.2.39 implies that

$$E = \varepsilon_1 + \varepsilon_2 + \cdots + \varepsilon_N. \quad (2.2.41)$$

Reducing the Hamiltonian to be single-electron in nature has introduced two problems. The first is that on its face the wave functions  $\Psi$  are not antisymmetric and thus will not satisfy the Pauli exclusion principle, and the second is that the Coulomb interaction term that was eliminated from the many-electron Hamiltonian is of the same order of magnitude as the other terms, and thus the total energy of the crystal is underestimated drastically.

The first problem is addressed by constructing  $\Psi$  from the Slater determinant

$$\Psi(\mathbf{r}_1, \mathbf{r}_2, \dots, \mathbf{r}_N) = \left(\frac{1}{N!}\right)^{\frac{1}{2}} \begin{vmatrix} \phi_1(\mathbf{r}_1) & \phi_1(\mathbf{r}_2) & \cdots & \phi_1(\mathbf{r}_N) \\ \phi_2(\mathbf{r}_1) & \phi_2(\mathbf{r}_2) & \cdots & \phi_2(\mathbf{r}_N) \\ \vdots & \vdots & \ddots & \vdots \\ \phi_N(\mathbf{r}_1) & \phi_N(\mathbf{r}_2) & \cdots & \phi_N(\mathbf{r}_N) \end{vmatrix}. \quad (2.2.42)$$

This wave function still satisfies

$$\int |\Psi(\mathbf{r}_1, \mathbf{r}_2, \dots, \mathbf{r}_N)|^2 d\mathbf{r}_1 d\mathbf{r}_2 \dots d\mathbf{r}_N = 1. \quad (2.2.43)$$

Since the electrons no longer interact, the probability of measuring any single electron is statistically independent and the charge density may be written as a

summation over single-electron wave function probability amplitudes

$$n(\mathbf{r}) = \sum_{i=1}^N |\phi_i(\mathbf{r})|^2. \quad (2.2.44)$$

The second problem arising from the single-electron Hamiltonian – the elimination of the Coulomb potential – can be treated by using an approximation that can reasonably mimic the Coulomb potential. Reverting again to a classical approach, a charge distribution  $n(\mathbf{r})$  will obey the Poisson equation

$$\nabla^2 V(\mathbf{r}) = 4\pi n(\mathbf{r}) \quad (2.2.45)$$

such that the electrons have potential energy  $V_{\text{H}}(\mathbf{r}) = -V(\mathbf{r})$ , referred to as the Hartree potential [42], which has the formal solution

$$V_{\text{H}}(\mathbf{r}) = \int d\mathbf{r}' \frac{n(\mathbf{r}')}{|\mathbf{r} - \mathbf{r}'|}, \quad (2.2.46)$$

and also satisfies the Poisson equation

$$\nabla^2 V_{\text{H}}(\mathbf{r}) = -4\pi n(\mathbf{r}). \quad (2.2.47)$$

Adding the Hartree potential gives the single-electron Schrödinger equation the form

$$\left[ -\frac{\nabla^2}{2} + V_{\text{n}}(\mathbf{r}) + V_{\text{H}}(\mathbf{r}) \right] \phi_i(\mathbf{r}) = \varepsilon_i \phi_i(\mathbf{r}), \quad (2.2.48)$$

which must be solved simultaneously with Eqns. 2.2.44 and 2.2.47. The requirement that Eqns. 2.2.44, 2.2.47, and 2.2.48 be solved as a system ensures that the approach is self-consistent.

The minimum energy associated with the ground state wave function  $\Psi$  is obtained via a variational approach. By minimizing the total energy with respect to

small changes to the single-electron wave functions and requiring that the single-electron wave functions be orthonormal

$$\begin{aligned} \frac{\delta E}{\delta \phi_i} &= 0 \\ \int d\mathbf{r} \phi_i^*(\mathbf{r}) \phi_j(\mathbf{r}) &= \delta_{i,j}, \end{aligned} \quad (2.2.49)$$

the Hartree-Fock (HF) equations are obtained

$$\left[ -\frac{\nabla^2}{2} + V_n(\mathbf{r}) + V_H(\mathbf{r}) \right] \phi_i(\mathbf{r}) + \int d\mathbf{r}' V_c(\mathbf{r}, \mathbf{r}') \phi_i(\mathbf{r}') = \varepsilon_i \phi_i(\mathbf{r}), \quad (2.2.50)$$

$$n(\mathbf{r}) = \sum_{i=1}^N |\phi_i(\mathbf{r})|^2, \quad (2.2.51)$$

$$\nabla^2 V_H(\mathbf{r}) = -4\pi n(\mathbf{r}), \quad (2.2.52)$$

where

$$V_c(\mathbf{r}, \mathbf{r}') = - \sum_{j=1}^N \frac{\phi_j^*(\mathbf{r}') \phi_j(\mathbf{r})}{|\mathbf{r} - \mathbf{r}'|}. \quad (2.2.53)$$

The last term on the left-hand side of Eqn. 2.2.50,  $V_c(\mathbf{r}, \mathbf{r}')$ , and given by Eqn. 2.2.53, arises from the constraint on each  $\phi_i(\mathbf{r})$  to obey the Pauli exclusion principle, and is referred to as the correlation potential. This potential is non-local in nature due to the integration over  $\mathbf{r}'$ .

**2.2.4. Kohn-Sham equations.** The canonical framework of DFT is almost complete. The Hohenberg-Kohn theorem elucidates that the total ground state energy of the crystal is a functional of the ground state charge density. Considering Eqns. 2.2.30 and 2.2.36 allows the energy functional to take the form

$$E[n(\mathbf{r})] = \int d\mathbf{r} n(\mathbf{r}) V_n(\mathbf{r}) + \langle \Psi | \hat{T} + \hat{W} | \Psi \rangle. \quad (2.2.54)$$

The work of Kohn and Sham [45] in 1965 was to rectify the energy functional of Eqn. 2.2.54 with the Hartree potential and the correlation potential from the Hartree-Fock equations and a new potential that approximates the last remaining potential acting on the electrons in the crystal, the exchange potential,  $V_x(\mathbf{r})$ , such that the single-electron Hamiltonian is now

$$\hat{H} = -\frac{\nabla^2}{2} + V_n(\mathbf{r}) + V_H(\mathbf{r}) + V_c(\mathbf{r}) + V_x(\mathbf{r}). \quad (2.2.55)$$

The energy functional becomes an expression of the kinetic and potential energies of non-interacting electrons and an extra energy term, the exchange and correlation energy,  $E_{xc}[n(\mathbf{r})]$ , which considers all of the remaining energy of the electrons that is unaccounted for

$$E[n(\mathbf{r})] = \int d\mathbf{r} n(\mathbf{r}) V_n(\mathbf{r}) - \sum_{i=1}^N \int d\mathbf{r} \phi_i^*(\mathbf{r}) \frac{\nabla^2}{2} \phi_i(\mathbf{r}) + \frac{1}{2} \iint d\mathbf{r} d\mathbf{r}' \frac{n(\mathbf{r})n(\mathbf{r}')}{|\mathbf{r} - \mathbf{r}'|} + E_{xc}[n(\mathbf{r})]. \quad (2.2.56)$$

At long last, the framework for determining the ground state charge density is in place. Finding the ground state energy of the electron density in the crystal is a matter of minimizing the energy functional with respect to the charge density evaluated at the ground state

$$\left. \frac{\delta E[n(\mathbf{r})]}{\delta n} \right|_{n_0} = 0. \quad (2.2.57)$$

Eqn. 2.2.57 is known as the Hohenberg-Kohn variational principle and solving it results in the single-particle Schrödinger equation taking the final form of the

Kohn-Sham equation

$$\left[ -\frac{\nabla^2}{2} + V_n(\mathbf{r}) + V_H(\mathbf{r}) + V_{xc}(\mathbf{r}) \right] \phi_i(\mathbf{r}) = \varepsilon_i \phi_i(\mathbf{r}), \quad (2.2.58)$$

where  $V_{xc}(\mathbf{r})$  is the exchange and correlation potential and is determined via

$$V_{xc}(\mathbf{r}) = \left. \frac{\delta E_{xc}[n(\mathbf{r})]}{\delta n} \right|_{n(\mathbf{r})}. \quad (2.2.59)$$

With the Kohn-Sham equations the foundation of DFT is complete. The analytic form of  $E_{xc}[n(\mathbf{r})]$  is unknown, but the functional approach to approximating the exchange and correlation energy is an area of research that has seen many, ever-more elaborate approximations estimate this value with increasing accuracy.

**2.2.5. The exchange and correlation energy: the local density approximation (LDA), generalized gradient approximation (GGA), Hubbard correction (U), hybrid functional, and modified Becke-Johnson (MBJ) potential.** The exchange and correlation energy,  $E_{xc}[n(\mathbf{r})]$ , is guaranteed to have a solution, although currently it is unknown. Despite this, many approximations have been offered over the years. The discussion of approximations to the exchange and correlation energies is restricted to the functionals used within the scope of this thesis, beginning with Kohn and Sham, who suggested that the electron charge density in a crystal be treated like a homogenous electron gas confined to a volume  $V$  [45]. In this approximation, the potential arising from the nuclei of the crystal is treated like a constant. The electrons have wave functions

$$\phi_{\mathbf{k}}(\mathbf{r}) = \frac{1}{V^{\frac{1}{2}}} \exp(i\mathbf{k} \cdot \mathbf{r}) \quad (2.2.60)$$

and have energy

$$\varepsilon_{\mathbf{k}} = \frac{|\mathbf{k}|^2}{2}. \quad (2.2.61)$$

The wave functions are standing, and correspond to the ground state configuration such that the highest occupied energy, known as the Fermi energy [38],  $\varepsilon_F$ , has energy

$$\varepsilon_F = \frac{k_F^2}{2}, \quad (2.2.62)$$

where  $k_F$  is the Fermi wave number, or the wave number of the highest occupied state. The usefulness of adopting this model is that it allows for the form of the exchange and correlation energy for a single electron,  $\varepsilon_{xc}[n(\mathbf{r})]$ , to be determined exactly, such that the total exchange and correlation energy is approximated as

$$E_{xc}[n(\mathbf{r})] = \int d\mathbf{r} n(\mathbf{r}) \varepsilon_{xc}[n(\mathbf{r})]. \quad (2.2.63)$$

This first approximation to  $E_{xc}[n(\mathbf{r})]$  offered by Kohn and Sham can be further refined by first determining an exact exchange energy from the electron gas model in the form of

$$E_x[n(\mathbf{r})] = -\frac{3}{4} \left( \frac{3}{\pi} \right)^{\frac{1}{3}} \int d\mathbf{r} n^{\frac{4}{3}}(\mathbf{r}). \quad (2.2.64)$$

which is determined by integrating over the volume of crystal.

The exchange potential is then just the functional derivative of the exchange energy in Eqn. 2.2.64

$$V_x[n(\mathbf{r})] = - \left( \frac{3}{\pi} \right)^{\frac{1}{3}} n^{\frac{1}{3}}(\mathbf{r}). \quad (2.2.65)$$

**The LDA.** The correlation energy is not such a straightforward solution and must be obtained using numerical methods. However, the idea with this extended approximation, known as the local density approximation for density functional theory (LDA), is that at all points in the crystal there is a local homogeneous electron gas with local density  $n(\mathbf{r})$  that contributes a differential to

the exchange and correlation energy,  $dE_{xc}[n(\mathbf{r})]$ , such that

$$dE_{xc}[n(\mathbf{r})] = d\mathbf{r} \frac{E_{xc}^{\text{HEG}}[n(\mathbf{r})]}{V}, \quad (2.2.66)$$

where  $E_{xc}^{\text{HEG}}[n(\mathbf{r})]$  is the exchange and correlation energy of the homogenous electron gas [46]. Then the LDA functional approximation of the exchange and correlation energy is obtained by integrating Eqn. 2.2.66 over the crystal volume

$$E_{xc}[n(\mathbf{r})] = \int d^3\mathbf{r} \frac{E_{xc}^{\text{HEG}}[n(\mathbf{r})]}{V}. \quad (2.2.67)$$

The LDA functional approximation to the exchange and correlation energy is most accurate for systems with charge densities that vary slowly over space, such as metals, due to its reliance on approximating regions of the charge density as a homogeneous electron gas. The LDA approximation is less accurate for semiconductor and insulator systems, where the homogenous electron gas model becomes a less accurate representation of the electron charge density.

### **The GGA and Perdew, Burke, and Erzenhof (PBE) method.**

The generalized gradient approximations (GGA) seek to further refine the LDA by accounting for higher charge concentrations around the nuclei through a derivative expansion of the charge density [42]. This exchange and correlation energy functional is similar in form to Eqn. 2.2.58, with the addition of a gradient expansion correction functional,  $F_{xc}[n(\mathbf{r}), \nabla n(\mathbf{r}), \nabla^2 n(\mathbf{r}), \dots]$ , in the integrand

$$E_{xc}[n(\mathbf{r})] = \int d^3\mathbf{r} n(\mathbf{r}) \varepsilon_{xc}^{\text{LDA}}[n(\mathbf{r})] F_{xc}[n(\mathbf{r}), \nabla n(\mathbf{r}), \nabla^2 n(\mathbf{r}), \dots] \quad (2.2.68)$$

and

$$\varepsilon_{xc}^{\text{LDA}}[n(\mathbf{r})] = \frac{E_{xc}^{\text{HEG}}[n(\mathbf{r})]}{n(\mathbf{r})V}, \quad (2.2.69)$$

where  $\varepsilon_{xc}^{\text{LDA}}[n(\mathbf{r})]$  is the LDA exchange and correlation energy density functional. Note that in the LDA approximation the gradient expansion correction functional reduces to one and Eqn. 2.2.67 is regained.

Initially, in the GGA approach, only the first order term in the gradient expansion correction functional was used and often the correlation energy contained more error than a pure LDA approach. Langreth and Mehl [47] addressed this problem in 1981 but their work did not address lingering problems with the exchange energy, which arise from modifying the LDA exchange and correlation energy via the gradient expansion correction functional. Specifically, in non-uniform charge densities where the Coulomb potential is not ignored, the presence of an electron at position  $\mathbf{r}$  inherently lowers the probability of finding another electron at position  $\mathbf{r} + \delta\mathbf{r}$  for some small  $\delta r$ . The exclusion of other electrons from the vicinity of the first can be thought of as an artificial hole, and considering all of these holes in the crystal gives a hole density

$$n_h(\mathbf{r}, \mathbf{r}') = n(\mathbf{r}') [g(\mathbf{r}, \mathbf{r}') - 1] \quad (2.2.70)$$

where  $g(\mathbf{r}, \mathbf{r}')$  is the probability of finding a second electron at the position  $\mathbf{r}'$  given that the first is at position  $\mathbf{r}$ . Imposing the requirement that  $\int d\mathbf{r}' n_h(\mathbf{r}, \mathbf{r}') = -1$  when applying the gradient expansion correction functional was found to greatly reduce the error in the exchange energy.

Although many GGA methods have been introduced over the years, the method of Perdew, Burke, and Erzenhof [48] (PBE) introduced in 1996 further increased the accuracy of the exchange and correlation energies and is seen as the standard GGA approach today. The PBE method gives a spin-dependent

correlation energy functional as

$$E_c[n_\uparrow(\mathbf{r}), n_\downarrow(\mathbf{r})] = \int d^3\mathbf{r} n(\mathbf{r}) [E_c^{\text{LDA}}(r_s, \zeta) + H(r_s, \zeta, t)] \quad (2.2.71)$$

for  $n(\mathbf{r}) = n_\uparrow(\mathbf{r}) + n_\downarrow(\mathbf{r})$ , where  $r_s$  is the local Wigner-Seitz radius

$$r_s = \left[ \frac{3}{4\pi n(\mathbf{r})} \right]^{\frac{1}{3}}. \quad (2.2.72)$$

Additionally,

$$\zeta = \frac{n_\uparrow(\mathbf{r}) - n_\downarrow(\mathbf{r})}{n(\mathbf{r})} \quad (2.2.73)$$

and

$$t = \frac{|\nabla n(\mathbf{r})|}{2\varphi(\zeta)k_s n(\mathbf{r})}. \quad (2.2.74)$$

In Eqn. 2.2.74,

$$\varphi(\zeta) = \frac{1}{2} \left[ (1 + \zeta)^{\frac{2}{3}} + (1 - \zeta)^{\frac{2}{3}} \right] \quad (2.2.75)$$

is the spin-scaling factor,

$$k_s = \left( \frac{4k_F}{\pi} \right)^{\frac{1}{2}} \quad (2.2.76)$$

is the Thomas-Fermi screening wave number, and  $k_F$  is the Fermi wave number with

$$k_F = [3\pi^2 n(\mathbf{r})]^{\frac{1}{3}}. \quad (2.2.77)$$

To satisfy the correlation energy functional, the Hamiltonian in Eqn. 2.2.67 takes the form

$$H = \gamma\varphi^3(\zeta) \ln \left[ 1 + \frac{\beta t^2}{\gamma} \left( \frac{1 + At^2}{1 + At^2 + A^2 t^4} \right) \right], \quad (2.2.78)$$

with  $\gamma = 0.1091$ ,  $\beta = 0.066725$ , and

$$A = \beta \left( \gamma \exp \left\{ \frac{-\varepsilon_c^{\text{LDA}}[n(\mathbf{r})]}{\gamma\varphi^3(\zeta)} - 1 \right\} \right). \quad (2.2.79)$$

The GGA exchange energy in the PBE method is given by

$$E_x[n(\mathbf{r})] = \int d^3\mathbf{r} n(\mathbf{r}) \varepsilon_x^{\text{LDA}}[n(\mathbf{r})] F_x(s). \quad (2.2.80)$$

where

$$F_x(s) = 1 + \kappa - \frac{\kappa}{1 + \mu s^2 / \kappa}. \quad (2.2.81)$$

In Eqn. 2.2.81,  $\mu = 0.21951$ ,  $\kappa = 0.804$ , and  $s$  is a dimensionless density gradient such that

$$s = \frac{|\nabla n(\mathbf{r})|}{2k_F n(\mathbf{r})}. \quad (2.2.82)$$

Summing Eqns. 2.2.71 and 2.2.80 gives the total PBE exchange correlation potential.

**The GGA+U approach.** As much of an improvement that the PBE method is, it still suffers from one of the pitfalls plaguing the LDA approach, namely that error is increased for highly correlated systems, such as in the case for Mott insulators like the transition metal oxides [49]. Essentially, energies associated with transitions in the  $d$  and  $f$  orbitals are drastically underestimated since the LDA method is a mean field theory and the interactions are expected to be small compared to the band gap width. For a weakly correlated system, the exchange splitting is independent of wave number and can be related back to the magnetization  $m(\mathbf{r})$  by

$$\langle \phi_j^{\mathbf{k}} | f(\mathbf{r}) m(\mathbf{r}) | \phi_j^{\mathbf{k}} \rangle \approx -mI \quad (2.2.83)$$

where  $f(\mathbf{r})$  is the occupancy at position  $\mathbf{r}$  and  $I$  is the Stoner parameter and represents the Hund's rule exchange. In contrast, the exchange splitting in highly correlated systems is not dependent on the Stoner parameter, but instead the

Hubbard parameter,  $U$ , which is an on-site quasiautomatic interaction

$$U = E(d^{n+1}) + E(d^{n-1}) - 2E(d). \quad (2.2.84)$$

The Hubbard parameter is the Coulomb energy required for two electrons to occupy the same site in a  $d$  (or  $f$ ) orbital. The Hund's rule exchange parameter is typically one order of magnitude lower than the Hubbard parameter, leading to the underestimated  $d$  orbital transitions. The Hubbard correction is a functional [49] of the form

$$E_{xc}^{+U}[N(\mathbf{r})] = E_{xc}[N(\mathbf{r})] + \frac{U}{2} \sum_i \sum_{m,m',\sigma} (n_{im\sigma} - n^0)(n_{im'\sigma} - n^0) + \frac{U - J}{2} \sum_i \sum_{m \neq m', \sigma} (n_{im\sigma} - n^0)(n_{im'\sigma} - n^0) \quad (2.2.85)$$

where  $n_{im\sigma}$  are the spin- and orbital-dependent occupancies of only the strongly correlated electrons defined in a single-particle, orthonormal basis, and  $n^0$  is the average occupancy of one  $d$  orbital. With GGA+U it is possible to employ the PBE method and still treat highly correlated systems, but the accuracy offered by the exchange and correlation function can still be improved.

**The hybrid functional (HSE06).** The nature of determining the ground state charge density by means of either the non-local Hartree-Fock theory or the semi-local DFT equations introduces error into the exchange and correlation functional approximations that is similar in nature to the applied theory; non-local approaches have non-local error and semi-local approaches have semi-local error. One way to reduce the error in obtaining an exchange and correlation energy functional is to create an exchange energy that is a linear combination of HF and

DFT exchange energies and add it to the correlation energy of DFT,

$$E_{xc}[n(\mathbf{r})] = \alpha E_x^{\text{HF}}[n(\mathbf{r})] + (1 - \alpha) E_x^{\text{DFT}}[n(\mathbf{r})] + E_c^{\text{DFT}}[n(\mathbf{r})]. \quad (2.2.86)$$

In this work, the hybrid functional used is the HSE06 functional [50], where  $\alpha = 0.25$ .

**The modified Becke-Johnson (MBJ) potential.** Tran and Blaha offered one improvement [51] in 2009 based on the Becke-Johnson exchange potential, which seeks to reproduce the shape of exact optimized effective potentials rather than refine the exchange and correlation potentials. Their proposed potential, the modified Beck-Johnson (MBJ) potential is

$$v_{x,\sigma}^{\text{MBJ}}(\mathbf{r}) = cv_{x,\sigma}^{\text{BR}}(\mathbf{r}) + (3c - 2) \frac{1}{\pi} \left[ \frac{5}{12} \right]^{\frac{1}{2}} \left[ \frac{2\tau_\sigma(\mathbf{r})}{n(\mathbf{r})} \right]^{\frac{1}{2}}, \quad (2.2.87)$$

where  $n(\mathbf{r})$  is the charge density of Eqn. 2.2.44,

$$c = \alpha + \beta \left( \frac{1}{V_{\text{cell}}} \int d^3\mathbf{r}' \frac{|\nabla\rho(\mathbf{r}')|}{\rho(\mathbf{r}')} \right)^{\frac{1}{2}}, \quad (2.2.88)$$

with  $\alpha$  and  $\beta$  acting as free parameters and the limits of integration are over the volume of the cell. Additionally,  $\tau_\sigma(\mathbf{r})$  is the kinetic-energy density

$$\tau_\sigma(\mathbf{r}) = \sum_{i=1}^N \phi_{i,\sigma}^* \nabla \phi_{i,\sigma}, \quad (2.2.89)$$

and  $v_{x,\sigma}^{\text{BR}}(\mathbf{r})$  is the Becke-Roussel (BR) potential [52] which is intended to treat the Coulomb potential created by the exchange hole

$$v_{x,\sigma}^{\text{BR}}(\mathbf{r}) = -\frac{1}{b_\sigma(\mathbf{r})} \left\{ 1 - \exp[-x_\sigma(\mathbf{r})] - \frac{1}{2} x_\sigma(\mathbf{r}) \exp[-x_\sigma(\mathbf{r})] \right\}. \quad (2.2.90)$$

The parameter  $x_\sigma(\mathbf{r})$  is determined in the context of  $n(\mathbf{r})$ ,  $\nabla n(\mathbf{r})$ ,  $\nabla^2 n(\mathbf{r})$  and  $\tau_\sigma(\mathbf{r})$ . Then  $b_\sigma$  takes the form

$$b_\sigma(\mathbf{r}) = \left\{ \frac{x_\sigma^3(\mathbf{r}) \exp[-x_\sigma(\mathbf{r})]}{8\pi n(\mathbf{r})} \right\}^{\frac{1}{3}}. \quad (2.2.91)$$

The MBJ potential is meant as an improvement for results obtained using a self-consistent approach, *i.e.* solving the Kohn-Sham equations using the LDA or GGA, by increasing the accuracy of the results through adding  $v_{x,\sigma}^{\text{MBJ}}(\mathbf{r})$  to the exchange and correlation potential, in a process referred to as a meta- LDA or GGA approach.

Explicit approximations for the exchange and correlation potential enable DFT to be put to use in calculating ground state charge densities and total energies. How this is done is the focus of the next section.

### 2.3. Determination of the Ground State Electron Charge Density.

The task of determining the ground state charge density and total energy is carried out through DFT-based numerical calculations performed via computation. To facilitate the ease of computation, several techniques are employed to approximate aspects of the calculation and the wave functions that satisfy the Kohn-Sham equations. What follows, then, is an accounting of two crucial approximations as well as an overview of the algorithm of solving the electron charge density through use of a DFT-based computational software package, the Vienna Ab Initio Simulation Package [53–56] (VASP).

**2.3.1. The projector-augmented wave (PAW) method and pseudopotentials.** Recall that in the initial discussion of the crystal potential in subsection 2.2.1 that the total potential was a superposition of separate potentials handling electron-electron, nuclei-nuclei, and nuclei-electron interactions. Within the crystal, bound electrons in the core states near the nucleus create a

charge-screening effect that weakens the Coulomb potential experienced by valence states. This phenomenon results in a much higher oscillation frequency of the wave functions in the core region than in the valence region. For that reason, the wave functions are modeled in two parts: the core region wave functions are treated as a partial-wave expansion in a sphere surrounding the nucleus, and in an outer shell beyond the core region the wave functions are modeled using plane waves [57].

In the frozen core approach [57, 58], the linear-augmented plane wave (LAPW) method uses ab-initio-based calculations to determine the wave functions in the core region by self-consistent means using local-density-functional theory based atomic potentials. A pseudo wave function is then generated by removing the oscillation such that the pseudo wave function approximately matches the real one outside of the core region. Even in the valence region, the wave functions – which are the single-electron Kohn-Sham wave functions called the all-electron (AE) wave functions – oscillate in a Hilbert space that is orthogonal to the core region in such a way as to make numerical approaches through computation difficult. The PAW method was introduced by Blöchl [57] in 1994 and applies a linear transformation to the all-electron (AE) wave functions that map them into a pseudo-Hilbert (PS) space, making calculations easier. Numerical approaches cannot fully treat a Hilbert space, and so to limit error both the AE and PS wave functions are truncated in a prescribed way.

To apply the linear transformation, an augmentation region similar to the frozen-core region of the LAPW method is established, outside of which the AE and PS wave functions are identical. Within the augmentation region, each PS single-electron wave function,  $|\tilde{\phi}\rangle$ , is a linear combination of  $|\tilde{\psi}_i\rangle$ , the partial PS wave functions

$$|\tilde{\phi}\rangle = \sum_{i=1}^N c_i |\tilde{\psi}_i\rangle, \quad (2.3.1)$$

and each AE one-electron wave function,  $|\phi\rangle$ , is a linear combination of partial AE

wave functions,  $|\psi_i\rangle$ , which are obtained through the linear transformation,  $T$ , on the corresponding PS single-electron wave function

$$|\phi\rangle = T |\tilde{\phi}\rangle = \sum_{i=1}^N c_i |\psi_i\rangle. \quad (2.3.2)$$

The constants  $c_i$  are given by

$$c_i = \langle \tilde{p}_i | \tilde{\phi}_i \rangle, \quad (2.3.3)$$

where  $\tilde{p}_i$  are the Blöchl projector functions, which minimize the total energy via the condition

$$\langle \tilde{p}_i | \tilde{\psi}_j \rangle = \delta_{ij}, \quad (2.3.4)$$

with

$$\delta_{ij} = \begin{cases} 1, & \text{if } i = j \\ 0, & \text{if } i \neq j, \end{cases}$$

is the Kronecker delta. Thus, from Eqns. 2.3.1 and 2.3.2, in the PAW method the AE single-electron wave function is

$$|\phi\rangle = |\tilde{\phi}\rangle - \sum_{i=1}^N c_i |\tilde{\psi}_i\rangle + \sum_{i=1}^N c_i |\psi_i\rangle, \quad (2.3.5)$$

from which the PS wave functions become the variational parameters used during calculations.

**2.3.2. The Vienna Ab Initio Simulation Package (VASP).** Using the previously discussed theoretical framework as well as the unit cell and atomic basis discussed in section 2.1 and the electronic configuration of each atom, the ground state electron charge density of Eqn. 2.2.44 and ground state wave functions of Eqn. 2.3.5 can be calculated by means of an iterative, numerical method for solving the Kohn-Sham Eqn. 2.2.58.

A Rayleigh-Ritz variational approach to the sub-space diagonalization of

the trial AE wave functions of the valence electrons is employed

$$\langle \phi_j | \hat{H} | \phi_i \rangle = H_{ij}. \quad (2.3.6)$$

This diagonalization process is excessively demanding when calculated in a straightforward manner for large systems. However, it was the work of Car and Parrinello [59] in 1985 to prove that the total potential energy Hamiltonian in real space and the total kinetic energy Hamiltonian in reciprocal space are already diagonal. Thus, computational time can be optimized by performing fast Fourier transforms – to be discussed shortly – from one Hamiltonian to the other and vice versa. The self-consistent cycle, which is used by VASP, is even more computationally efficient, and involves the mixing of the Car and Parrinello method with an iterative algorithm to determine the ground state charge density.

The process is applied to one single-electron wave function at a time and revolves around finding the error in the trial solution for each iterative step and adding the error to the trial wave function, producing a new wave function for the next iterative step. The result is ever-increasing accuracy of the eigenvalues over time, with the process completing when the change in total energy from one iterative step to the next is below some threshold value. The eigenvalues are calculated as

$$\varepsilon_i = \frac{\langle \phi_i | \hat{H} | \phi_i \rangle}{\langle \phi_i | \hat{S} | \phi_i \rangle}, \quad (2.3.7)$$

where the operator  $\hat{S}$  is

$$\hat{S} = 1 + \sum_{i=1}^N \sum_{j=1}^N q_{ij} |\tilde{p}_j\rangle \langle \tilde{p}_i| \quad (2.3.8)$$

and

$$q_{ij} = \int d^3\mathbf{r} Q_{ij}(\mathbf{r}), \quad (2.3.9)$$

using  $\tilde{p}_i$ , the localized projection states from the PAW method in Eqns. 2.3.2 and

2.3.5. In Eqn. 2.3.9,  $Q_{ij}(\mathbf{r})$  are the localized augmentation functions. The operator  $\hat{S}$  is subject to the normalization condition

$$\langle \phi_i | \hat{S} | \phi_j \rangle = \delta_{ij}. \quad (2.3.10)$$

A residual vector to facilitate finding the error in the wave function (WF) is given by

$$|R_{\text{WF}}\rangle = (\hat{H} - \varepsilon_i \hat{S}) | \phi_i \rangle, \quad (2.3.11)$$

such that the error in the wave function,  $|\phi_i^{\text{err}}\rangle$ , becomes

$$|\phi_i^{\text{err}}\rangle = \left( \frac{1}{\hat{H} - \varepsilon_i} \right) |R_{\text{WF}}\rangle. \quad (2.3.12)$$

The error does not have an exact solution due to the dominance of kinetic energy in the Hamiltonian arising from large reciprocal lattice vectors,  $\mathbf{G}$ , in reciprocal space,

$$\lim_{G \rightarrow \infty} \hat{H} = \frac{\mathbf{G}^2}{2}, \quad (2.3.13)$$

thus the error is treated with an approximation that limits large  $\mathbf{G}$  and keeps small values tending towards a constant. Once the error is added to the trial wave function, the process repeats for the next band, until all eigenvalues and wave functions are determined, after which they are diagonalized via the Gram-Schmidt method and the new trial wave functions are then used in the next iteration after the partial occupancies and charge density is updated. As previously mentioned, this process repeats until the change in total energy falls below a threshold value.

The electron charge density is updated by mixing the input and output charge densities from each iteration. The residual vector for the error in the charge

density is

$$R_{\text{CD}}[n_{\text{in}}(\mathbf{r})] = n_{\text{out}}[n_{\text{in}}(\mathbf{r})] - n_{\text{in}}(\mathbf{r}), \quad (2.3.14)$$

where  $n_{\text{out}}[n_{\text{in}}(\mathbf{r})]$  is a functional of the input charge density,  $n_{\text{in}}(\mathbf{r})$ . The charge density of Eqn. 2.2.44 is modified to take the form

$$n(\mathbf{r}) = \sum_{i=1}^N f_i |\phi_i(\mathbf{r})|^2 + \sum_{i=1}^N \sum_{j=1}^N \sum_{k=1}^N f_i \langle \phi_i | \tilde{p}_k \rangle \langle \tilde{p}_j | \phi_i \rangle Q_{jk}(\mathbf{r}), \quad (2.3.15)$$

with the sums over  $i$ ,  $j$ , and  $k$  happening independently and where  $f_i$  is the occupancy number one or zero. The mixing method for the step  $l + 1$  is then

$$n_{\text{in}}^{l+1}(\mathbf{r}) = n_{\text{in}}^l(\mathbf{r}) + A R_{\text{CD}}[n_{\text{in}}^l(\mathbf{r})], \quad (2.3.16)$$

where  $A$  is a value determined from the eigenvalue spectrum.

The specific method for mixing that VASP uses is that of Pulay [60], such that all of the preceding charge densities from earlier iterations are linearly combined into a current optimized charge density

$$n_{\text{in}}^{\text{opt}}(\mathbf{r}) = \sum_{i=1}^N \alpha_i n_{\text{in}}^i(\mathbf{r}), \quad (2.3.17)$$

with  $\alpha_i$  subject to

$$\sum_{i=1}^N \alpha_i = 1. \quad (2.3.18)$$

The Pulay method gives residual vector

$$|R_{\text{in}}^{\text{opt}}\rangle = \sum_{i=1}^N \alpha_i |R_{\text{in}}^i\rangle. \quad (2.3.19)$$

The intent is that the new optimal charge density must minimize the norm of the residual vector,  $\langle R_{\text{in}}^{\text{opt}} | R_{\text{in}}^{\text{opt}} \rangle$ , with the process repeated iteratively until reaching the

required accuracy.

## 2.4. Beyond the VASP Code.

As stated in section 2.2, obtaining the ground state electron charge density and total crystal energy enables – in theory – the determination of all physical properties of the crystal. In the computational approach, many physical properties are calculated – with a few exceptions, notably force constants and optical properties – as a post-process in which the ground state charge density and eigenvalues obtained from first-principles calculations are then used by supplementary software that performs the required additional calculations. In this work, the response of the total crystal energy to changes in the unit cell lattice constants, changes to the wave number and magnitude of the hole effective masses as a result of introducing native defects and dopants in XTO, and the optical properties associated with the pristine and defective crystals are of interest.

**2.4.1. The Birch-Murnaghan equation of state.** In order to obtain theoretical optimized lattice constants for a crystal, it is necessary to calculate the total crystal energy using many different unit cell volumes. For any particular volume,  $V$ , of the crystal, there is an associated total energy,  $E$ , and in the case that the volume is the relaxed volume then the lowest – and correct – ground state energy is obtained. The lowest ground state energy is given by theoretically optimized lattice constants that approach the lattice constants of the crystal observed in nature, although due to the approximations employed by DFT-based calculations these values will not be identical. Although there may be a lowest ground state energy associated with a series of total energy calculations for similar crystals different only by unit cell volume, it would only be coincidental for that lowest energy to truly correspond to the optimized lattice constants. For this reason, the optimized lattice constants must be interpolated by fitting an equation of state to the series and finding the minimum of the function. In this work, the

Birch-Murnaghan equation of state [61, 62] is employed for this process,

$$E(V) = E_0 + \frac{9V_0B_0}{16} \left\{ \left[ \left( \frac{V_0}{V} \right)^{\frac{2}{3}} - 1 \right]^3 + B_0 \left[ \left( \frac{V_0}{V} \right)^{\frac{2}{3}} - 1 \right]^2 \left[ 6 - 4 \left( \frac{V_0}{V} \right)^{\frac{2}{3}} \right] \right\}, \quad (2.4.1)$$

where  $E_0$  is the minimum energy of the curve,  $V_0$  is the associated volume of the minimum energy, and  $B_0$  is the bulk modulus of the crystal

$$B = -V \left( \frac{\partial P}{\partial V} \right)_T \quad (2.4.2)$$

evaluated at constant temperature and zero pressure

$$B_0 = -V \left( \frac{\partial P}{\partial V} \right)_T \Big|_{P=0}. \quad (2.4.3)$$

The pressure is given by

$$P = \left( \frac{\partial E}{\partial V} \right)_S \quad (2.4.4)$$

evaluated at constant entropy. Therefore, at the relaxed volume which corresponds to the ground state energy of the crystal, there is zero pressure.

There are several ways to implement the method outlined above, and in this work a series of ground state energies are determined for a series of volumes, all defined by fixing one lattice constant and varying the other – recall that XTO has one lattice constant shared by two vectors . The minimum energy determined by the equation of state gives a more optimized value for the varying lattice constant than the initial value, and the new value is then held fixed while the second lattice constant is varied to produce new volumes which generate new ground state energies that can then be fitted by the equation of state again. In general, each application of the equation of state should produce a minimum total energy that is lower than the one before it, so repeating the curve fitting in this way until the

change in total ground state energy falls below a threshold value corresponds to determining the optimized lattice constants.

#### 2.4.2. Hole effective masses and the method of band unfolding.

A vital quality of any effective semiconductor is to have a high electrical conductivity in the on state. The electrical conductivity is affected by two main factors, namely the number of available charge carriers for conduction and their mobility [38]. The charge carrier mobility,  $\mu$ , is a measure of the carrier's response to the internal electric field of the crystal which is induced by the potential created by the charged nuclei and carriers. This internal electric field arises regardless of the presence of an external bias and produces a current within the crystal. Thus, the mobility relates directly to the carrier charge,  $e$ , which is either negative or positive depending on the nature of the carrier – whether it is an electron or a hole, respectively – and indirectly to the carrier mass,  $m$ , which is also positive or negative for the same reason as the charge. The carrier mass affects the acceleration that the charge experiences in the presence of the electric field through inertia. Additionally, the configuration of the potential in the crystal affects the charge carrier mobility by creating scattering events as the charge carrier is accelerated towards nuclei in the crystal, which is accounted for in the mean scattering time,  $\tau$ . In general, then, the charge carrier mobility is

$$\mu = \frac{e\tau}{m}. \quad (2.4.5)$$

For a crystal with  $n$  electrons and  $p$  holes, the electrical conductivity,  $\sigma$ , takes the form of a sum

$$\sigma = ne\mu_e + pe\mu_h, \quad (2.4.6)$$

where the subscript attached to the mobility denotes whether the source is an electron (e) or a hole (h). Substituting Eqn. 2.4.5 into Eqn. 2.4.6 gives

$$\sigma = \frac{ne^2\tau_e}{m_e} + \frac{pe^2\tau_h}{m_h}. \quad (2.4.7)$$

The electrical conductivity is susceptible to tuning by introducing dopants and defects to the crystal, which has an immediate effect on the number of majority charge carriers, but also has the effect of changing the effective mass of the charge carrier and also – perhaps to a lesser extent – affecting the mean scattering time. The hole effective mass changes since this is essentially a measure of how the carrier will be accelerated in the crystal field, and that acceleration is controlled by the electronic band structure which imposes restrictions on the allowed energies of the carrier. Sections 2.1 and 2.2 clearly illustrate how altering the atomic basis of the unit cell will alter the electronic structure. The mean scattering time may also change due to a reconfiguring of the potential as a result of the dopant or defect.

For charge carriers defined as wave packets that are localized around a wave vector  $\mathbf{k}$ , motion through the crystal happens at the group velocity

$$\mathbf{v} = \frac{d\omega}{dk}, \quad (2.4.8)$$

where  $\omega$  is the angular frequency. In the quantum theory, a wave function with energy  $\varepsilon$  has angular frequency  $\omega = \varepsilon/\hbar$ , such that the group velocity of Eqn. 2.4.8 becomes

$$\mathbf{v} = \frac{1}{\hbar} \nabla_{\mathbf{k}} \varepsilon(\mathbf{k}). \quad (2.4.9)$$

The acceleration of the charge carrier in the field is time derivative of the group velocity

$$\frac{d\mathbf{v}}{dt} = \frac{1}{\hbar} \left( \frac{d^2\varepsilon}{dk^2} \frac{dk}{dt} \right), \quad (2.4.10)$$

within which, a mass term, known as the effective mass,  $m_*$ , may be identified

$$m_* = \hbar^2 \left( \frac{d^2\varepsilon}{dk^2} \right)^{-1}. \quad (2.4.11)$$

This effective mass is purely a measure of the inertia experienced by the charge carrier as a result of being accelerated in the crystal electric field, and in general depends on the direction through which the carrier moves in the crystal such that the carrier effective mass is given by a tensor. From Eqn. 2.4.11 it becomes apparent that the carrier effective mass is inversely proportional to the band curvature of the band structure,  $d^2\varepsilon/dk^2$ . In a small enough region around the wavenumber of the carrier, the band can be approximated by a parabola, such that the second order derivative (the curvature) is calculated to be a numerical constant. For semiconductors, conduction is achieved by exciting valence state charge carriers across the band gap into the conduction states, and so the electron effective mass is determined by the curvature at the lowest unoccupied energy state, also known as the conduction band minimum (CBM), while the hole effective mass is determined by the curvature at the highest occupied energy state, or the valence band maximum (VBM).

Naturally, a thoroughly described, well-resolved band structure, especially around the VBM or CBM, is essential for an accurate measurement of the band curvature and subsequently the effective mass of the charge carrier. For many semiconductors it is not good enough to have a measurement of the carrier effective mass in the pristine crystal, since many semiconductors depend on the introduction of dopants and defects to reach their full potential for tunable devices. In order to model doped and defective crystals in DFT-based calculations, the size of the unit cell must be increased in such a way that when it is replicated through space it accurately establishes the crystal structure with the incorporated dopant or defect.

Due to the requirements of periodicity, the arrangement of the dopants or defects in the crystal will not be random, but may be quasi-random depending on their locations in the atomic basis. The supercell (SC) will have primitive reciprocal lattice vectors  $\mathbf{B}_1 = N_i \mathbf{b}_1$ ,  $\mathbf{B}_2 = N_j \mathbf{b}_2$ , and  $\mathbf{B}_3 = N_k \mathbf{b}_3$  for  $N_i, N_j, N_k \in \mathbb{Z}^+$ , where  $\mathbf{b}_1, \mathbf{b}_2$ , and  $\mathbf{b}_3$  are the primitive reciprocal lattice vectors of the primitive cell [38] (PC). In this way, the SC contains  $N_i N_j N_k A$  atoms if  $A$  is the number of atoms in the PC and the term  $N_i \times N_j \times N_k$  SC refers to the length of each edge of the SC in multiples of the corresponding PC unit cell edge.

Although converting to a SC representation alone does not alter the total crystal energy or the charge density distribution other than being composed of more electrons due to the presence of more atoms, resulting in identical electronic density of states (DOS) when normalized by the number of atoms in the cell, it does come with the drawback that it introduces a coupling to the Kohn-Sham orbitals, which results in the “folding” of the electronic band structure into the smaller SC from the larger PC. This phenomenon is brought to the forefront when attempting to measure changes to the charge carrier effective mass as the result of introducing defects and dopants. The folding of the bands in the SC representation of the band structure is not reconcilable with the need to compare the new effective mass location in reciprocal space since it relies on a measurement of the PC VBM band curvature. It becomes essential to unfold the SC representation of the band structure into that of the PC. This is accomplished through the method of Medeiros, Stafström and Björk [63, 64] proposed in 2014, which differs slightly from earlier methods first developed by Boykin and Klimeck [65] in 2005.

As previously mentioned, there is a coupling of the Kohn-Sham orbitals introduced by converting a PC into an SC. Consider a wave function in the SC representation in band number  $m$  with wave vector  $\mathbf{K}$  and eigenstate  $|\phi_{m\mathbf{K}}^{\text{SC}}\rangle$ . In the PAW method (subsection 2.3.1) the eigenstate is a sum of partial wave functions.

The part of the PAWs outside of the augmentation region takes the form

$$|\phi_{m\mathbf{K}}^{\text{SC}}\rangle = \sum_{\mathbf{G}} C_{n,\mathbf{K}}(\mathbf{G}) \exp[i(\mathbf{K} + \mathbf{G}) \cdot \mathbf{r}]. \quad (2.4.12)$$

The SC Brillouin Zone (SCBZ) has a volume  $V_{\text{SCBZ}}$ , and the PC Brillouin Zone (PCBZ) has a volume  $V_{\text{PCBZ}}$  such that there are  $N_{\text{unf}} = V_{\text{PCBZ}}/V_{\text{SCBZ}}$  wave vectors  $\mathbf{k}_i$  in the PCBZ for a wave vector  $\mathbf{K}$  within the SCBZ. The wave vectors  $\mathbf{k}_i$  are given by

$$\mathbf{k}_i = \mathbf{K} + \mathbf{G}_{\mathbf{k}_i \leftarrow \mathbf{K}}, \quad (2.4.13)$$

where  $\mathbf{K}$  unfolds into  $\mathbf{k}_i$  via the unfolding vector  $\mathbf{G}_{\mathbf{k}_i \leftarrow \mathbf{K}}$  in the SCBZ. In other words, a wave vector  $\mathbf{k}_i$  must obey

$$\mathbf{k}_i + \mathbf{g} = \mathbf{K} + \mathbf{G}. \quad (2.4.14)$$

for lattice vectors  $\mathbf{g}$  and  $\mathbf{G}$  in the PCBZ and SCBZ, respectively [66]. When the above condition is satisfied, the PC Blochl wave vector  $\mathbf{k}_i$  PAW expansion coefficients match those of the SC,

$$C_{n,\mathbf{K}}(\mathbf{G}) \rightarrow c_{n,\mathbf{k}}(\mathbf{g}). \quad (2.4.15)$$

The probability that an eigenfunction  $|\phi_{m\mathbf{K}}^{\text{SC}}\rangle$  in the SCBZ has the same eigenenergy as  $|\phi_{n\mathbf{k}_i}^{\text{PC}}\rangle$  in the PCBZ is given by the spectral weight

$$w_{n,\mathbf{K}}(\mathbf{k}_i) = \sum_{\mathbf{g}} C_{n,\mathbf{K}}(\mathbf{k}_i + \mathbf{g}), \quad (2.4.16)$$

such that the SCBZ wave functions can be expressed in terms of the PCBZ wave

functions as

$$|\phi_{m\mathbf{K}}^{\text{SC}}\rangle = \sum_{n,i} w_{n,\mathbf{K}}(\mathbf{k}_i) |\phi_{n\mathbf{k}_i}^{\text{PC}}\rangle. \quad (2.4.17)$$

Specific to the Medeiros, Stafström and Björk method [63], a spectral function  $W(\mathbf{k}_i, \varepsilon)$ , is defined as

$$W(\mathbf{k}_i, \varepsilon) \equiv \sum_n w_{n,\mathbf{K}}(\mathbf{k}_i) \delta[\varepsilon - \varepsilon_n(\mathbf{K})], \quad (2.4.18)$$

with  $\delta$  being the Dirac delta function. The cumulative probability function,  $S_{\mathbf{k}_i}(\varepsilon)$ , has a differential of the form

$$dS_{\mathbf{k}_i}(\varepsilon) = W(\mathbf{k}_i, \varepsilon)d\varepsilon, \quad (2.4.19)$$

which represents the number of PC energy bands crossing the interval  $(\varepsilon, \varepsilon + d\varepsilon)$ . The interval is then mapped onto a  $(\mathbf{k}_i, \varepsilon_j)$  grid with step size  $\delta\varepsilon$ , where an energy weight,  $\delta N(\mathbf{k}_i, \varepsilon_j)$ , is obtained via

$$\delta N(\mathbf{k}_i, \varepsilon_j) \equiv \int_{\varepsilon_j - \delta\varepsilon/2}^{\varepsilon_j + \delta\varepsilon/2} dS_{\mathbf{k}_i}(\varepsilon). \quad (2.4.20)$$

Substituting Eqns. 2.4.18 and 2.4.19 into the above result yields

$$\delta N(\mathbf{k}_i, \varepsilon_j) = \sum_n w_{n,\mathbf{K}}(\mathbf{k}_i) \int_{\varepsilon_j - \delta\varepsilon/2}^{\varepsilon_j + \delta\varepsilon/2} d\varepsilon \delta[\varepsilon - \varepsilon_n(\mathbf{K})]. \quad (2.4.21)$$

The energy weight is then averaged over all  $\mathbf{k}_i$  that relate via symmetry operations of the PCBZ. This method possesses the advantage of not needing to find the peaks of the spectral function  $W(\mathbf{k}_i, \varepsilon)$  nor the steps of the cumulative probability function  $S_{\mathbf{k}_i}(\varepsilon)$ .

The implementation of this method for the measurement of carrier effective masses is essentially to define all  $\mathbf{k}_i$  in the PCBZ, *e.g.* the path through the PCBZ

that gives a band structure for either the CBM or VBM to be measured, and then through the relation in Eqn. 2.4.13 find all required  $\mathbf{K}$  of the path through the SCBZ that must be traced to obtain a band structure that will then be unfolded into the primitive cell representation using the above method. In this way changes in the wave number and magnitude of the carrier effective mass can be studied upon the introduction of dopants and defects.

**2.4.3. Optical properties.** The last set of properties that are of interest in this study are associated with the optical character of the crystal. Consider a semiconductor in which the electron configuration is in the ground state. The electron in the most excited electron state will have an energy equal to that of the Fermi energy and all of the occupied states are valence states. Imparting the electrons with energy will allow them to occupy conduction states if the energy they receive is greater than that of the band gap. This energy can come from many sources, such as thermal excitation or an applied external bias. Similarly, radiation in the form of photons incident on the crystal may also scatter electrons into the conduction band states. Due to the quantum selection rules, for an electron with wave vector  $\mathbf{k}$ , the electron is restricted to possessing excited-state energies,  $\varepsilon_i(\mathbf{k})$ , *i.e.* the electron is only permitted to transitions according to the electronic band structure. For that reason, photons will not excite electrons into excited states (valence nor conduction) unless the interband energy for two eigenenergies,  $\varepsilon_i > \varepsilon_j$  corresponds to the energy,  $E = \hbar\omega$ , of the photon with angular frequency  $\omega$  by

$$\hbar\omega = \varepsilon_i - \varepsilon_j. \quad (2.4.22)$$

Some time after the electron has been excited it will spontaneously relax back into an unoccupied valence state and emit a photon with angular frequency  $\omega'$  corresponding to the change in energy of the electron. A semiconductor is

transparent when the band gap,  $E_g = \varepsilon_{\text{CBM}} - \varepsilon_{\text{VBM}}$ , where  $\varepsilon_{\text{CBM}}$  and  $\varepsilon_{\text{VBM}}$  are the eigenenergies at the CBM and VBM respectively, is large enough that the energies of photons in the visible portion of the spectrum (roughly 1.6–3.0 eV) are too small to allow electron energies to transition across the band gap [67].

The incident photons themselves may be modeled as plane waves

$$\mathbf{E}(\mathbf{r}, t) = \mathbf{E}_0 \exp[i(\hat{\mathbf{k}} \cdot \mathbf{r} - \omega t)], \quad (2.4.23)$$

where  $\mathbf{E}_0$  is the amplitude of the plane wave, and  $\hat{\mathbf{k}}$  is a unit vector parallel to the direction of travel [43, 67]. Using SI units for the remainder of this subsection, Eqn. 2.4.23 satisfies the wave equation

$$\nabla^2 \mathbf{E}(\mathbf{r}, t) = \frac{\mu\epsilon}{c^2} \frac{\partial^2}{\partial t^2} \mathbf{E}(\mathbf{r}, t) + \frac{\mu\sigma}{\epsilon_0 c^2} \frac{\partial}{\partial t} \mathbf{E}(\mathbf{r}, t). \quad (2.4.24)$$

where  $\mu$  and  $\epsilon$  are the permeability and permittivity of the crystal, respectively,  $\epsilon_0$  is the permittivity of the vacuum, and  $\sigma$  is the crystal's electrical conductivity.

Substituting Eqn. 2.4.23 into Eqn. 2.4.24 gives

$$\hat{k}^2 = \frac{\mu\omega^2}{c^2} \left( \epsilon + i \frac{\sigma}{\epsilon_0\omega} \right). \quad (2.4.25)$$

Define a complex refractive index,  $\hat{n} = n + i\kappa$ , such that

$$\hat{k} = \frac{\omega}{c} \hat{n} = \frac{\omega}{c} (n + i\kappa), \quad (2.4.26)$$

which gives the following result when substituted into Eqn. 2.4.23:

$$\mathbf{E}(\mathbf{r}, t) = \mathbf{E}_0 \exp\left(-\frac{\omega}{c} \boldsymbol{\kappa} \cdot \mathbf{r}\right) \exp\left[i\omega \left(\frac{\mathbf{n} \cdot \mathbf{r}}{c} - t\right)\right]. \quad (2.4.27)$$

The exponential term containing the extinction coefficient  $\kappa$  determines the decrease

in the amplitude of the plane wave as a function of distance [67]. The second exponential term is the plane wave phase velocity,  $v_{\text{ph}} = c/n$ . Since  $n \geq 1$ , the phase velocity is always less than the speed of light [67]. In this way, the refractive index is a measure of how much slower the speed of light is in a solid. Together, Eqns. 2.4.25 and 2.4.26 give

$$n^2 - \kappa^2 + i2n\kappa = \mu\epsilon + i\frac{\mu\sigma}{\epsilon_0\omega}. \quad (2.4.28)$$

equating the real and imaginary parts of the above result gives

$$\epsilon = \frac{1}{\mu}(n^2 - \kappa^2), \quad (2.4.29)$$

and

$$\sigma = \frac{2n\kappa\epsilon_0\omega}{\mu}. \quad (2.4.30)$$

Recalling that  $\sigma$  is a coefficient relating the strength of the current density  $J$  produced by an electric field,  $\sigma = J/E$ , and that in this case only the current density produced by incident photons is considered,  $\sigma$  may be referred to as the optical conductivity. A complex dielectric function,  $\hat{\epsilon} = \epsilon_1 + i\epsilon_2$ , may be introduced such that

$$\epsilon_1 = \frac{1}{\mu}(n^2 - \kappa^2) \quad (2.4.31)$$

and

$$\epsilon_2 = 2n\kappa = \frac{\mu\sigma}{\epsilon_0\omega}. \quad (2.4.32)$$

Eqns. 2.4.31 and 2.4.32 can be used to express the refractive index and extinction coefficient in terms of the real and imaginary part of the complex dielectric function:

$$n(\omega) = \left[ \frac{|\hat{\epsilon}(\omega)| + \epsilon_1(\omega)}{2} \right]^{\frac{1}{2}}, \quad (2.4.33)$$

$$\kappa(\omega) = \left[ \frac{|\hat{\epsilon}(\omega)| - \epsilon_1(\omega)}{2} \right]^{\frac{1}{2}}. \quad (2.4.34)$$

The optical conductivity re-expressed in terms of the complex dielectric function is

$$\sigma(\omega) = \frac{\omega}{4\pi} \text{Im}[\hat{\epsilon}(\omega)], \quad (2.4.35)$$

While in terms of the refractive index and extinction coefficient, the reflectivity,  $R(\omega)$ , is

$$R(\omega) = \frac{[n(\omega) - 1]^2 + \kappa^2(\omega)}{[n(\omega) + 1]^2 + \kappa^2(\omega)}. \quad (2.4.36)$$

The absorption coefficient,  $\alpha$ , describes the fractional decrease in intensity,  $I$ , as a function of distance [67]. Since the intensity is proportional to the square of the electromagnetic wave amplitude, norm squaring the plane wave solution of Eqn. 2.4.23 and differentiating with respect to  $r$  gives:

$$\alpha(\omega) = -\frac{dI}{dr} = \frac{2\omega\kappa(\omega)}{c}. \quad (2.4.37)$$

The rate of absorption of a solid, otherwise known as the loss function,  $L$ , is related to the imaginary part of the inverse of the complex dielectric function by

$$L(\omega) = -\text{Im} \left[ \frac{1}{\hat{\epsilon}(\omega)} \right] = \frac{\epsilon_2(\omega)}{\epsilon_1^2(\omega) + \epsilon_2^2(\omega)}. \quad (2.4.38)$$

The complex dielectric function is calculated from the VASP code after the eigenenergies  $\varepsilon_{\mathbf{k}}$  corresponding to the ground state have been determined by enabling `LOPTICS = .TRUE.` in the `INCAR` input file. The imaginary part of the dielectric function can be determined from a summation over conduction states,  $c$ , and valence states,  $v$ , at a wave vector  $\mathbf{k}$

$$\text{Im}[\hat{\epsilon}(\omega)]_{\alpha\beta} = \frac{4\pi^2 e^2}{\Omega} \lim_{q \rightarrow 0} \frac{1}{q^2} \sum_{c,v,\mathbf{k}} 2\omega_{\mathbf{k}} \delta(\varepsilon_{c\mathbf{k}} - \varepsilon_{v\mathbf{k}} - \omega) \langle u_{c\mathbf{k}+\mathbf{e}_\alpha q} | u_{v,\mathbf{k}} \rangle \langle u_{v,\mathbf{k}} | u_{c\mathbf{k}+\mathbf{e}_\beta q} \rangle, \quad (2.4.39)$$

where  $e$  is the fundamental charge,  $\Omega$  is the cell volume,  $q$  is the magnitude of the

Bloch vector,  $\varepsilon_{c\mathbf{k}}$  and  $\varepsilon_{v\mathbf{k}}$  are conduction and valence energies at wave vector  $\mathbf{k}$  respectively, and  $\mathbf{e}_\alpha$  and  $\mathbf{e}_\beta$  are Cartesian unit vectors [68]. The Kramers-Kronig relations gives the real part of the dielectric function from the imaginary part:

$$\text{Re}[\hat{\varepsilon}(\omega)]_{\alpha\beta} = 1 + \frac{2}{\pi} \text{P} \int_0^\infty d\omega' \frac{\omega' \varepsilon_2(\omega')}{\omega'^2 - \omega^2 + i\eta}, \quad (2.4.40)$$

where P is a principle value and  $\eta$  is a complex shift, which can be used to limit local oscillations in the real part of the complex dielectric function. Once the complex dielectric function is calculated by VASP, Eqns. 2.4.33 through 2.4.38 can be used to determine the other previously discussed optical properties.

## 2.5. Computational Methodology

The first principles study using density functional theory will be performed by using the VASP code [53–56]. Projector augmented wave function pseudopotentials [69, 70] will be used in conjunction with the GGA in the PBE method. The screened values,  $U_{\text{Cu}}^{\text{CAO}} = 3.24$  eV,  $U_{\text{Cu}}^{\text{CCO}} = 1.99$  eV,  $U_{\text{Ag}}^{\text{AAO}} = 2.45$  eV,  $U_{\text{Ag}}^{\text{ACO}} = 1.29$  eV,  $U_{\text{Cr}}^{\text{CCO}} = 2.20$  eV, and  $U_{\text{Cr}}^{\text{ACO}} = 1.81$  eV, in  $\text{CuAlO}_2$  (CAO),  $\text{AgAlO}_2$  (AAO),  $\text{CuCrO}_2$  (CCO), and  $\text{AgCrO}_2$  (ACO), were calculated using the ATOM code [71] in the non-relativistic PBE method following the screening effect approach described by Janotti, Segev, and Van de Walle [72]. The valence configuration of each atom set in the ATOM code are:  $\text{Cu}^+ 3d^{10}4s^0$  [73],  $\text{Ag}^+ 4d^{10}5s^0$ ,  $\text{Cr}^{3+} 3d^34s^0$ . Optimized lattice constants for each material were obtained by minimizing the total crystal energy by fitting the Birch-Murnaghan equation of state according to the method described in subsection 2.4.1 via the Gibbs2 code [74, 75]. The valence electron configuration for each atom is as follows: Cu  $3d^{10}4s^1$ , Ag  $4d^{10}5s^1$ , Al  $3s^23p^1$ , Cr  $3d^54s^1$ , Mg  $2p^63s^2$ , O  $2s^22p^4$ . A plane wave cut-off energy of 400 eV was employed during calculations, which were conducted on a  $21 \times 21 \times 5$  gamma-centered k-mesh for band structure and DOS calculations, and

a  $41 \times 41 \times 9$  gamma-centered k-mesh for complex dielectric function calculations on the primitive cell. During the self-consistent phase, each of the atomic positions within each structure were allowed to relax and the calculations were considered converged once the global force on all atoms was less than  $1 \times 10^{-6}$  eV  $\text{\AA}^{-1}$ . The bulk XAO material will be modelled using the unit cells mentioned in section 2.1 to optimize all structures and evaluate the total energy for each polymorph of XAO by means of fitting the Birch-Murnaghan equation of state (of degree 4) using Gibbs2.

With regards to the complex antiferromagnetic configuration of CCO in the ground state reported by Frontzek *et al.* in chapter 2, an accurate model would involve the use of a supercell due to the need for more than two Cr atoms to accurately produce the required spin configuration and would also require the use of the non-colinear version of the VASP code in order to calculate the ground state charge density and wave functions properly. Both of the requirements outlined above would very likely prove too computationally demanding within the scope of this work, and thus in order to justify the adoption of a simple antiferromagnetic (AFM)  $\alpha$ -2H primitive cell, such as the one used by Xu *et al.* [35], in which each of the two Cr atoms in the primitive cell have opposite spin moments aligned along the  $c$ -axis, the total ground state energy of AFM 2H XCO will be scrutinized against a simple ferromagnetic (FM) configuration – where both Cr spins are aligned along the  $c$ -axis – and a nonmagnetic (NM) configuration achieved by ignoring spin during the calculation of the ground state charge density. The different 2H XCO magnetic configurations will be optimized and evaluated by means of the equation of state fitting using the Gibbs2 code described above for the polymorphs of XAO.

2H XTO will be the focus of the remainder of this investigation as it is the least studied of the delafossites. The more accurate – but more computationally demanding – hybrid functional, HSE06, is also used for the exchange and correlation energies of bulk 2H XTO with the intent of using results to scrutinize a

proper choice of Hubbard correction, such that the less computationally demanding Hubbard correction to treat exchange and correlation energies of the Cu/Cr(Ag)- $3d(4d)$  orbitals in the PBE method (+U) can be utilized for the defective/doped systems [76].

Specific to the application of GGA, GGA+U, and hybrid functionals to the study of transition metal oxides (TMOs), namely  $\text{Cu}_2\text{O}$  and other  $\text{A}^+$  cation TMOs, Scanlon, Morgan, and Watson demonstrated [77] in 2009 that the GGA and GGA+U approaches unsuccessfully model the deep traps and other properties associated with the polarons that are understood to be the main conduction mechanism and arise from Cu-vacancy and O-interstitial acceptor-forming defects. Any “improvements” to the inter- Cu- $3d$  state transitions were shown to only be superficial and could not be resolved in the context of experimental ionization levels. It was thus concluded that the GGA and GGA+U methods fail to describe conduction mechanisms in TMOs that are polaronic in nature but hybrid functionals can be successful due to their ability to treat to some degree the exact exchange in all atomic species and not just the Cu- $3d$  states [77]. However, Tate *et al.* have argued that although some groups have reported [78] small polaronic character in  $\text{CuAlO}_2$ , which is a TMO obtained schematically by combining  $\text{Cu}_2\text{O}$  with an aluminate like  $\text{Al}_2\text{O}_3$ , their measurements of  $a - b$  plane and  $c$ -axis mobilities at 300 K of  $3.0$  and  $0.12 \text{ cm}^2 \text{ V}^{-1} \text{ s}^{-1}$  respectively are too large to have dominant polaronic character and therefore support a band conduction model. Though the exact mechanism at work in their offered band conduction model is not known, Tate *et al.* rule out polaronic character in  $\text{CuAlO}_2$ . Additionally, Laskowski *et al.* have demonstrated that a GGA+U approach in the context of the Bethe-Salpeter formalism can describe excitonic effects through calculation of the complex dielectric function [79]. However, such a methodology is outside of the scope of this research. With that in mind, the consideration of the PBE method and

an on-site Hubbard correction for  $d$  states in this work is considered reasonable due to the computational efficiency of the methods.

**2.5.1. Supercell Scheme.** Once pristine 2H XTO is well understood electronically, 64-atom hexagonal supercells will be used to model pristine 2H XTO, 6.25% Cu/Ag-vacant 2H XTO, 3.13% O-vacant 2H XTO, and 6.25% Mg-doped 2H XTO. The supercells are illustrated [17] in Fig. 2.3. Charge densities for the structural and electronic properties will be obtained on an  $11 \times 11 \times 3$  gamma-centered k-mesh and visualized using the VESTA code [17], and optical properties will be derived from a  $7 \times 7 \times 3$  gamma-centered k-mesh, all using PBE+U. All symmetry considerations imposed by the VASP code to facilitate the efficient calculation of the charge density will be turned off in the supercell scheme.

After the electronic structure has been determined for pristine and defective 2H XTO systems, parabolic band fitting will be employed on both primitive cells and all supercells using energies within 10% of the VBM towards adjacent symmetry-like points to measure the hole effective masses in each reciprocal lattice vector direction. Due to the band folding phenomenon discussed in subsection 2.4.2, the band structures of the supercells must first be unfolded into a primitive cell representation using the BandUP code [63, 64].

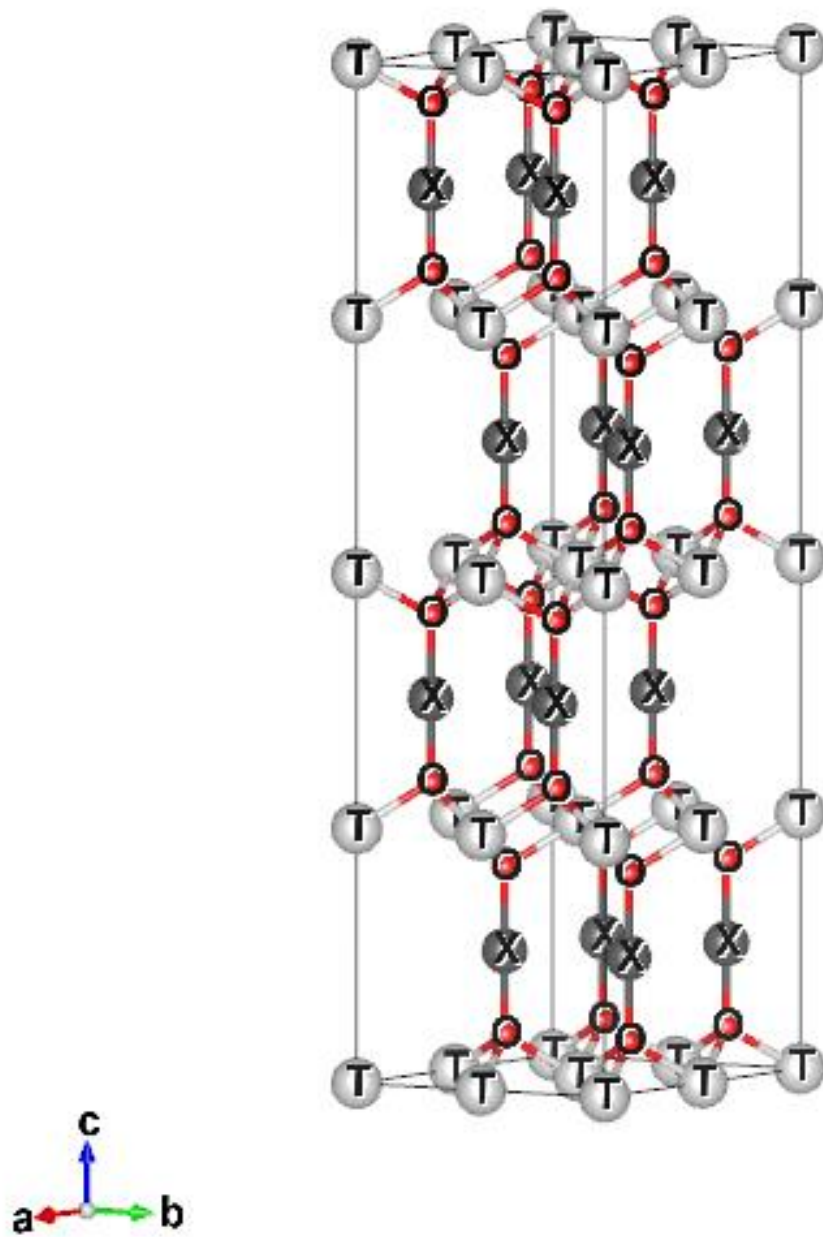


Figure 2.3: 2H XTO  $2 \times 2 \times 2$  supercell.

### 3. STRUCTURAL, ELECTRONIC, AND OPTICAL PROPERTIES OF PURE XTO

#### 3.1. Introduction

The beginning of this study is centered on building as accurate a model of the pristine XTO crystals as possible, comparing their total energies normalized by the number of atoms in each respective cell, and then using those energies to motivate a decision regarding which polymorph to study more thoroughly. Concerning XAO, the choice is among polymorphs, and after which, for XCO modeled with the same polymorph as XAO, the choice is in regard to a simple magnetic configuration – *e.g.* whether the two Cr nuclei in the primitive cell are arranged in a NM configuration where their moments are ignored in the calculation, a FM configuration with parallel moments, or an AFM configuration where the moments are antiparallel. From there, the underestimated band gaps in the PBE method will be treated by modeling the chosen 2H polymorph with the functional approaches discussed in section 2.2 and comparing the obtained band gaps with the experimental values from literature. The 2H XTO crystal will then be re-optimized using the chosen functional approach and several structural parameters will be determined and compared with available experimental data. With XTO optimized in the PBE+U method, the electronic band structure and density of states (DOS) are calculated. Hole effective masses are measured around the VBM, and optical properties are determined. Once a thorough description for the pristine 2H XTO in the primitive cell model is obtained, the study will shift into adopting a  $2 \times 2 \times 2$  supercell model, in which the electronic structure, hole effective masses, and optical properties will be re-determined and evaluated against the primitive cell model for the purpose of ensuring that the chosen parameters of the calculation – which are motivated by the capabilities of the LEAP cluster, a high performance computing cluster maintained by the Division of Information Technology at Texas State, upon

which the calculations are run – are sufficient to accurately model the structure and give confidence to the results obtained for the defective and doped systems.

### 3.2. Structural Properties

The optimized lattice constants used to obtain the total crystal energy normalized by the number of atoms in the unit cell,  $E_{\text{tot}}/\text{atom}$ , are given in Tab. 3.1 for CAO and 3.2 for AAO. Here, the lattice constants for the  $\alpha$ -3R<sub>R</sub> polymorph are given in the  $\alpha$ -3R<sub>CH</sub> representation for ease of comparison. All CAO optimized constants have a percent error lower than 1.5%, showing good agreement with theoretical [27, 80] and experimental [80] values. Regarding the AAO optimized

Table 3.1: The optimized lattice constants of CAO using PBE.

Phase	Const.	This Work (Å)	Other Work (Å)	% Diff.	Exp. (Å)	% Error
$\alpha - 2\text{H}$	$a$	2.8797	2.8646 [80]	0.53	2.8630 [80]	0.58
	$c$	11.4248	11.282 [80]	1.26	11.3140 [80]	0.98
	$u = c/a$	3.9647	3.9384	0.67	3.9518	0.40
$\alpha - 3\text{R}_{\text{CH}}$	$a$	2.8844	2.8844 [27]	0	2.8567 [7]	0.97
	$c$	17.1240	17.1389 [27]	0.09	16.943 [7]	1.07
	$u = c/a$	5.9368	5.9419	0.09	5.931	-
$\alpha - 3\text{R}_{\text{R}}$	$a$	2.8844	2.8844 [27]	0	2.8567 [7]	0.97
	$c$	17.1256	17.1389 [27]	0.08	16.943 [7]	1.07
	$u = c/a$	5.9373	5.9419	0.08	5.931	0.11
$\beta$	$a$	5.3048	-	-	-	-
	$b$	6.5167	-	-	-	-
	$c$	5.3153	-	-	-	-

lattice constants, the  $\alpha$ -2H,  $\alpha$ -3R<sub>CH</sub>, and  $\alpha$ -3R<sub>R</sub> all show high agreement with the associated theoretical values [16, 27], but there is less agreement with the theoretical constants of the  $\beta$  polymorph reported by Reshak [16], specifically for the  $b$  constant, which has a percent difference of 19.60%. However, more importantly, there is good agreement with the optimized constants and their experimental [16] values, with the error in  $b$  being only 2.30%. With all XTO polymorph structures

Table 3.2: The optimized lattice constants of AAO using PBE.

Phase	Const.	This Work (Å)	Other Work (Å)	% Diff.	Exp. (Å)	% Error -
$\alpha - 2\text{H}$	$a$	2.9164	-	-	-	-
	$c$	12.3482	-	-	-	-
	$u = c/a$	4.2341	-	-	-	-
$\alpha - 3\text{R}_{\text{CH}}$	$a$	2.9175	2.9211 [27]	0.12	2.890 [25]	0.95
	$c$	18.5049	18.6017 [27]	0.52	18.350 [25]	0.84
	$u = c/a$	6.3427	6.3680	0.40	6.349	0.10
$\alpha - 3\text{R}_{\text{R}}$	$a$	2.9170	2.9211 [27]	0.14	2.890 [25]	0.93
	$c$	18.5406	18.6017 [27]	0.33	18.350 [25]	1.04
	$u = c/a$	6.3560	6.3680	0.19	6.349	0.11
$\beta$	$a$	5.4508	5.2728 [16]	3.32	5.4306 [16]	0.37
	$b$	7.0147	5.7628 [16]	19.60	6.9802 [16]	0.49
	$c$	5.4986	5.3626 [16]	2.51	5.3751 [16]	2.30

optimized in the PBE method, their total energies may be compared after normalizing by the number of atoms in each respective unit cell. At this stage, the ratio of the optimized lattice constants,  $u = c/a$ , are held fixed for total energy calculations for a series of volumes around – and including – the relaxed volume (using the optimized lattice parameters). Then this series is fitted by the Birch-Murnaghan equation of state from section 2.4, from which the minimum energy from the fit corresponds to the minimum total crystal energy of the relaxed structure. The results, plotted in Fig. 3.1, show the total energies calculated by VASP as x’s and the equation of state as a line, both in colors corresponding to each polymorph, plotted against the unit cell volume after normalizing by each respective relaxed volume. Clearly, the  $\beta$  polymorph corresponding to the orthorhombic phase has an unambiguously higher total energy than the  $\alpha$ - 2H and 3R polymorphs associated with the hexagonal phases. The normalized total energies are presented in Tab. 3.3. For the  $\alpha$ -2H and  $\alpha$ -3R polymorph modeled using the conventional hexagonal unit cell, the minimum energy calculated by the Gibbs2 code is identical for CAO and AAO. The minimum total energy calculated by VASP

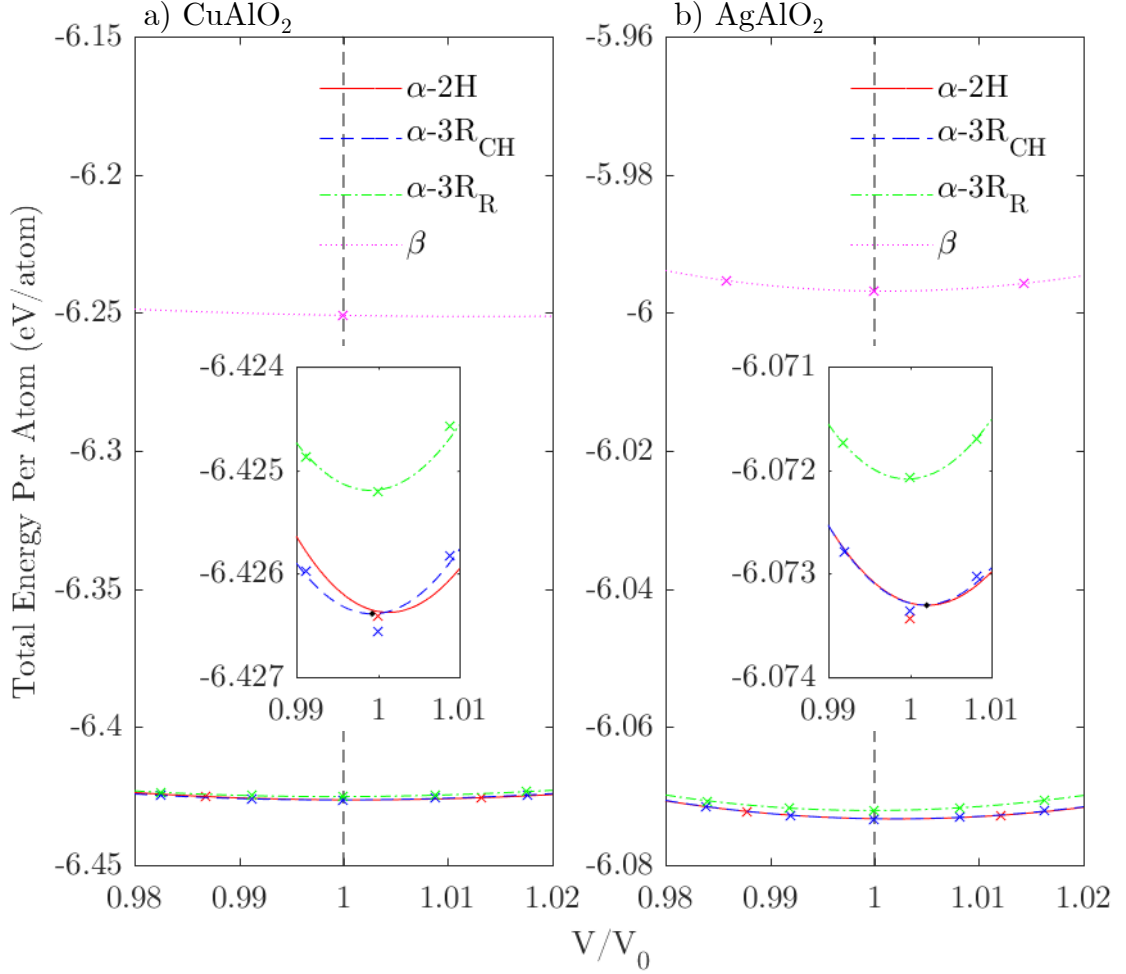


Figure 3.1: Total crystal energies normalized by the number of atoms in each unit cell versus the volume of the unit cell normalized by each relaxed volume for a) CAO and b) AAO using PBE.

using the optimized lattice constants shows  $\alpha$ -3R<sub>CH</sub> to have a slightly lower total energy (-6.4266 eV) than  $\alpha$ -2H (-6.4264 eV) for CAO, but results using VASP show the opposite for AAO (-6.07336 eV and -6.07343 eV). From both the VASP and Gibbs2 data, the  $\alpha$ -3R polymorph modeled using the rhombohedral primitive cell shows the  $\alpha$ -3R<sub>R</sub> polymorph to be  $5 \times 10^{-4}$  ( $8 \times 10^{-4}$ ) eV higher in total energy than  $\alpha$ -2H CAO(AAO). The similarity of the total energies of the 2H and 3R polymorphs is consistent with the only difference in the two crystal structures being a rotation of every third 2H layer by an angle  $\pi$  to obtain the 3R polymorph, resulting in no

change to coordination or bond lengths. These calculations suggest that the  $\alpha$ -2H polymorph may have the lowest crystal energy in the ground state. However, referring to Tabs. 3.1 and 3.2, the optimized lattice constants used to obtain these results are slightly higher than the experimentally measured values, which may bring ambiguity to the results obtained through the Gibbs2 code. Considering that the  $\alpha$ -3R polymorph is the most thoroughly studied in the literature, and since the total energy calculations using the PBE method in this study support the idea that the  $\alpha$ -2H polymorph may be just as stable as  $\alpha$ -3R, the remainder of this study is devoted to the 2H polymorph of XTO.

Table 3.3: The XAO total energies normalized by the number of atoms in each unit cell,  $E_{\text{tot}}/\text{atom}$ , using PBE.

	Phase	$E_{\text{tot}}/\text{atom}$ (eV)
CuAlO <sub>2</sub>	$\alpha - 2\text{H}$	-6.4264
	$\alpha - 3\text{R}_{\text{CH}}$	-6.4264
	$\alpha - 3\text{R}_{\text{R}}$	-6.4252
	$\beta$	-6.2514
AgAlO <sub>2</sub>	$\alpha - 2\text{H}$	-6.0734
	$\alpha - 3\text{R}_{\text{CH}}$	-6.0734
	$\alpha - 3\text{R}_{\text{R}}$	-6.0720
	$\beta$	-5.9968

As discussed in the computational methodology (section 2.5), modeling XCO’s tertiary helical magnetic moment structure would require the use of the non-collinear version of VASP, and a unit cell much larger than the primitive unit cell which only contains two Cr atoms. These two requirements would make computation of the pristine crystal quite taxing, and the supercell defect and doped systems even more so. Models in the literature side-step the need for non-collinear DFT-based calculations by adopting a simple AFM configuration where each Cr nucleus has a magnetic moment antiparallel to the other and aligned along the  $c$ -axis. Thus, it is necessary to show that adopting the simple AFM configuration

still results in a model accurate enough to be capable of offering useful predictions. In similar rationale to the total energy evaluation of the XAO polymorphs, the AFM configuration of XCO should have the lowest total ground state energy of the three studied configurations, the other two being the nonmagnetic NM – where the magnetic moments are ignored in the calculation – and FM with parallel Cr magnetic moments. Using the same method for evaluating the total ground state energy of the XAO polymorphs, the normalized total energy for each magnetic configuration against the normalized crystal volume is presented in Fig 3.2, with the minimum energies obtained from Gibbs2 reported in Tab. 3.4. The VASP and Gibbs2 data show the NM configuration to have the highest total energy. The VASP results give a slightly lower total energy for the AFM configuration, -7.1967(-6.8610) eV, than the FM configuration, -7.1964(-6.8580) eV, for CCO(ACO). However, the Gibbs2 data show that in both materials the FM configuration is less than 0.1 eV lower in energy than the AFM configuration. Although it may be ambiguous given the contradictory results that the AFM configuration is the most stable, it is predicted to be at least as stable as the FM configuration, and for that reason the AFM configuration will be used in this study to allow the results obtained for the XCO defect and doped systems to be compared to other first principles results in literature.

Table 3.4: The XCO total energies normalized by the number of atoms in each unit cell,  $E_{\text{tot}}/\text{atom}$ , using PBE.

	Config.	$E_{\text{tot}}/\text{atom}$ (eV)
CuCrO <sub>2</sub>	NM	-6.9688
	FM	-7.2050
	AFM	-7.1966
AgCrO <sub>2</sub>	NM	-6.5506
	FM	-6.8626
	AFM	-6.8608

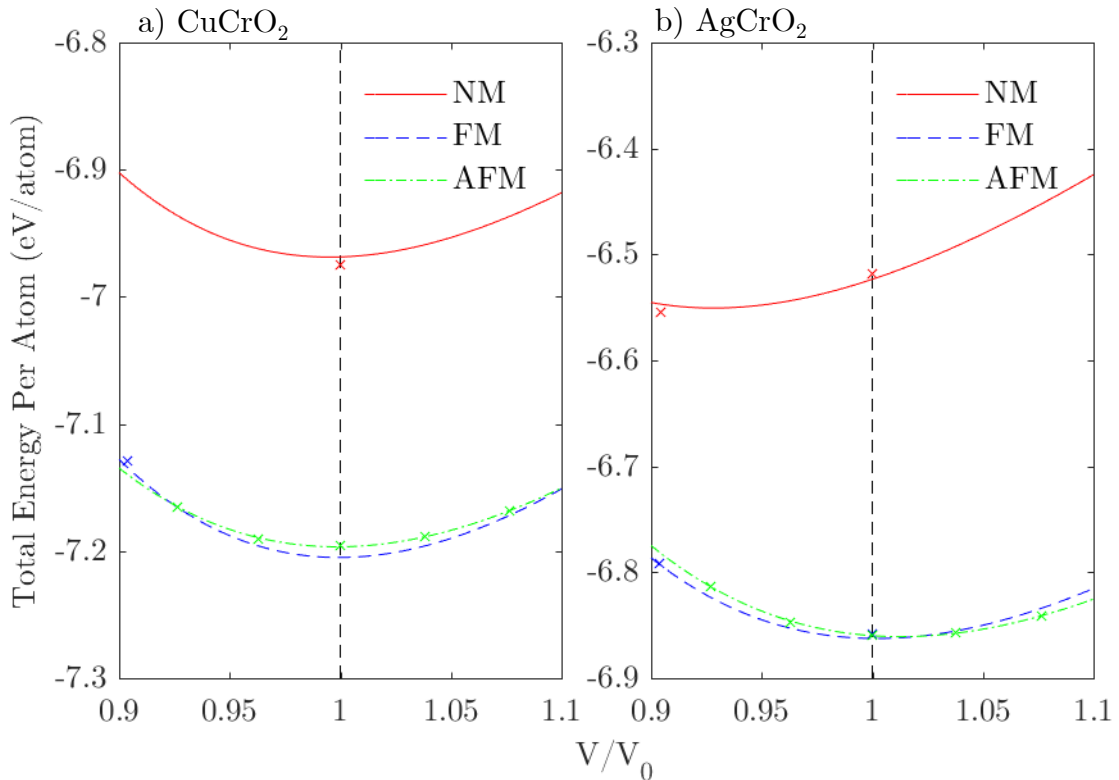


Figure 3.2: Total crystal energies normalized by the number of atoms in each unit cell versus the volume of the unit cell normalized by each relaxed volume for a) CCO and b) ACO using PBE.

With a rationale for a focused study on 2H XTO and a simple AFM configuration for XCO, it is now necessary to justify the choice of Hubbard correction what will be used with the PBE and PBE+MBJ exchange and correlation energy functionals when choosing which functional approach will produce the most accurate band gap. In accordance with the method described by Van de Walle, the static dielectric constant,  $\epsilon_\infty$ , for each 2H XTO crystal is first determined along with the unscreened Hubbard correction,  $U_{\text{unscr}}$ , for each atom in vacuum using the ATOM code. The screened Hubbard corrections,  $U_{\text{scr}}$  are used in the remainder of this work and are presented with the unscreened values and the static dielectric constant obtained in the PBE method in Tab. 3.5.

As will be discussed in the proceeding section, the PBE+U method most

Table 3.5: The 2H XTO Hubbard corrections, where  $\epsilon_\infty$  is the static dielectric constant,  $U_{\text{unscr}}$  is the unscreened Hubbard parameter in vacuum, and  $U_{\text{scr}} = U_{\text{unscr}}/\epsilon_\infty$  is the screened Hubbard parameter in the crystal, using PBE.

	$\epsilon_\infty$	$U_{\text{unscr}}$ (eV)	$U_{\text{scr}}$ (eV)
CuAlO <sub>2</sub> :Cu	5.6944	18.4477	3.2368
AgAlO <sub>2</sub> :Ag	5.9282	14.5058	2.4469
CuCrO <sub>2</sub> :Cu	9.2486	18.4477	1.9947
CuCrO <sub>2</sub> :Cr	9.2486	20.3871	2.2044
AgCrO <sub>2</sub> :Ag	11.2699	14.5058	1.2871
AgCrO <sub>2</sub> :Cr	11.2699	20.3871	1.8090

accurately models the 2H XTO direct bang gaps, which are the most relevant for optical properties (since they do not require phonon generation to conserve wave number). With that in mind, the optimized lattice constants, bond lengths  $d_{\text{X-O}}$  and  $d_{\text{T-O}}$ , bulk modulus  $B_0$  at zero Kelvin and its associated pressure derivative,  $\partial B/\partial P$ , are presented in Tab. 3.6. Also presented in Tab. 3.6 are the 2H XTO cohesive energies, defined as  $E_{\text{coh}} = 2E_{\text{tot}}^{\text{X}} + 2E_{\text{tot}}^{\text{T}} + 2E_{\text{tot}}^{\text{O}_2} - E_{\text{tot}}^{2\text{HXTO}}$ , where  $E_{\text{tot}}^{\text{X}}$ ,  $E_{\text{tot}}^{\text{T}}$ , and  $E_{\text{tot}}^{\text{O}_2}$  are the total energies of X, T, and O<sub>2</sub> in vacuum and  $E_{\text{tot}}^{2\text{HXTO}}$  is the total ground state energy of 2H XTO calculated using the PBE method only. The decision to calculate the 2H XTO cohesive energies using only the PBE method is motivated by the fact that the Hubbard correction is only intended to widen the band gap by means of adjusting the inter-energy transitions of the X atom  $d$  orbitals, however, the total ground state energy of any system is only affected by the ground state valence configuration of the bonded atoms in the material, and thus using the Hubbard correction for the calculation of the total ground state energy is a superfluous treatment. The lattice constant  $a$  in the case of XAO does not change when optimizing the structures when beginning with the PBE lattice constants using PBE+U, however, the lattice constant  $c$  slightly decreases and further approaches the experimental values. The experimental lattice constants for CCO of

$a = b = 2.97 \text{ \AA}$  and  $c = 11.40 \text{ \AA}$  [30] are in good agreement with the optimized constants obtained in this work of  $a = 3.0308 \text{ \AA}$  and  $c = 11.4914 \text{ \AA}$ . The Cu-O bond lengths in CTO are shorter than the bond lengths in ATO, with CCO(ACO) longer than the respective bonds in CAO(AAO). This behavior has a direct effect on the lattice constant  $c$  since the X-O bond is parallel to the  $c$ -axis. The T-O bond length is only affected by the X-O bond length in a minor way (since there are three T-O bonds for every X-O bond on the same O atom), and so although the T-O length is shorter for CTO than in its corresponding ATO counterpart, the length is most dependent on the T atom, and so the physically larger valence configuration of Cr compared to Al gives ACO(CCO) a longer T-O bond length than AAO(CAO). Since the X-O bond is parallel to the  $c$ -axis it has no bearing on the lattice constant  $a$ , and thus  $a$  only depends on the T-O bond lengths.

Table 3.6: The optimized lattice constants,  $a$  and  $c$ , the ratio  $u = c/a$ , X-O and T-O bond lengths,  $d_{X-O}$  and  $d_{T-O}$  respectively, ground state bulk modulus,  $B_0$ , and pressure derivative of the ground state bulk modulus,  $\partial B/\partial P$  of XTO using PBE+U. Also presented are the XTO cohesive energies normalized by the number of atoms in the primitive cell,  $E_{\text{coh}}^{\text{PBE}}/\text{atom}$ , calculated using PBE only.

	$a$ ( $\text{\AA}$ )	$c$ ( $\text{\AA}$ )	$u$	$d_{X-O}$ ( $\text{\AA}$ )	$d_{T-O}$ ( $\text{\AA}$ )	$B_0$ (GPa)	$\partial B/\partial P$	$E_{\text{coh}}^{\text{PBE}}/\text{atom}$ (eV)
CuAlO <sub>2</sub>	2.8797	11.3918	3.9560	1.8804	1.9278	169.92	4.41	34.2563
AgAlO <sub>2</sub>	2.9164	12.3329	4.2288	2.1215	1.9391	151.71	4.70	31.4283
CuCrO <sub>2</sub>	3.0308	11.4914	3.7912	1.8959	2.0040	165.35	4.67	38.0474
AgCrO <sub>2</sub>	3.0322	12.5225	4.1298	2.1254	2.0187	143.71	5.00	35.3601

### 3.3. Electronic Properties

The XAO and 2H XCO crystal structures have been optimized in the PBE method and the choice for studying the  $\alpha$ -2H XTO polymorph with a simple AFM configuration for XCO has been validated. Additionally, looking ahead at the result that the PBE+U method using the screened Hubbard corrections from Tab. 3.5 most accurately replicates the band gaps of 2H XTO, several structural parameters

for 2H XTO were calculated using the PBE+U method. Now it is appropriate to give attention to the electronic structures of the pristine crystals and compare them to experimental results from the literature. The paths taken through the Brillouin zones when calculating the band structure are  $\Gamma \rightarrow M \rightarrow L \rightarrow A \rightarrow \Gamma \rightarrow K \rightarrow H$  for the hexagonal lattice,  $\Gamma \rightarrow F \rightarrow L \rightarrow Z \rightarrow \Gamma$  for the rhombohedral lattice, and  $\Gamma \rightarrow Y \rightarrow S \rightarrow X \rightarrow U \rightarrow R \rightarrow \Gamma$  for the orthorhombic lattice. The fractional coordinates in terms of the reciprocal lattice vectors are given in Tab. 3.7. All paths are shown in Fig. 3.3. The electronic band structures and DOS for CAO and AAO obtained

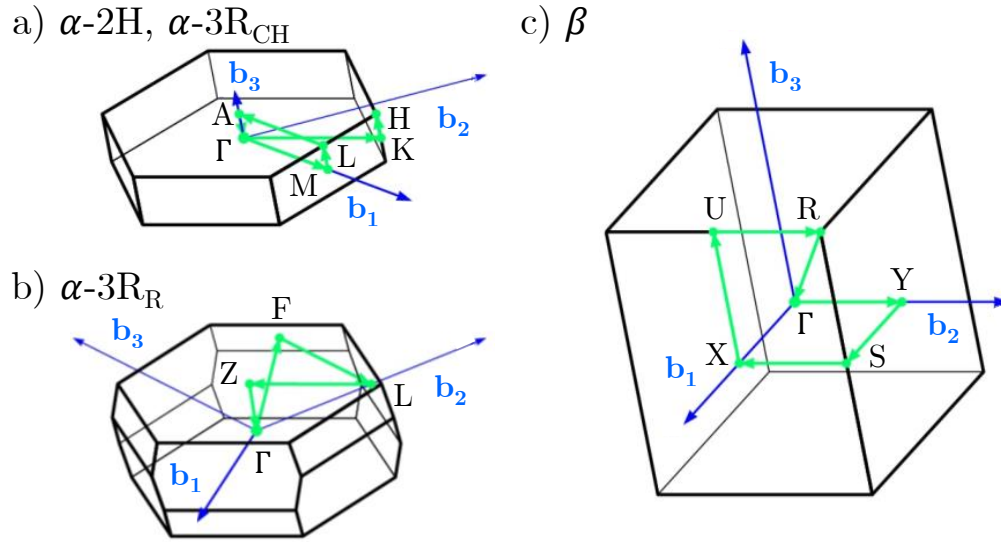


Figure 3.3: Brillouin zone paths through the a) hexagonal, b) rhombohedral, and c) orthorhombic unit cells used in calculating the electronic band structure.

in the PBE method are plotted in Figs. 3.4 and 3.5 respectively. In all of the band structure and DOS plots presented in this work, the Fermi energy,  $E_F$ , is set at zero and is defined as the maximum energy of a valence electron in the ground state.

The delafossite polymorphs of CAO are predicted to be indirect band gap materials, with an indirect transition from  $H \rightarrow \Gamma$  in the 2H polymorph and from  $M \rightarrow \Gamma$  in  $\alpha\text{-}3R_{CH}$  CAO, which corresponds to a transition from  $F \rightarrow \Gamma$  in  $\alpha\text{-}3R_R$ . The  $\beta$  polymorph is predicted to be a direct band gap material with a significantly smaller band gap than the  $\alpha$  polymorphs. For all 2H CAO delafossites, the direct band gap

Table 3.7: The high symmetry points used in the paths through the Brillouin zones of each polymorph expressed as fractional coordinates of the respective reciprocal lattice vectors.

Phase	High sym. pts.	Frac. coord.
$\alpha - 2\text{H}, \alpha - 3\text{R}_{\text{CH}}$	$\Gamma$	(000)
	M	$(\frac{1}{2}00)$
	L	$(\frac{1}{2}0\frac{1}{2})$
	A	$(00\frac{1}{2})$
	K	$(\frac{1}{3}\frac{1}{3}0)$
	H	$(\frac{1}{3}\frac{1}{3}\frac{1}{2})$
$\alpha - 3\text{R}_{\text{R}}$	$\Gamma$	(000)
	F	$(0\frac{1}{2}\frac{1}{2})$
	L	$(0\frac{1}{2}0)$
	Z	$(\frac{1}{2}\frac{1}{2}\frac{1}{2})$
$\beta$	$\Gamma$	(000)
	Y	$(0\frac{1}{2}0)$
	S	$(\frac{1}{2}\frac{1}{2}0)$
	X	$(\frac{1}{2}00)$
	U	$(\frac{1}{2}0\frac{1}{2})$
	R	$(\frac{1}{2}\frac{1}{2}\frac{1}{2})$

is located at the M point. In AAO, the delafossite polymorphs are also indirect band gap materials, with a direct gap also located at the M point, but the indirect band gap is from  $\text{H} \rightarrow \Gamma$ . The  $\beta$  AAO polymorph also has a smaller band gap than the corresponding delafossites but is also predicted as an indirect band gap material, with a transition from  $\text{R} \rightarrow \Gamma$  and a direct gap at a location between R and  $\Gamma$ . The band gap values for all polymorphs of XAO using the PBE method are presented in Tab. 3.8. It is clear from the experimental values for the  $\alpha$ -3R polymorphs that the PBE method has underestimated the direct band gaps. It is well known that the band gaps obtained with DFT are underestimated since it is intended to be an accurate theory of the ground state and error is introduced when exciting states into the conduction bands [81, 82]. Incidentally, since there are no experimental values reported specifically for the 2H delafossite polymorphs of XAO

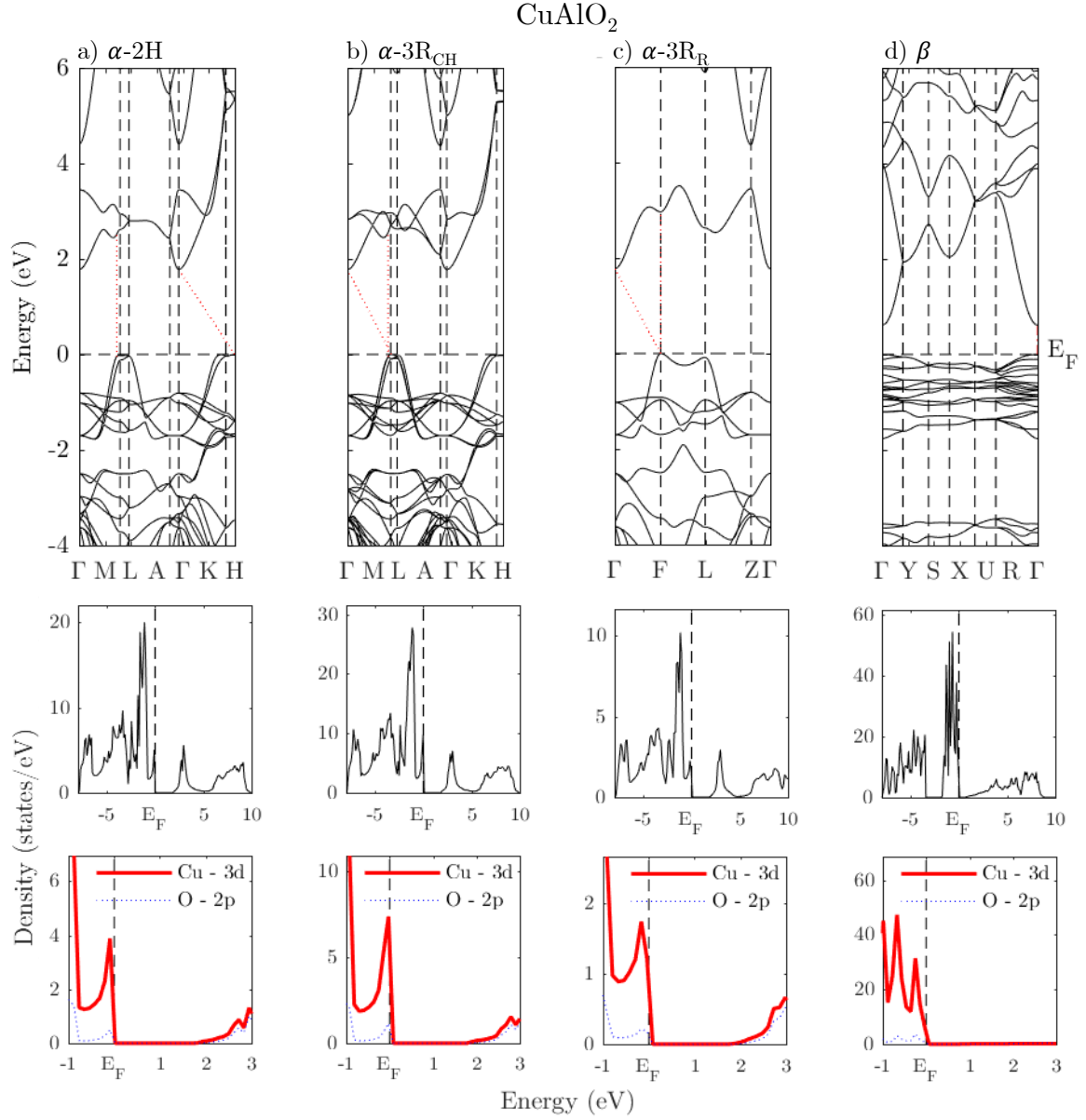


Figure 3.4: Band structures and DOS of the a)  $\alpha$ -2H, b)  $\alpha$ -3R<sub>CH</sub>, c)  $\alpha$ -3R<sub>R</sub>, and d)  $\beta$  CAO polymorphs using PBE, where the Fermi energy,  $E_F$ , is set to zero and is defined as the maximum energy of a valence electron in the ground state.

at the time of this writing, and since the crystal structures and total ground state energies are so similar for both delafossite polymorphs, the 3R direct gap will be used to evaluate the 2H direct band gaps as well. Making the approximation that the two delafossite polymorphs have the same direct band gap enables 2H XAO to

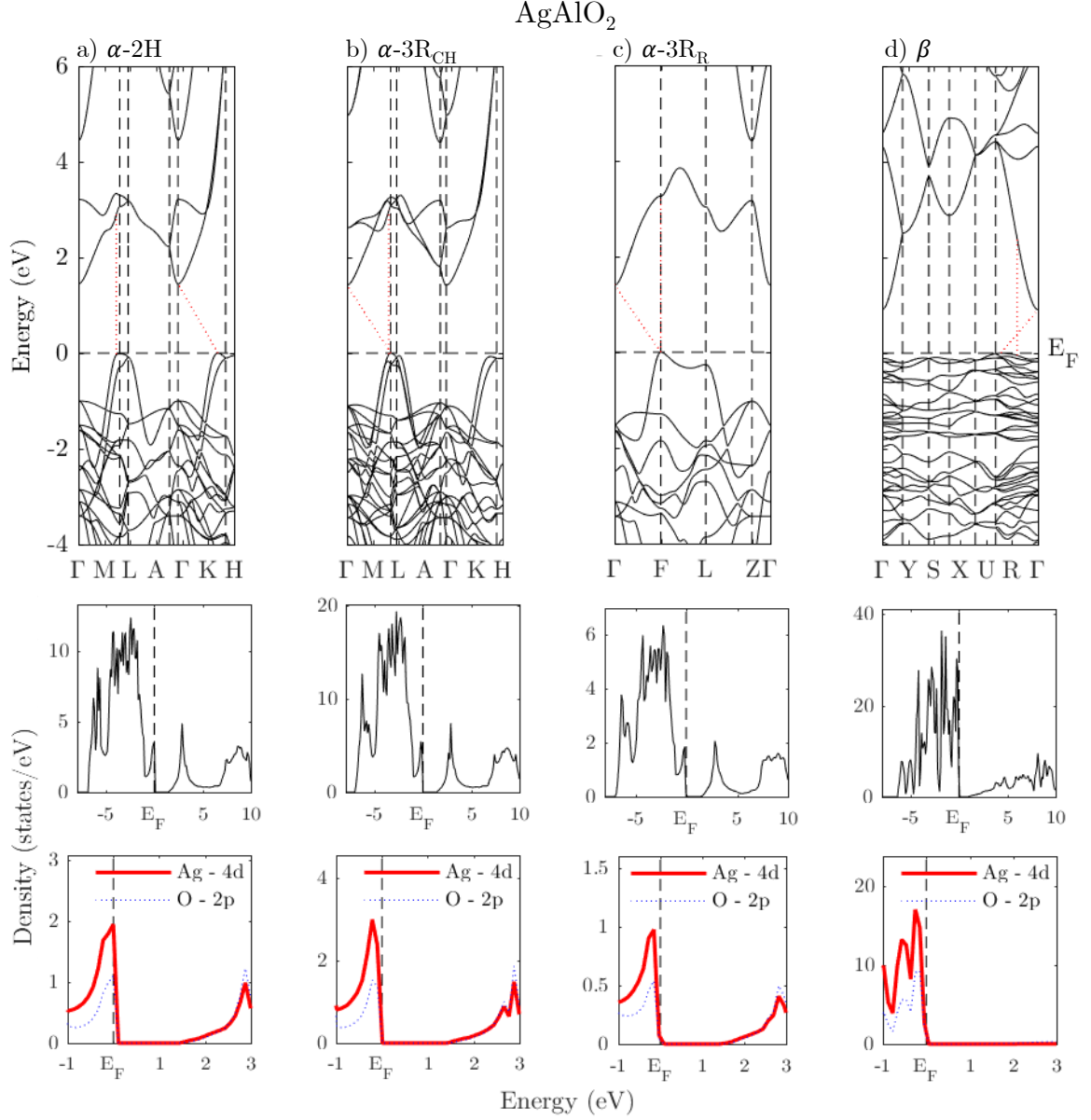


Figure 3.5: Band structures and DOS of the a)  $\alpha$ -2H, b)  $\alpha$ -3R<sub>CH</sub>, c)  $\alpha$ -3R<sub>R</sub>, and d)  $\beta$  AAO polymorphs using PBE, where the Fermi energy,  $E_F$ , is set to zero and is defined as the maximum energy of a valence electron in the ground state.

be modeled using different functionals, namely PBE, PBE+U, PBE+MBJ, PBE+MBJ+U, and HSE06 for the purpose of obtaining direct band gaps that are as close as possible to the experimental values.

The band structures for 2H XAO calculated using the previously

Table 3.8: The XAO band gaps using PBE, where  $E_{g-\text{opt}}^{\text{ind}}$  and  $E_{g-\text{opt}}^{\text{dir}}$  are the indirect and direct gaps obtained in this work, and  $E_{g-\text{exp}}^{\text{ind}}$  and  $E_{g-\text{exp}}^{\text{dir}}$  are the respective experimental values from the literature.

	Phase	$E_{g-\text{opt}}^{\text{ind}}$ (eV)	$E_{g-\text{exp}}^{\text{ind}}$ (eV)	$E_{g-\text{opt}}^{\text{dir}}$ (eV)	$E_{g-\text{exp}}^{\text{dir}}$ (eV)
CuAlO <sub>2</sub>	$\alpha - 2\text{H}$	1.7796	-	2.5594	-
	$\alpha - 3\text{R}_{\text{CH}}$	1.7766	2.99 [20]	2.6020	3.01 [21], 3.47-3.53 [6, 7, 13, 20], 3.75 [10], 3.9 [22]
	$\alpha - 3\text{R}_{\text{R}}$	1.7757		2.7122	
	$\beta$	-	-	0.6141	-
AgAlO <sub>2</sub>	$\alpha - 2\text{H}$	1.4480	-	2.4465	-
	$\alpha - 3\text{R}_{\text{CH}}$	1.4211	-	2.5246	3.6 [25]
	$\alpha - 3\text{R}_{\text{R}}$	1.4037	-	2.9159	
	$\beta$	0.9108	-	1.0248	2.81 [16], 2.95 [29]

mentioned functionals are shown in Figs. 3.6 and 3.7. Note that as implemented by the VASP code, the HSE06 functional does not allow for the same  $k$ -point to be traced more than once in the BZ path, and for that reason two separate calculations were run using the same converged charge density, each covering a unique path that produces the same overall path shown in Fig. 3.3a when catenated. The direct band gaps,  $E_{g-\text{dir}}^{\text{XAO}}$ , for XAO calculated using PBE, PBE+U, PBE+MBJ, PBE+MBJ+U, and HSE06 are shown in Tab. 3.9. For both XAO, the direct gap is overestimated by PBE+MBJ+U and HSE06 except for the direct band gap value of 3.9 eV for CAO reported by Suriwong, Thongtem, and Thongtem [22]. The PBE+MBJ method overestimates the band gap for AAO as well, and in all cases the over estimation is by roughly 0.5 eV for all reported values (up to 0.9 eV in the case of the direct band gap of 4.4858 eV for AAO calculated by PBE+MBJ+U). The PBE+U method direct band gap values,  $E_{g-\text{opt}}^{\text{dir}}$ , presented along with the associated indirect band gaps,  $E_{g-\text{opt}}^{\text{ind}}$ , are shown in Tab. 3.10. These band gaps are still roughly 0.5 eV below the experimental values, except for the value reported by Smith [21] of 3.01 eV, which has good agreement with the direct band gap of 3.0689 eV for CAO. The direct band gap of CCO (2.3869 eV) is also approximately

0.5 eV below the reported range of 2.95 – 3.3 eV [30–34]. Due to the high efficiency in computation of the PBE+U method when compared to PBE+MBJ, PBE+MBJ+U, and HSE06, as well as similar error in the direct band gap values without overestimation and an improvement in the structural parameters, the PBE+U method is adopted for the remainder of this work.

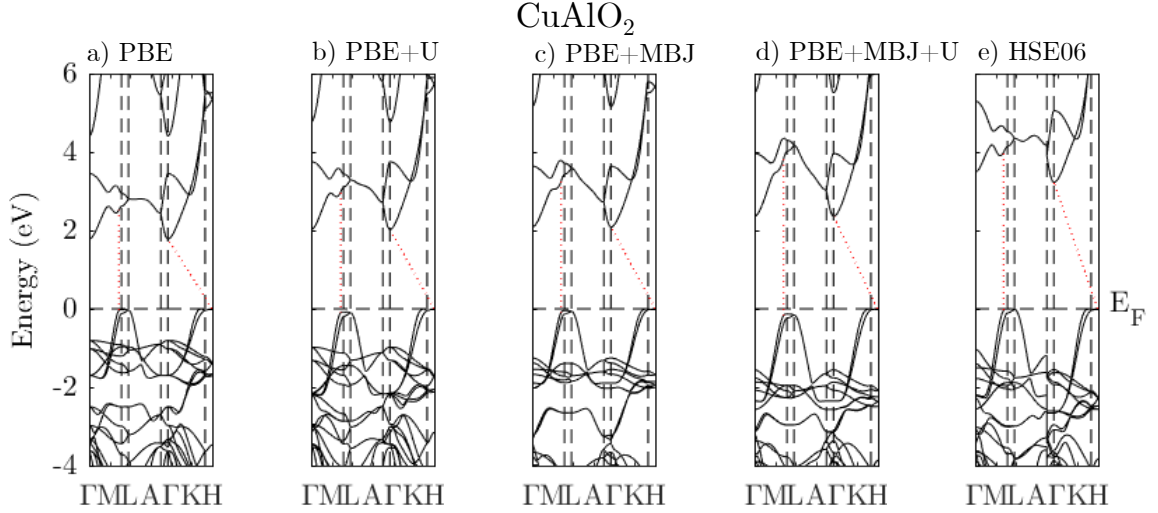


Figure 3.6: The electronic band structure for 2H CAO calculated using PBE, PBE+U, PBE+MBJ, PBE+MBJ+U, and HSE06, where the Fermi energy,  $E_F$ , is set to zero and is defined as the maximum energy of a valence electron in the ground state.

Table 3.9: The direct band gaps,  $E_{g\text{-dir}}^{\text{CAO}}$  and  $E_{g\text{-dir}}^{\text{AAO}}$ , for CAO and AAO respectively, calculated using PBE, PBE+U, PBE+MBJ, PBE+MBJ+U, and HSE06.

	$E_{g\text{-dir}}^{\text{CAO}}$ (eV)	$E_{g\text{-dir}}^{\text{AAO}}$ (eV)
PBE	2.5594	2.8798
PBE+U	3.0689	3.2545
PBE+MBJ	3.3427	4.1844
PBE+MBJ+U	3.9523	4.4858
HSE06	4.0276	3.9265

Concerning the magnetic configurations of 2H XCO, the AFM configuration not only shares the lowest total energy with FM configuration, it also has an unambiguous semiconductor nature and the larger band gap which is

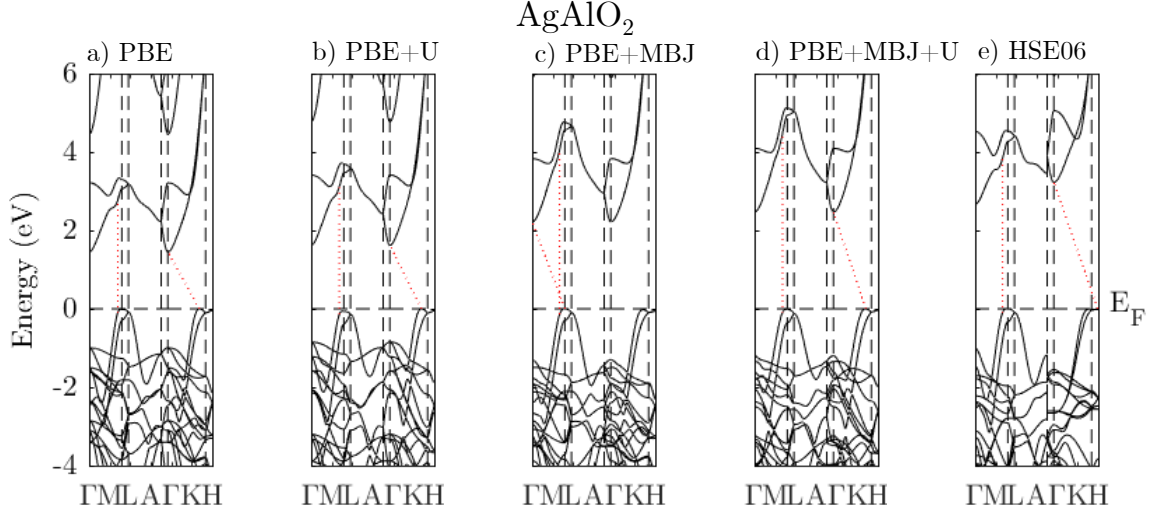


Figure 3.7: The electronic band structure for 2H AAO calculated using PBE, PBE+U, PBE+MBJ, PBE+MBJ+U, and HSE06, where the Fermi energy,  $E_F$ , is set to zero and is defined as the maximum energy of a valence electron in the ground state.

Table 3.10: The 2H XTO band gaps using PBE+U, where  $E_{g-\text{opt}}^{\text{ind}}$  and  $E_{g-\text{opt}}^{\text{dir}}$  are the indirect and direct gaps respectively.

	$E_{g-\text{opt}}^{\text{ind}}$ (eV)	$E_{g-\text{opt}}^{\text{dir}}$ (eV)
CuAlO <sub>2</sub>	2.0227	3.0689
AgAlO <sub>2</sub>	1.6202	3.2545
CuCrO <sub>2</sub>	1.7083	2.3869
AgCrO <sub>2</sub>	1.5233	2.5184

preferred for a TCO as presented in Figs. 3.8 and 3.9 along with the other configurations. The NM XCO is clearly metallic, and FM ACO exhibits shallow acceptor states (unoccupied states immediately above the Fermi energy) in addition to a small band gap with is also a characteristic of FM CCO along with strong asymmetry in the band structure across spin, making both the NFM and FM poor candidates for *p*-type TCOs. In this way the electronic structures further support using the AFM configuration with the primitive cell representation of 2H XCO.

The next step in this study is to use the optimized crystal structure in the PBE+U approach to obtain band structures and DOS of pristine 2H XTO – from now on referred to only as XTO – which will serve as a point of comparison when

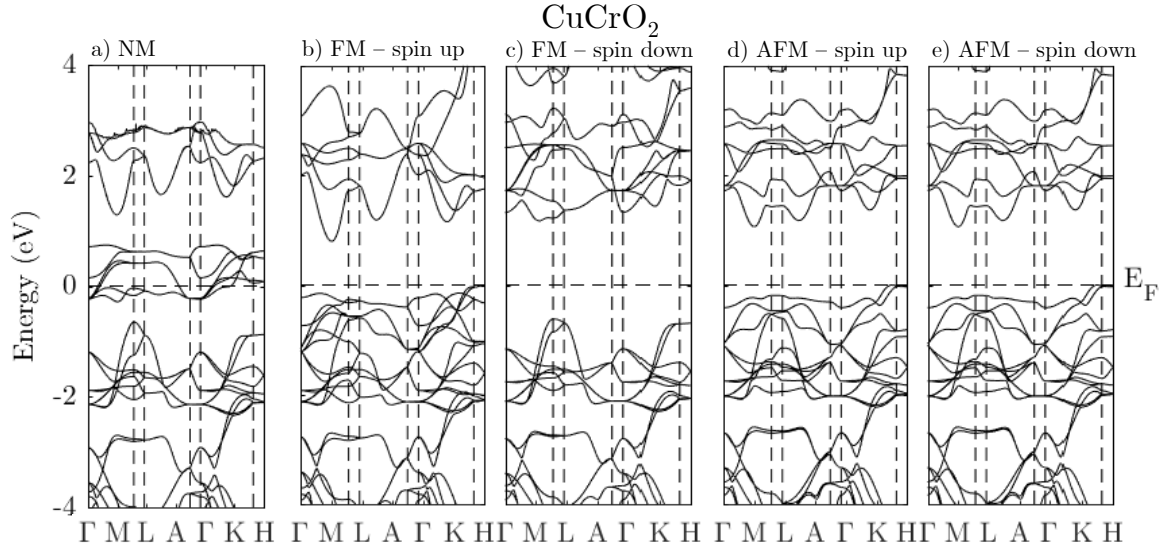


Figure 3.8: 2H CCO band structures in the a) non-magnetic (NM), b) spin-up ferromagnetic (FM), c) spin-down ferromagnetic, d) spin-up antiferromagnetic (AFM), and e) spin-down antiferromagnetic configurations using PBE, where the Fermi energy,  $E_F$ , is set to zero and is defined as the maximum energy of a valence electron in the ground state.

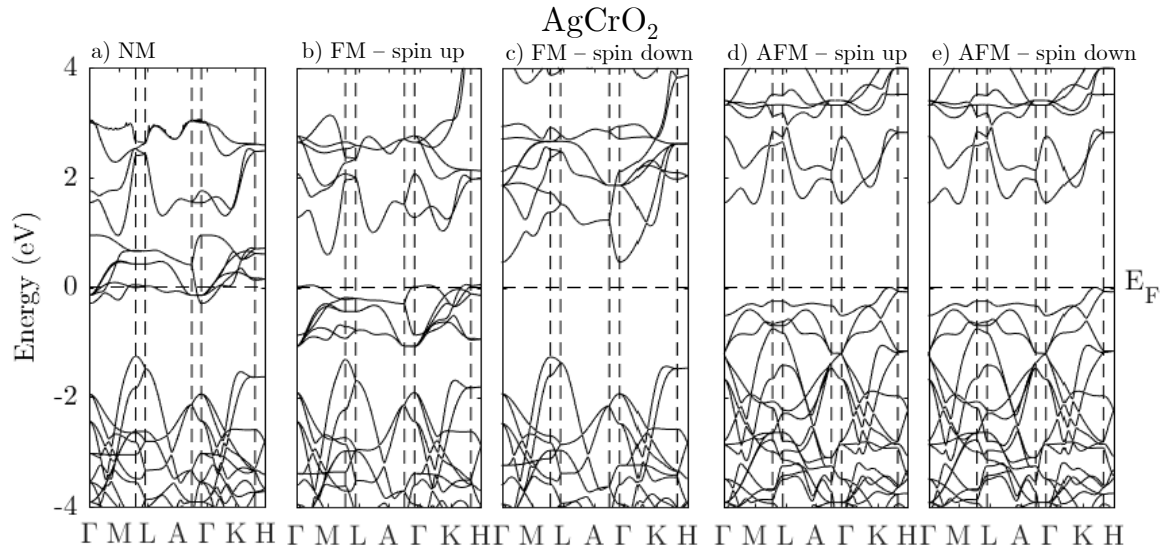


Figure 3.9: 2H ACO band structures in the a) non-magnetic (NM), b) spin-up ferromagnetic (FM), c) spin-down ferromagnetic, d) spin-up antiferromagnetic (AFM), and e) spin-down antiferromagnetic configurations using PBE, where the Fermi energy,  $E_F$ , is set to zero and is defined as the maximum energy of a valence electron in the ground state.

the supercell scheme is implemented. X behaves as  $X^+$ , T as  $T^{3+}$ , and O as  $O^{2-}$  in XTO. Figure 3.10 shows the electronic band structure and DOS for CAO. As previously stated, the delafossite XTO are indirect band gap materials, and the CAO indirect gap is from  $H \rightarrow \Gamma$ . The direct gap is located at the slightly off-M location in the direction of  $\Gamma$ . The bands around the gap are highly dispersive in the  $a - b$  plane. Local to the band gap area, the DOS in the valence band is at a maximum at -2.0 eV below the Fermi energy. There is another, smaller local maximum right below the Fermi energy, which is dominated by Cu-3d states, with minor contributions from O-2p states. Shown in panel b) of Fig. 3.10 are the band structure and DOS for AAO. The band structure is very similar to that of CAO, with the exception of the indirect gap being located at the off-K point towards  $\Gamma$  instead of the H point. The DOS are more evenly distributed than in CAO from about -1 eV to -4 eV below the Fermi energy, with contributions becoming smaller until the local maxima right below the Fermi energy that begins at about -1 eV. In AAO, the contribution of Ag-4d states near the VBM is roughly the same as O-2p states. In both XAO, the region above the CBM is equal parts Cu(Ag)-3(4)d states. The Al contributions to the DOS in XAO are negligible.

The XCO electronic band structures and DOS, which are shown in Fig. 3.11, show that the indirect gap for both materials is from the off-K point towards  $\Gamma$  to a point roughly midway between  $\Gamma$  and M. The direct gap for both materials is located at a similar off-K point. The energy bands around the band gap are less dispersive in the  $a - b$  plane as compared to XAO. The DOS in CCO have a local maximum at about -1.8 eV below the Fermi energy. There is also a small local maximum immediately below the Fermi energy. The immediate DOS below the Fermi energy are dominated by Cu-3d states, followed by similar contributions from Cr-3d and O-2p states, while in the area directly above the CBM Cr-3d states dominate the DOS followed closely by equal contributions from Cu-3d and O-2p

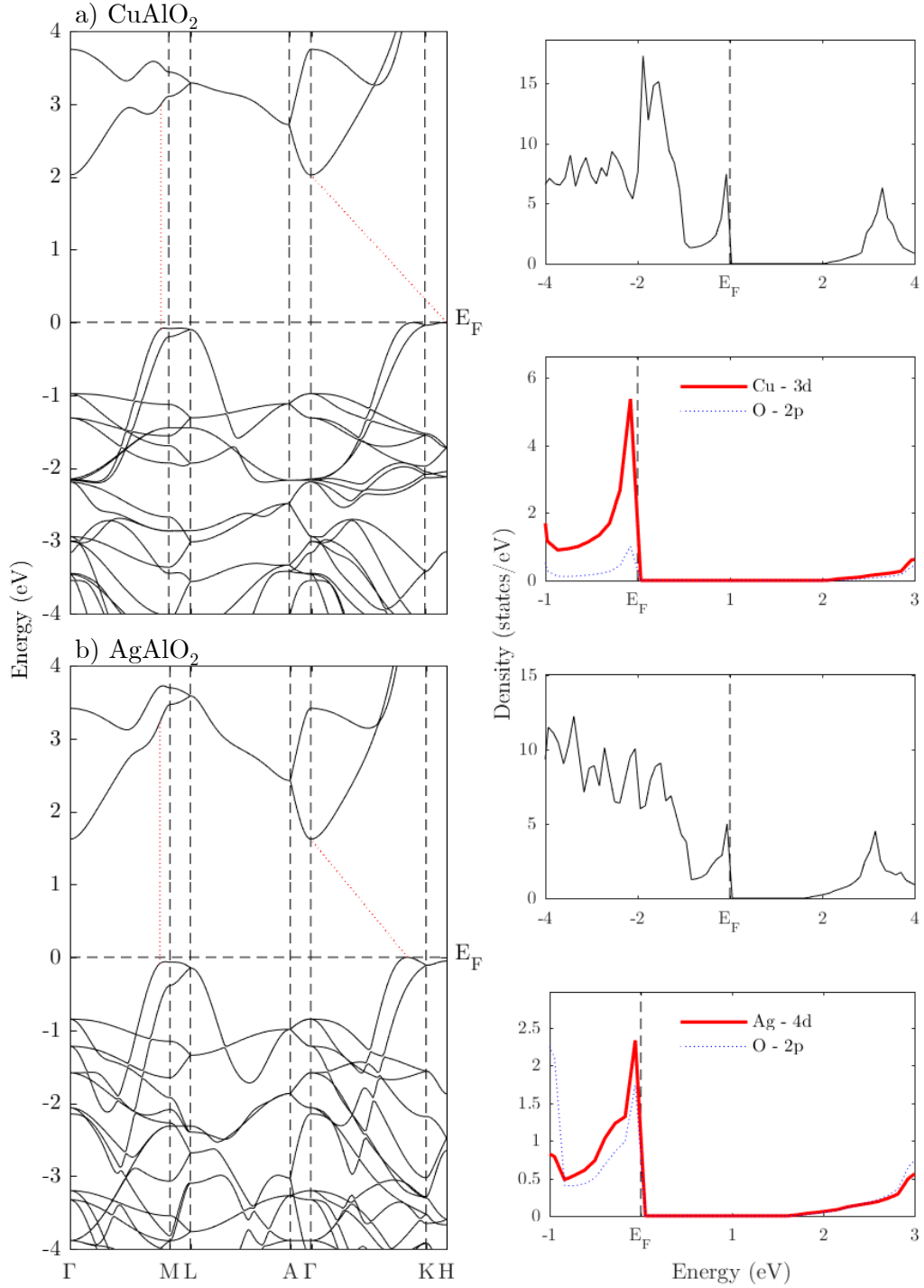


Figure 3.10: The electronic band structure and density of states for a) CAO, and b) AAO using PBE+U, where the Fermi energy,  $E_F$ , is set to zero and is defined as the maximum energy of a valence electron in the ground state.

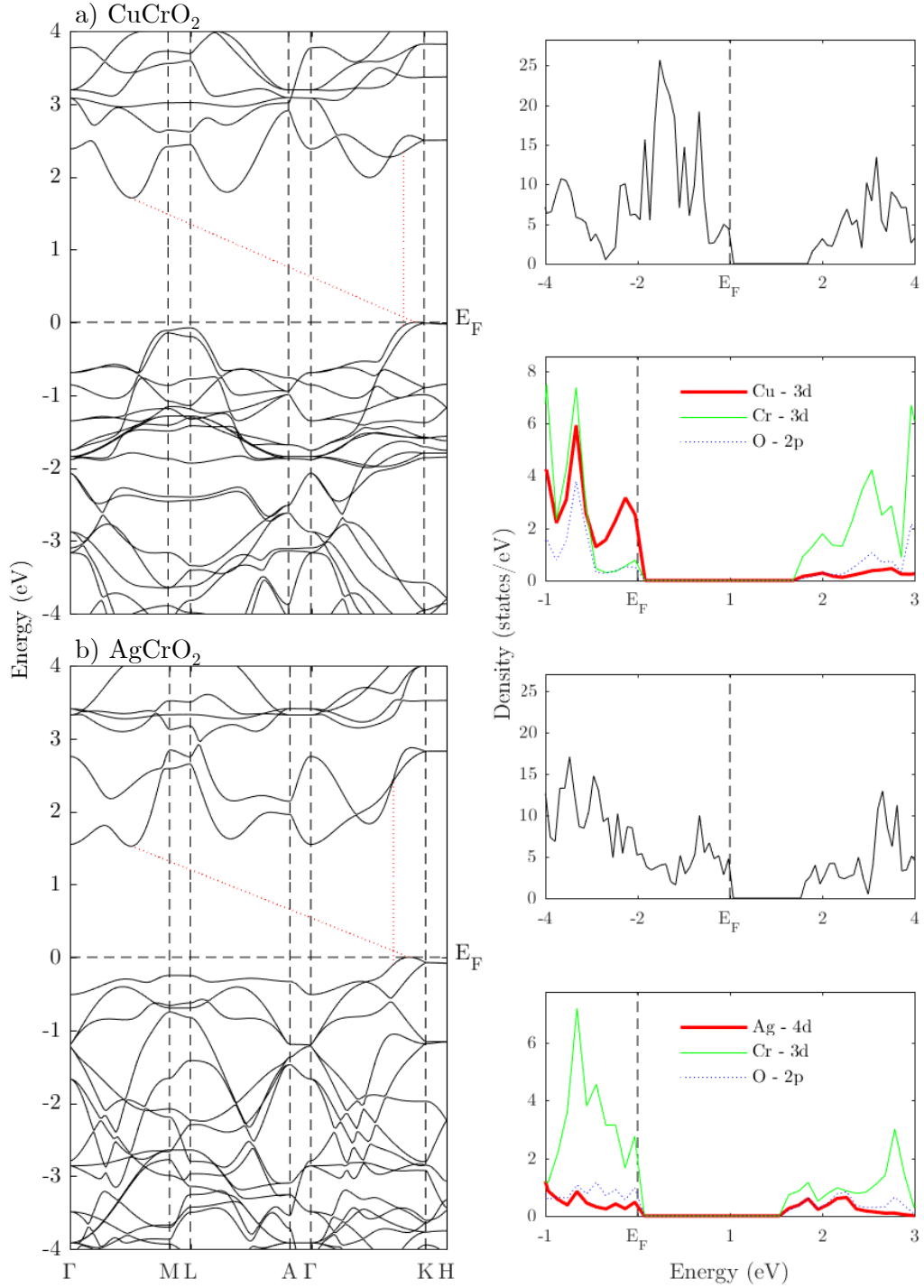


Figure 3.11: The electronic band structure and density of states for AFM a) CCO, and b) ACO using PBE+U, where the Fermi energy,  $E_F$ , is set to zero and is defined as the maximum energy of a valence electron in the ground state.

states. The DOS in ACO has the greatest local maximum at -3.5 eV, but that local maximum is only a bit more than half of the local maximum in CCO. The DOS generally decreases as energy increases from -3.5 eV until about -1.2 eV, when the DOS reaches another local maximum at -0.7 eV. This local maximum close to the band gap is dominated heavily by Cr-3*d* states, followed by O-2*p* states. Similarly to CCO, the lower conduction band states are predominantly Cr-3*d* in nature, with equal contributions from Cu-3*d* and O-2*p* states.

In order to convert to a supercell scheme and study the effects of Mg doping and Cu and O vacancies, it is important to ensure that the electronic structure of the pristine XTO crystal modeled in the  $2 \times 2 \times 2$  supercell is in good agreement with the results from the primitive cell model. In converting to a supercell, it is necessary to scale back the number of points in the k-mesh in order to prevent the computation from running out of virtual memory or creating output files that are too large to process. Reducing the k-mesh by too many points can cause the supercell results to become less accurate. As presented in Fig. 3.12, however, the folded band structures for XTO using the SC model are difficult to interpret in the context of the primitive cell model. From Fig 3.12 alone it cannot be determined if the chosen SC model accurately reproduces the results of the PC model shown in Figs. 3.10 and 3.11. Plotting the unfolded SC band structures (red x's) as obtained using the BandUP code [63,64] along with the results for the PC models (black lines) is displayed in Fig. 3.13 and shows strong agreement between the electronic band structures obtained in both models.

The charge densities, shown in Fig. 3.14, are strongly ionic in nature, with a majority of the density located at the X and O sites. The Cr nuclei in XCO have the highest density in CCO, and in general the density is greater at the Cr sites than at the Al sites in XAO. The charge density at the Al sites in CAO is negligible.

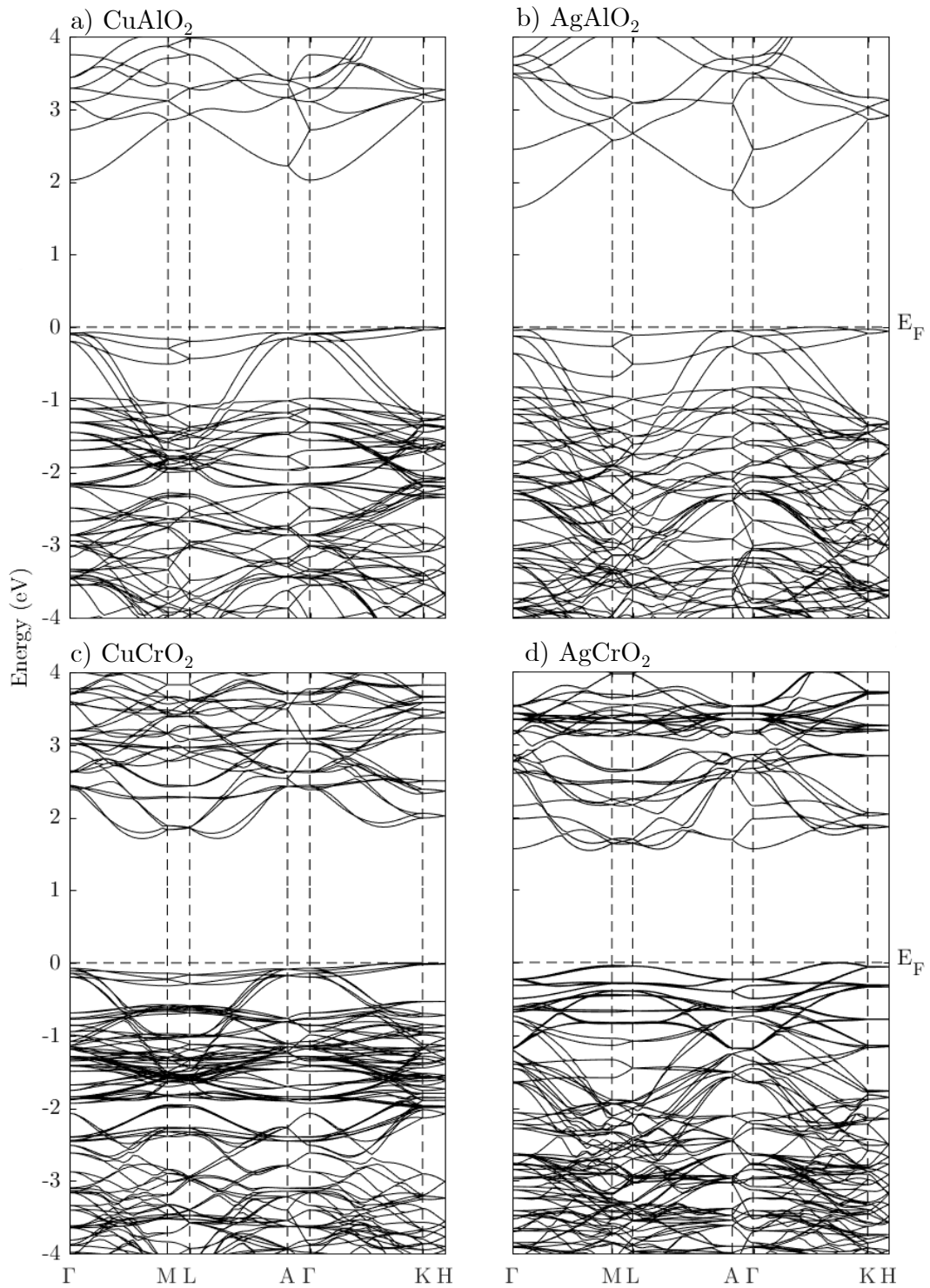


Figure 3.12: The folded electronic band structure of the a) CAO, b) AAO, c) CCO, and d) AAO supercells using PBE+U, where the Fermi energy,  $E_F$ , is set to zero and is defined as the maximum energy of a valence electron in the ground state.

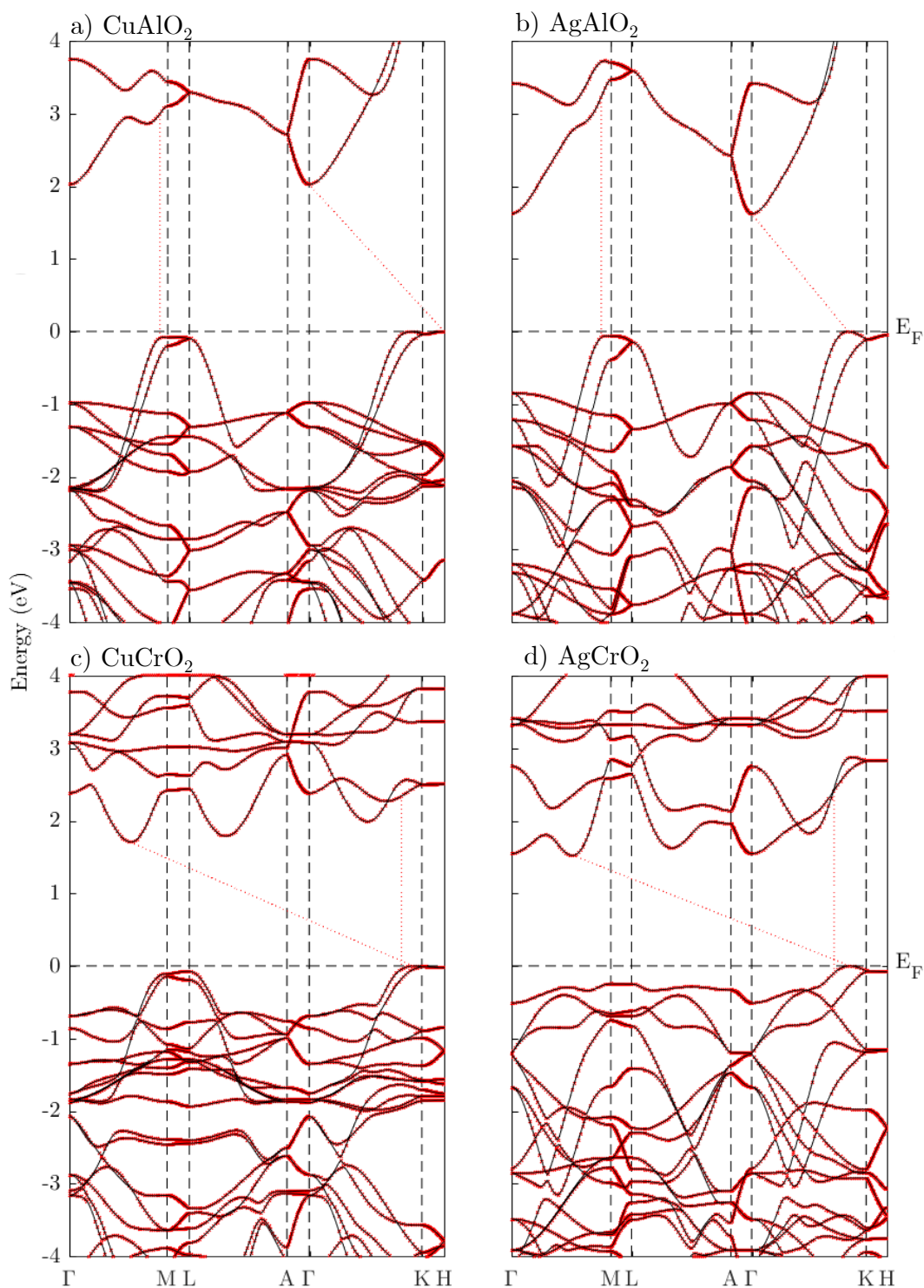


Figure 3.13: The electronic band structure of the primitive cell (solid black lines) and the supercell in the primitive cell representation (red x's) for a) CAO, b) AAO, c) CCO, and d) ACO using PBE+U, where the Fermi energy,  $E_F$ , is set to zero and is defined as the maximum energy of a valence electron in the ground state.

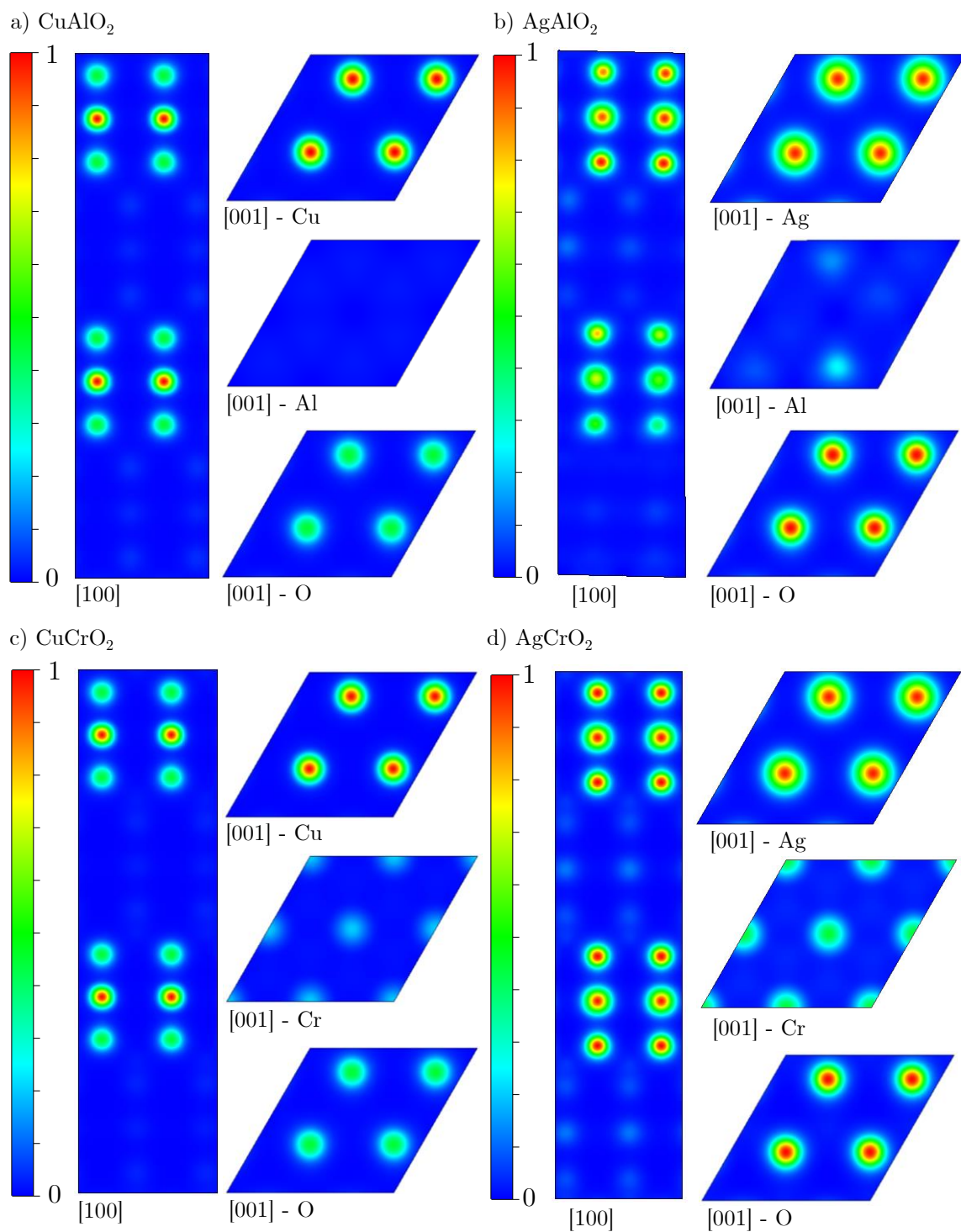


Figure 3.14: Charge density contour plots for a) CAO, b) AAO, c) CCO, and d) ACO supercells using PBE+U. The direction presented with each contour plot indicates a direction perpendicular to the plot and the atomic symbol indicates the ion in the plot.

### 3.4. Hole Effective Masses

The VBM was calculated to be at the off-M point in XAO and the off-K point in XCO, both in the direction of the  $\Gamma$  point. New paths through the BZ are defined that pass through each VBM in the [010] and [001] directions in addition to the [100] direction already covered by the initial band structure calculations. The [010] direction are not associated with a high symmetry point, but the [010] direction is towards L(H) for off-M(off-K). The reported hole effective mass,  $m_* = |m_h/m_e|$  where  $m_h$  and  $m_e$  are the measured hole effective mass and free electron mass respectively, are reported in Tab. 3.11. In all cases, the hole effective mass is

Table 3.11: The hole effective masses for XTO using the primitive cell model and PBE+U, in units of  $m_e$ , the free electron mass.

	M(K) $\rightarrow$ $\Gamma$ [100]	[010]	M(K) $\rightarrow$ L(H) [001]	avg.
CuAlO <sub>2</sub> (off-M)	0.48	2.36	2.72	1.85
AgAlO <sub>2</sub> (off-M)	0.42	1.99	1.11	1.17
CuCrO <sub>2</sub> (off-K)	2.33	2.82	4.27	3.14
AgCrO <sub>2</sub> (off-K)	1.61	1.77	6.06	3.15

smallest in the [100] direction. With the exception of AAO, the [001] direction is associated with the largest mass. Overall, the hole effective masses in XCO are larger than in XAO. Other theoretical values for the hole effective masses in XAO are reported in Tab. 3.12 and are similar with the results obtained in this work except for Cerqueira’s average value [83] of 2.66 for 3R CAO and Zhang’s reported value [1] of 38.9 for 3R CAO in the [001] direction. Tab. 3.13 shows the hole effective masses obtained for the pristine XTO crystal in the SC scheme. The values are comparable to results calculated in the PC model for XAO. However, although there is agreement between hole effective masses in the [100] direction in the PC and SC models, there is much more disagreement in the [010] and [001] directions, which leads to overall smaller hole effective masses for XCO in the SC scheme. In the case of CCO, the hole effective mass is lowest in the [001] direction. The

Table 3.12: Other theoretical hole effective masses for XTO from literature, in units of  $m_e$ , the free electron mass.

	[100]	[010]	[001]	avg.
3R CuAlO <sub>2</sub> (PBE) [27]	0.41	1.88	1.01	1.10
3R CuAlO <sub>2</sub> (PBE) [83]	-	-	-	2.66
3R CuAlO <sub>2</sub> (HSE06) [1]	-	2.6	38.9	-
AgAlO <sub>2</sub> (PBE) [27]	0.47	2.01	1.91	1.46
AgAlO <sub>2</sub> (PBE) [83]	-	-	-	1.49

discrepancies between the results in the PC and SC models is the result of a reduction of the number of  $k$  points in the  $k$ -mesh of the primitive cell and a reduction in the resolution of the energy spectrum from  $1 \times 10^{-4}$  eV in the PC model to  $1 \times 10^{-3}$  eV in the SC model as a result of the band unfolding process.

Table 3.13: The hole effective masses for XTO using the supercell scheme, in units of  $m_e$ , the free electron mass.

	M(K) $\rightarrow$ $\Gamma$ [100]	[010]	M(K) $\rightarrow$ L(H) [001]	avg.
CuAlO <sub>2</sub> (off-M)	0.47	1.54	2.22	1.41
AgAlO <sub>2</sub> (off-M)	0.42	1.72	2.03	1.39
CuCrO <sub>2</sub> (off-K)	2.05	5.23	0.81	2.70
AgCrO <sub>2</sub> (off-K)	1.25	1.76	1.99	1.67

### 3.5. Optical Properties

The optical properties of XTO are symmetric in the  $a - b$  plane. As indicated by Tab. 3.14, the static dielectric constants and refractive indices in each primitive lattice vector direction are larger for XCO than XAO, with the largest values in ACO and the smallest in CAO. In all crystals, the values are higher in the plane than perpendicular.

The frequency-dependent optical properties presented in this section, the real component of the complex dielectric function,  $\epsilon_1(\omega)$ , imaginary component of the complex dielectric function,  $\epsilon_2(\omega)$ , refractive index,  $n(\omega)$ , extinction coefficient,  $\kappa(\omega)$ , optical conductivity,  $\text{Re } \sigma(\omega)$ , absorption coefficient,  $\alpha(\omega)$ , reflectivity,  $R(\omega)$ ,

Table 3.14: The static dielectric constants,  $\epsilon_\infty$ , and refractive indices,  $n$ , in the directions  $a$ ,  $b$ , and  $c$ , corresponding to the primitive lattice vectors  $\mathbf{b}_1$ ,  $\mathbf{b}_2$ , and  $\mathbf{b}_3$ , of 2H XTO modeled in the primitive cell using PBE+U.

	$\epsilon_\infty^a$	$\epsilon_\infty^b$	$\epsilon_\infty^c$	$\epsilon_\infty^{\text{avg}}$	$n_a$	$n_b$	$n_c$	$n_{\text{avg}}$
CuAlO <sub>2</sub>	5.4141	5.4142	4.4346	5.0876	2.3268	2.3268	2.1058	2.2531
AgAlO <sub>2</sub>	5.4994	5.4999	5.5418	5.5137	2.3451	2.3452	2.3541	2.3481
CuCrO <sub>2</sub>	7.7501	7.7478	6.6488	7.3822	2.7839	2.7835	2.5785	2.7153
AgCrO <sub>2</sub>	8.0116	8.0116	7.8292	7.9508	2.8305	2.8305	2.7981	2.8197

and loss function,  $L(\omega)$ , are overlays of the results obtained using the SC model onto results obtained in the PC scheme. The component in the  $a - b$  plane is drawn in blue for the SC model and the corresponding component in the PC scheme is green. The perpendicular component in the SC model is drawn in dotted red, while the same component in the PC scheme is drawn in dashed cyan. The optical properties for CAO are shown in Fig. 3.15. The real component of the complex dielectric function of CAO shows the onset of the optical transition in the  $a - b$  plane. The overall maximum value also happens in the plane and about  $1 - 2$  eV before the corresponding maximum in the perpendicular component. A similar behavior is exhibited in the imaginary component of the complex dielectric function. These features are exhibited in the derived optical properties. There is a sharp increase in the optical conductivity oriented in the plane at about 3 eV, consistent with the optical transition in the real component of the dielectric function and the direct gap measured from the band structure. In addition to symmetry in the plane, the complex dielectric function in AAO shares more symmetry with the perpendicular component than in CAO, which can be seen in Fig 3.16. That approximate symmetry is disturbed at roughly 4.5 eV, where much more anisotropy is introduced across the two components. Unlike CAO, the complex dielectric function also exhibits a second local maximum at 5.0(6.0) eV for the perpendicular(in-plane) component. As illustrated in Fig. 3.17, there are many more features to the complex dielectric function in CCO than in XAO. First, due to

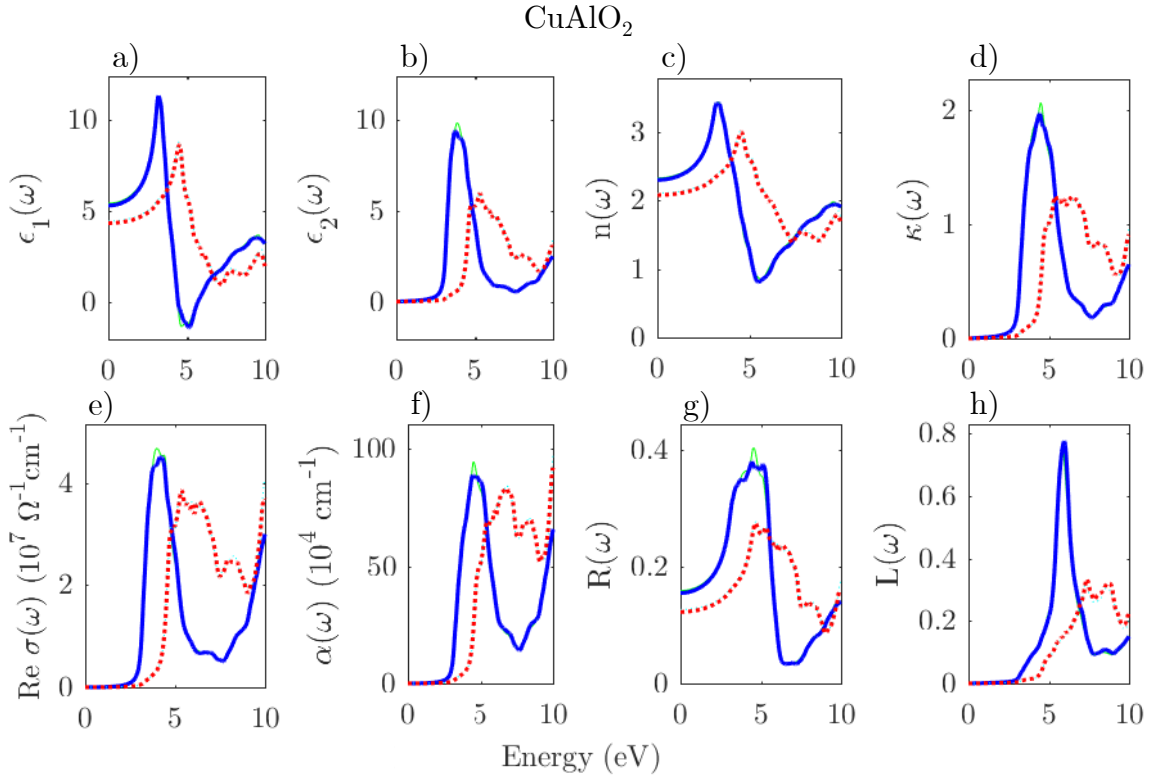


Figure 3.15: Frequency dependence of the a) real component of the complex dielectric function, b) imaginary component of the complex dielectric function, c) refractive index, d) extinction coefficient, e) optical conductivity, f) absorption coefficient, g) reflectivity, and h) loss function of CAO. The in-plane components of the supercell are drawn as a thick blue line and the perpendicular component is drawn by a thick red dashed line. The primitive cell results are plotted in the same panels for comparison, with the in-plane components drawn as a thin green line and a thin cyan dashed line for the perpendicular component.

the smaller band gap, the maximums in each component happen at lower energies, which is consistent with the direct band gap measured from the band structure.

The in-plane component is larger than the perpendicular component until about 4.0 eV, at which point the perpendicular component is larger. Although the complex dielectric function has a lower energy optical transition and many features across the spectrum similar to CCO, it differs from CCO in that the in-plane and perpendicular components alternate more often as the dominant component.

In all materials the results from the supercell scheme match closely the

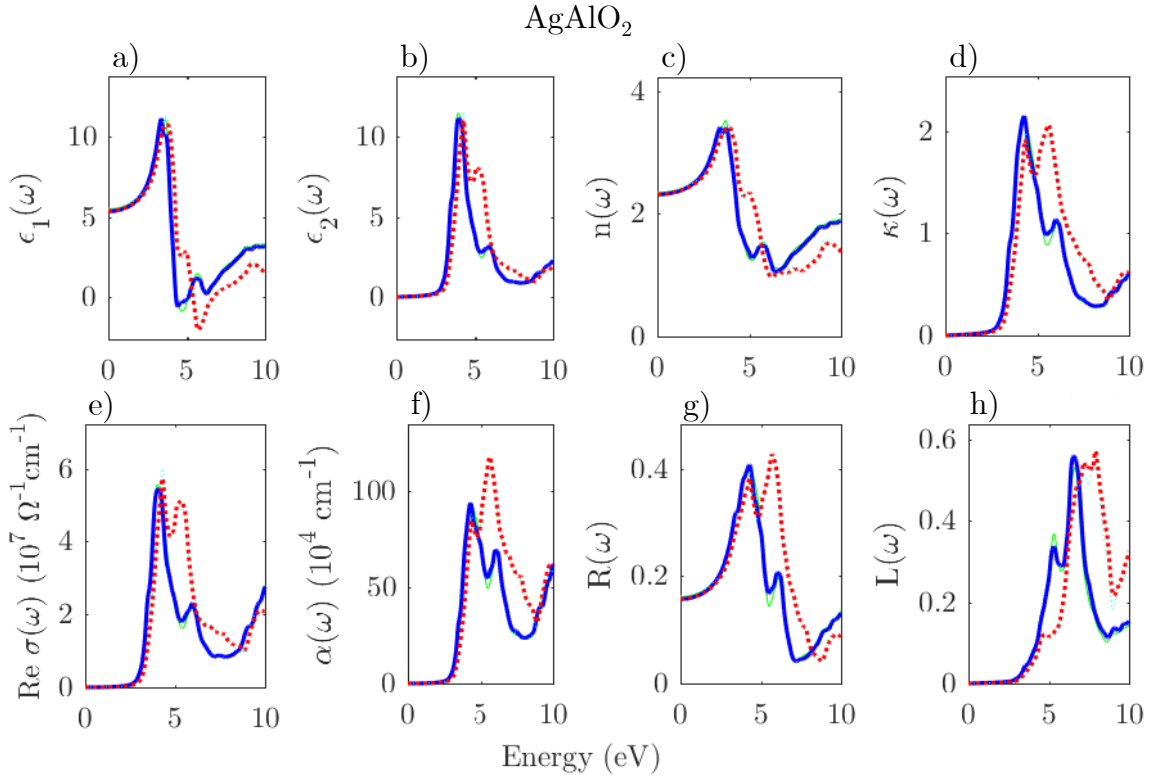


Figure 3.16: Frequency dependence of the a) real component of the complex dielectric function, b) imaginary component of the complex dielectric function, c) refractive index, d) extinction coefficient, e) optical conductivity, f) absorption coefficient, g) reflectivity, and h) loss function of AAO. The in-plane components of the supercell are drawn as a thick blue line and the perpendicular component is drawn by a thick red dashed line. The primitive cell results are plotted in the same panels for comparison, with the in-plane components drawn as a thin green line and a thin cyan dashed line for the perpendicular component.

results obtained from the PC model, indicating that the accuracy of the complex dielectric function was not appreciably affected by the reduction of  $k$ -points in the mesh used on the SC.

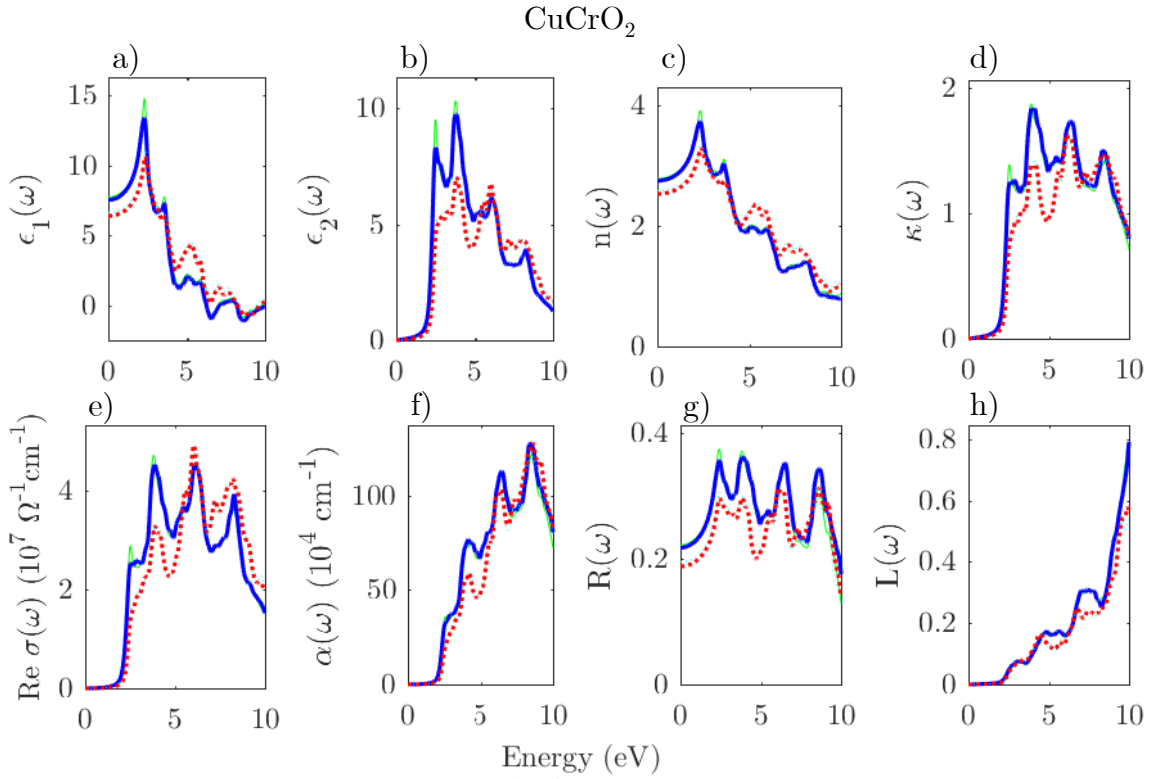


Figure 3.17: Frequency dependence of the a) real component of the complex dielectric function, b) imaginary component of the complex dielectric function, c) refractive index, d) extinction coefficient, e) optical conductivity, f) absorption coefficient, g) reflectivity, and e) loss function of CCO. The in-plane components of the supercell are drawn as a thick blue line and the perpendicular component is drawn by a thick red dashed line. The primitive cell results are plotted in the same panels for comparison, with the in-plane components drawn as a thin green line and a thin cyan dashed line for the perpendicular component.

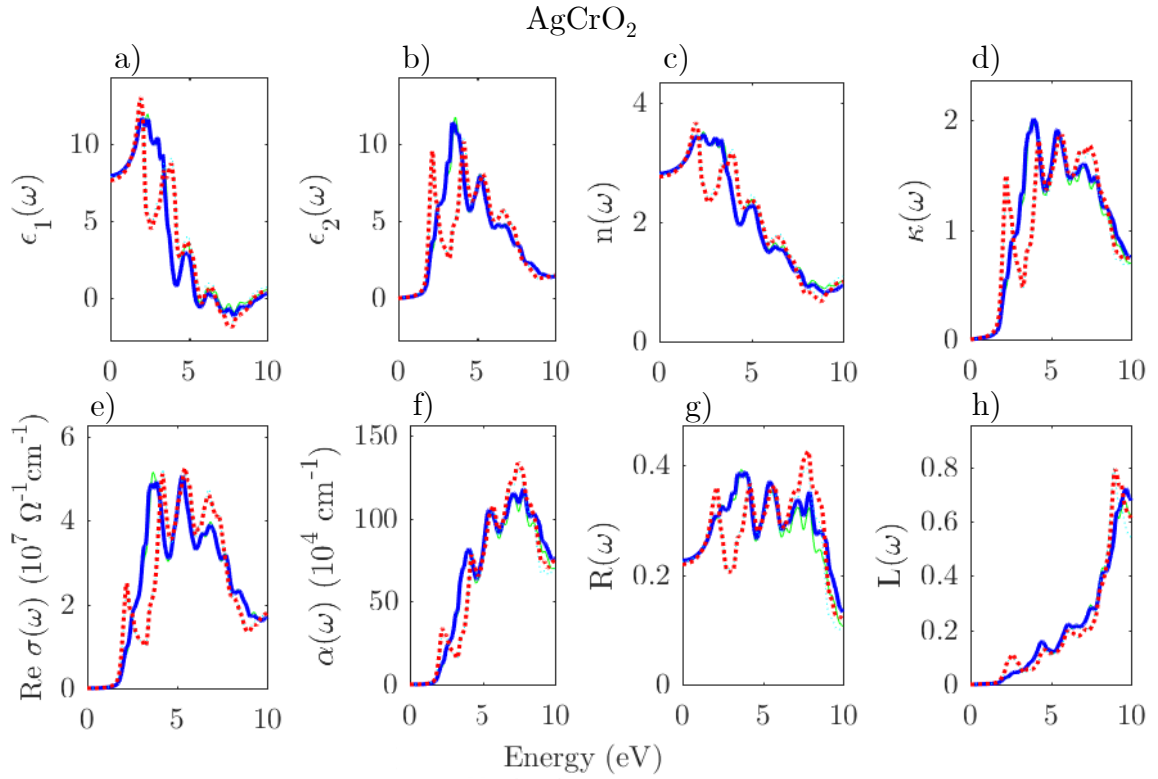


Figure 3.18: Frequency dependence of the a) real component of the complex dielectric function, b) imaginary component of the complex dielectric function, c) refractive index, d) extinction coefficient, e) optical conductivity, f) absorption coefficient, g) reflectivity, and e) loss function of ACO. The in-plane components of the supercell are drawn as a thick blue line and the perpendicular component is drawn by a thick red dashed line. The primitive cell results are plotted in the same panels for comparison, with the in-plane components drawn as a thin green line and a thin cyan dashed line for the perpendicular component.

### 3.6. Summary of Results

All polymorphs of XAO are optimized in the PBE method, and their normalized total energies indicate that 2H XAO may be just as – if not more – stable than 3R XAO in the ground state, and since it is the lesser investigated polymorph, it is chosen to be the focus of the remainder of this work. The simple AFM configuration is the most appropriate choice for XCO in the PC model. PBE+U is shown to most suitably replicate the experimental band gaps and structural properties. The electronic band structure, hole effective masses, and optical properties are determined in the SC scheme and the PC model in order to have confidence in the calculated results of the defect and doped systems. All properties except the XCO hole effective masses in the [010] and [001] directions are determined to be in good agreement between the PC and SC models. The optical properties for XAO support transparent character due to an onset of the optical transition in the real and imaginary components of the complex dielectric function taking place at about 3 eV. Due to the underestimation of the band gaps in XCO, which are smaller than for XAO, the onset of the optical transition happens at roughly 2 eV, in which case the transparent character of XCO is poorly modeled. The lighter hole effective masses in the  $a - b$  plane (with the exception of CCO in the SC model) along with dominant optical properties in the plane for all materials except AAO (in which case the in-plane and perpendicular components are much more symmetric) and the strong contributions from the  $X-d$  and  $O-2p$  states around the band gap support a model of hole conduction in the  $a - b$  plane perpendicular to the O–X–O dumbbells.

## 4. NATIVE DEFECTS IN XTO: X AND O VACANCIES

### 4.1. Introduction

The first type of crystal defects that are studied in this work are X and O vacancies. Vacancies affect the bond lengths of the atoms adjacent and near the defect site, which not only affects the structural parameters, but also the electronic structure by affecting the charge density distribution both from the new positions of the adjacent ions and the absence of an ion at the defect site as well as by acting as an electron donor or acceptor, altering the number of available electrons available for conduction.

### 4.2. Structural Properties

The new bond lengths, reported in Tab. 4.1 show 1.33 – 2.43% and 2.12 – 3.57% shorter lengths for X-O and T-O bonds, respectively, than those of the pristine XTO crystals in Tab. 3.6 adjacent to an X vacancy, indicating a contraction of the dangling O anions towards the T plane. In the presence of an O vacancy, the T-O bond length increases only marginally (0.02 – 0.57%) for all crystals except ACO, where the change is by 1.83%, and the X-O bond length also increases quite drastically, by 9.10 – 19.60%, which is consistent with the X cation relaxing towards the vacancy site towards the T plane adjacent to the vacancy.

Table 4.1: The X-O and T-O bond lengths,  $d_{X-O}$  and  $d_{T-O}$  respectively, of X- and O- vacant XTO in the PBE+U method. % Diff. refers to the difference between the values reported here and the associated values from the pristine crystals reported in Tab. 3.6.

	$d_{X-O}$ (Å)	% Diff.	$d_{T-O}$ (Å)	% Diff.
CuAlO <sub>2</sub> :V <sub>Cu</sub>	1.8556	1.33	1.8602	3.57
AgAlO <sub>2</sub> :V <sub>Ag</sub>	2.0866	1.66	1.9815	2.16
CuCrO <sub>2</sub> :V <sub>Cu</sub>	1.8503	2.43	1.9620	2.12
AgCrO <sub>2</sub> :V <sub>Ag</sub>	2.1219	1.65	1.9518	3.37
CuAlO <sub>2</sub> :V <sub>O</sub>	2.1886	15.15	1.9304	0.13
AgAlO <sub>2</sub> :V <sub>O</sub>	2.5823	19.60	1.9281	0.57
CuCrO <sub>2</sub> :V <sub>O</sub>	2.0766	9.10	2.0411	1.83
AgCrO <sub>2</sub> :V <sub>O</sub>	2.5842	19.48	2.0192	0.02

### 4.3. Electronic Properties

The bond length trends discussed in the previous section manifest as corresponding shifts in the local maxima of the charge densities, shown in Figs. 4.1 and 4.2. A disturbance of the symmetry in the T plane is introduced by the discussed native defects for all crystals except for O vacancies in CAO and vacancies in general for CCO. The band structure for Cu-vacant CAO, shown in Fig. 4.3 along with the DOS, shows the presence of shallow acceptor states above the Fermi energy in the spin up channel, which are strongly Cu-3*d* in nature according to the partial DOS. The electronic structure of Ag-vacant AAO is presented in Fig. 4.4 and contains acceptor states in the spin down channel. Similar to pristine AAO, the character of the DOS is equal parts Ag-4*d* and O-2*p* in the immediate vicinity of the band gap and dominant O-2*p* character at -0.5 eV below the Fermi energy. Very shallow acceptor states in the spin up and down channels are predicted in the Cu-vacant CCO band structure and DOS shown in Fig. 4.5. Here the Cu-3*d*, Cr-3*d*, and O-2*p* states are roughly equal in contribution to the VBM, but the Cr-3*d* states still dominate the lower conduction band energies. The band structure and DOS are

symmetric across spin as shown in Fig. 4.6 for Ag-vacant ACO and indicate shallow acceptor states present in both spin channels. Similar to the pristine crystal, Cr-3d states dominate the area surrounding the band gap, followed by equal contributions from Ag-4d and O-2p states. The shallow acceptor states in X-vacant XTO are likely the result of the vacancy site (missing X<sup>+</sup> ion) acting as an electron acceptor for the adjacent O anions, creating shallow transition energies directly above the Fermi energy.

The O-vacant CAO band structure and DOS presented in Fig. 4.7 exhibit symmetry across spin and a slight decrease in the band gap as compared to pristine CAO. There is an increase in Al-3p states around the band gap, likely from the three Al atoms near the vacancy site which each retain an electron, raising the energy of those associated states. The local maximum with strong Cu-3d character at the VBM is replaced by contributions that taper off towards the VBM that are equal parts Cu-3d and O-2p. Fig. 4.8 shows a drastic decrease in the band gap symmetrically across both spins in O-vacant AAO, likely the result of the corresponding Al-3p states similar to what is discussed for O-vacant CAO. The region surrounding the band gap has equal contributions from Ag-4d and O-2p states. O-vacant CCO contains acceptor states in the spin down channel. The upper valence states near the Fermi energy are now dominated by Cu-3d character down to -0.8 eV below the Fermi energy. The band structure shown in Fig. 4.10 for O-vacant ACO also shows spin down acceptor states. The partial DOS shows that the Cr-3d states remain the dominant contribution to the total DOS around the band gap. For both XCO, there is a decrease in the band gap when compared to the pristine crystal. The shrinking band gap in the case of O vacancies is a result of the X<sup>+</sup> and three T<sup>3+</sup> ions surrounding the vacancy site retaining an extra electron each instead of donating them to an O atom. The retained electrons will be higher in energy than their counterpart empty states and will take less energy to excite into

the conduction bands, thus there are more Al-3*p* and Cr-3*d* states in the upper valence band, pushing the Fermi energy upwards, and more Al-3*p* and Cr-3*d* states near the conduction band minimum, which has moved closer to the Fermi energy.

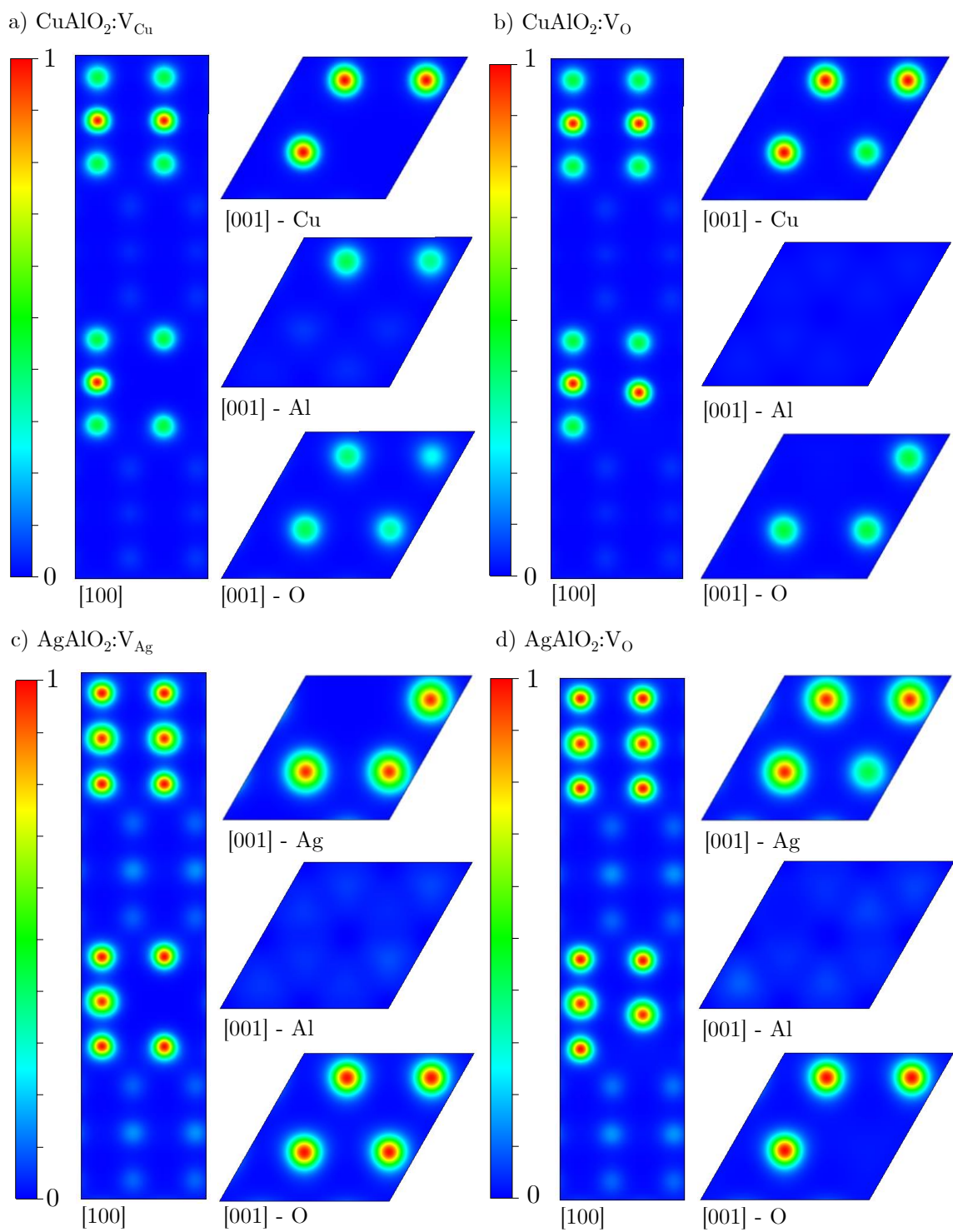


Figure 4.1: Charge density contour plots for a) Cu-vacant CAO, b) O-vacant CAO, c) Ag-vacant AAO, and d) O-vacant AAO  $2 \times 2 \times 2$  supercells using PBE+U. The direction presented with each contour plot indicates a direction perpendicular to the plot and the atomic symbol indicates the ion in the plot.

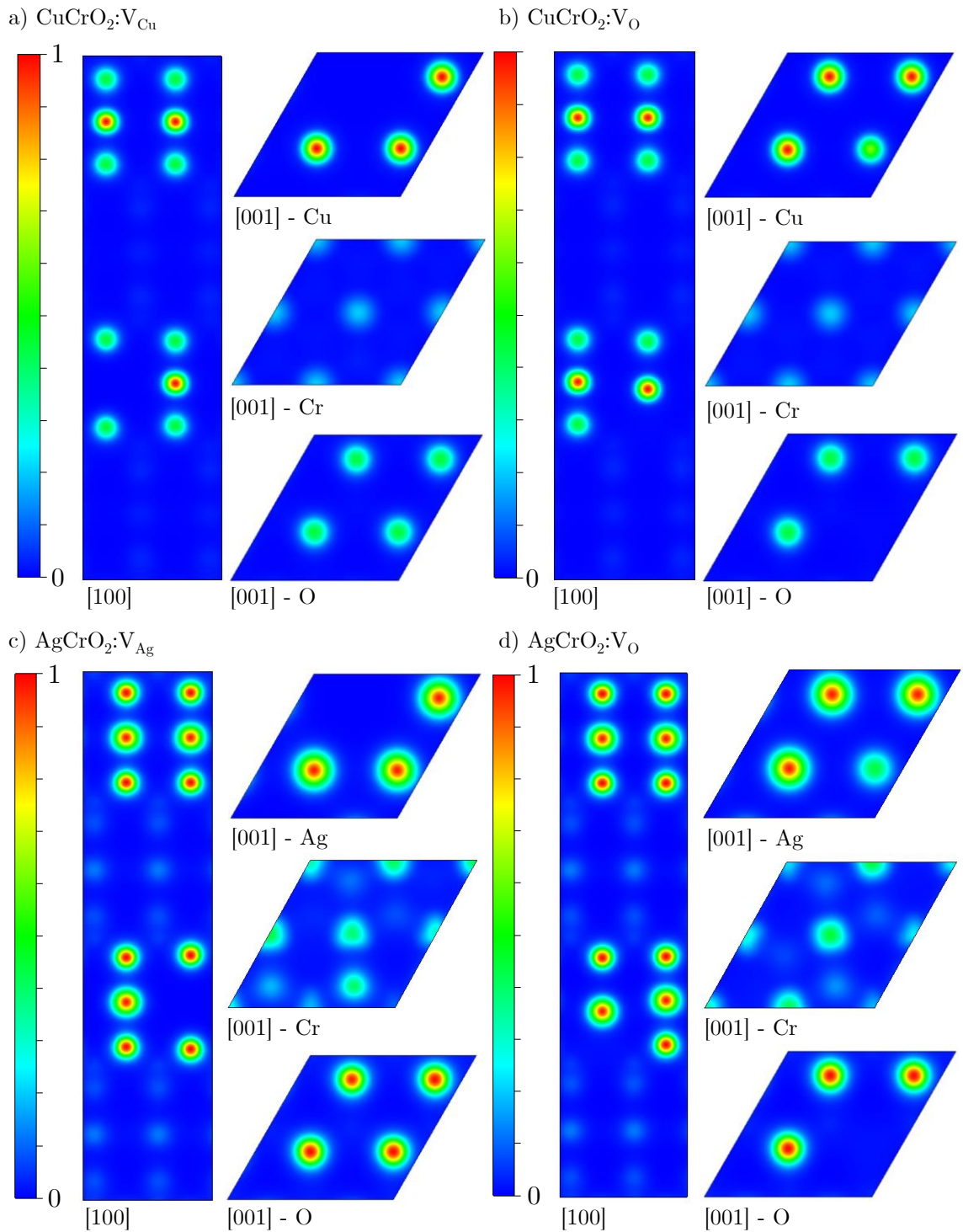


Figure 4.2: Charge density contour plots for a) Cu-vacant CCO, b) O-vacant CCO, c) Ag-vacant ACO, and d) O-vacant ACO  $2 \times 2 \times 2$  supercells using PBE+U. The direction presented with each contour plot indicates a direction perpendicular to the plot and the atomic symbol indicates the ion in the plot.

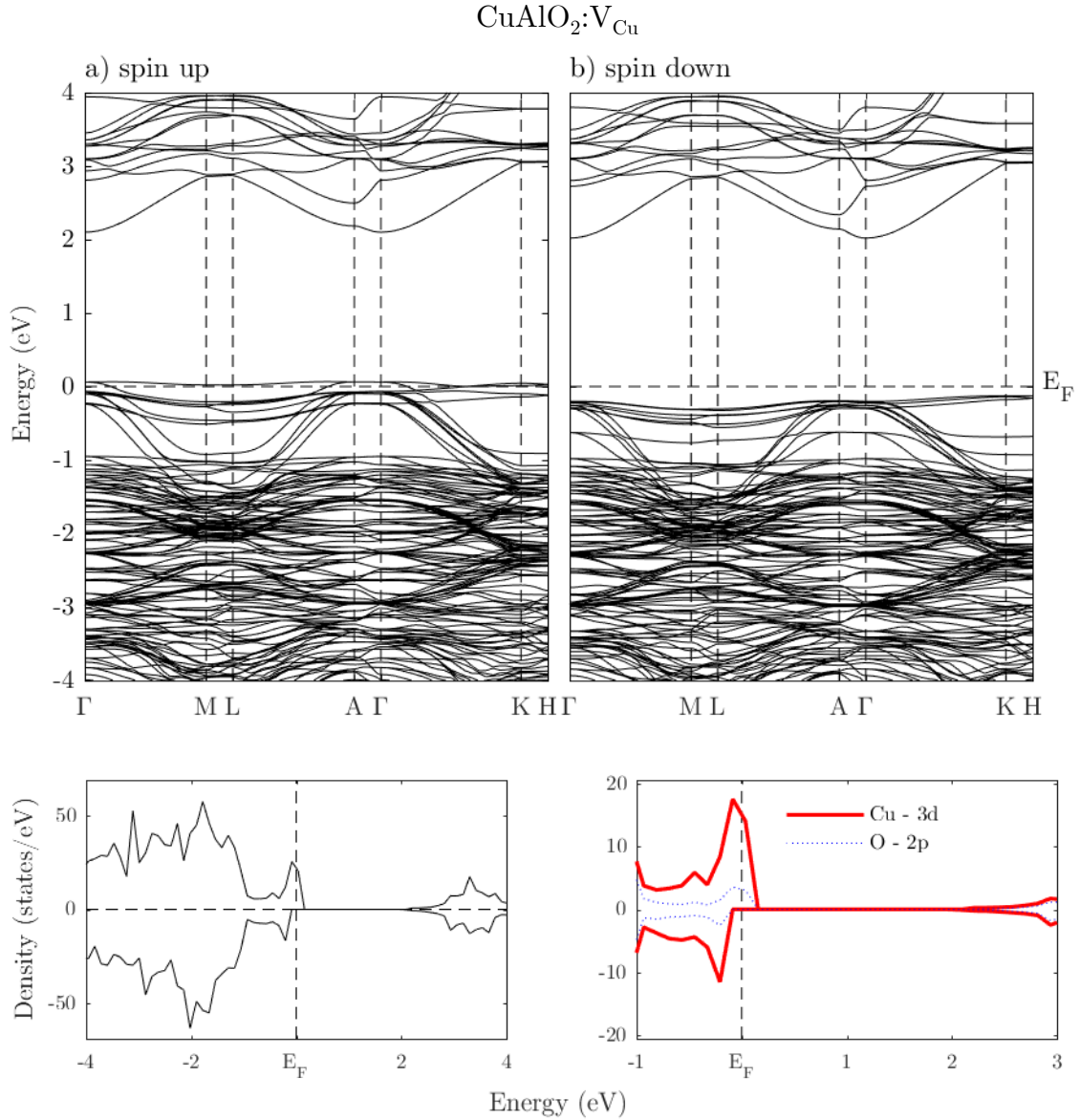


Figure 4.3: The electronic band structure and density of states for Cu-vacant CAO using PBE+U, where the Fermi energy,  $E_F$ , is set to zero and is defined as the maximum energy of a valence electron in the ground state.

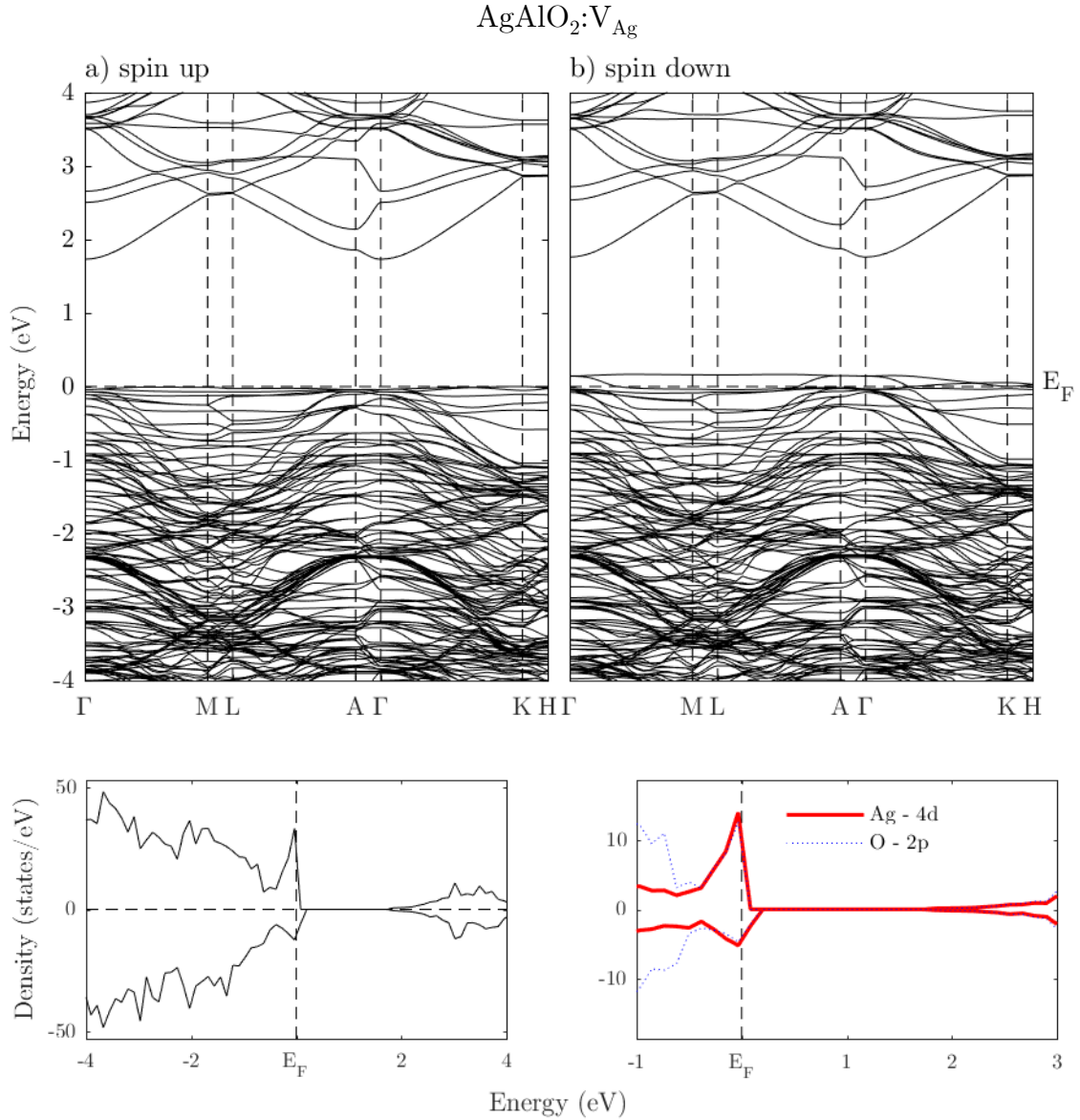


Figure 4.4: The electronic band structure and density of states for Ag-vacant AAO using PBE+U, where the Fermi energy,  $E_F$ , is set to zero and is defined as the maximum energy of a valence electron in the ground state.

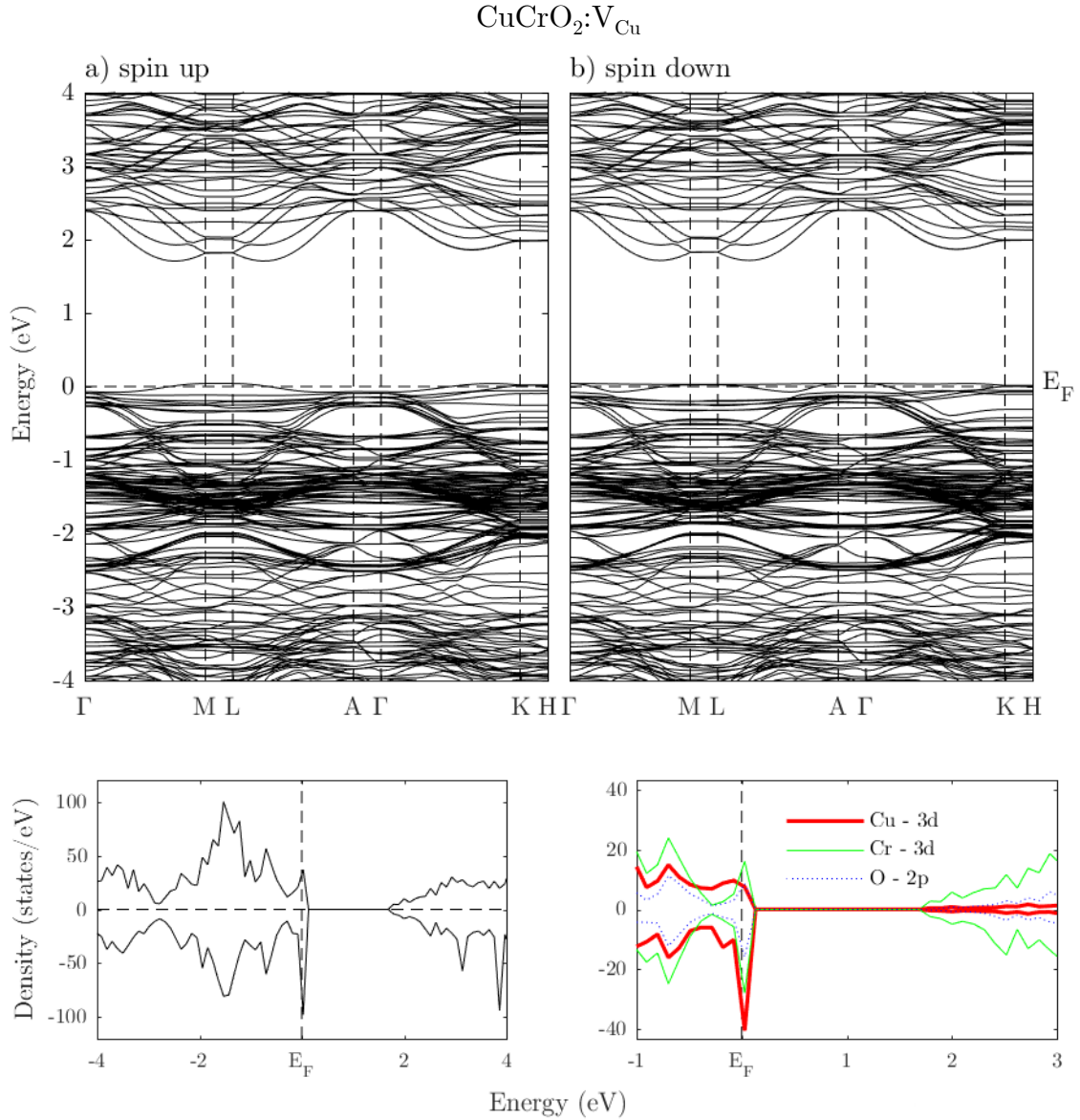


Figure 4.5: The electronic band structure and density of states for Cu-vacant CCO using PBE+U, where the Fermi energy,  $E_F$ , is set to zero and is defined as the maximum energy of a valence electron in the ground state.

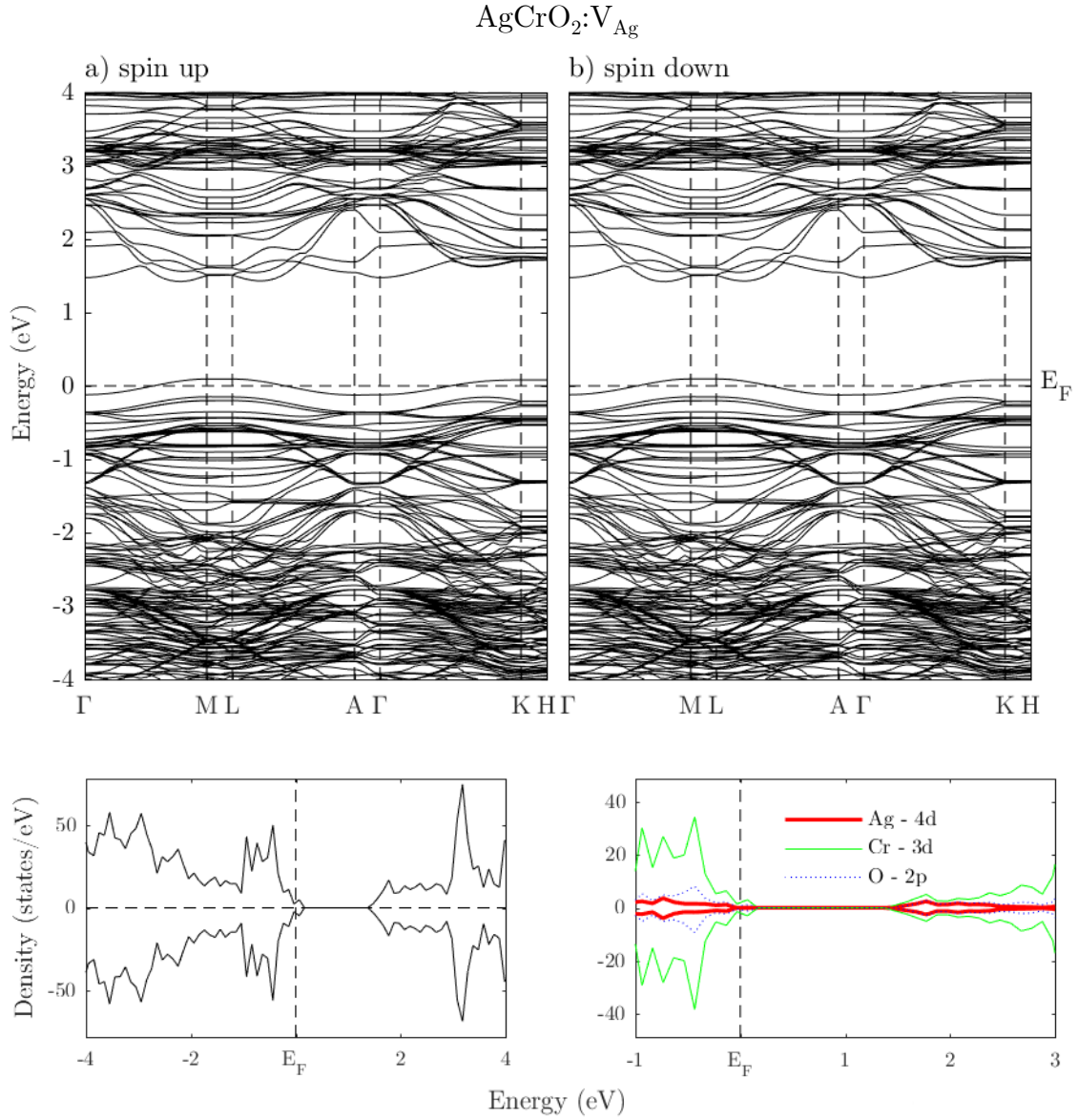


Figure 4.6: The electronic band structure and density of states for Ag-vacant ACO using PBE+U, where the Fermi energy,  $E_F$ , is set to zero and is defined as the maximum energy of a valence electron in the ground state.

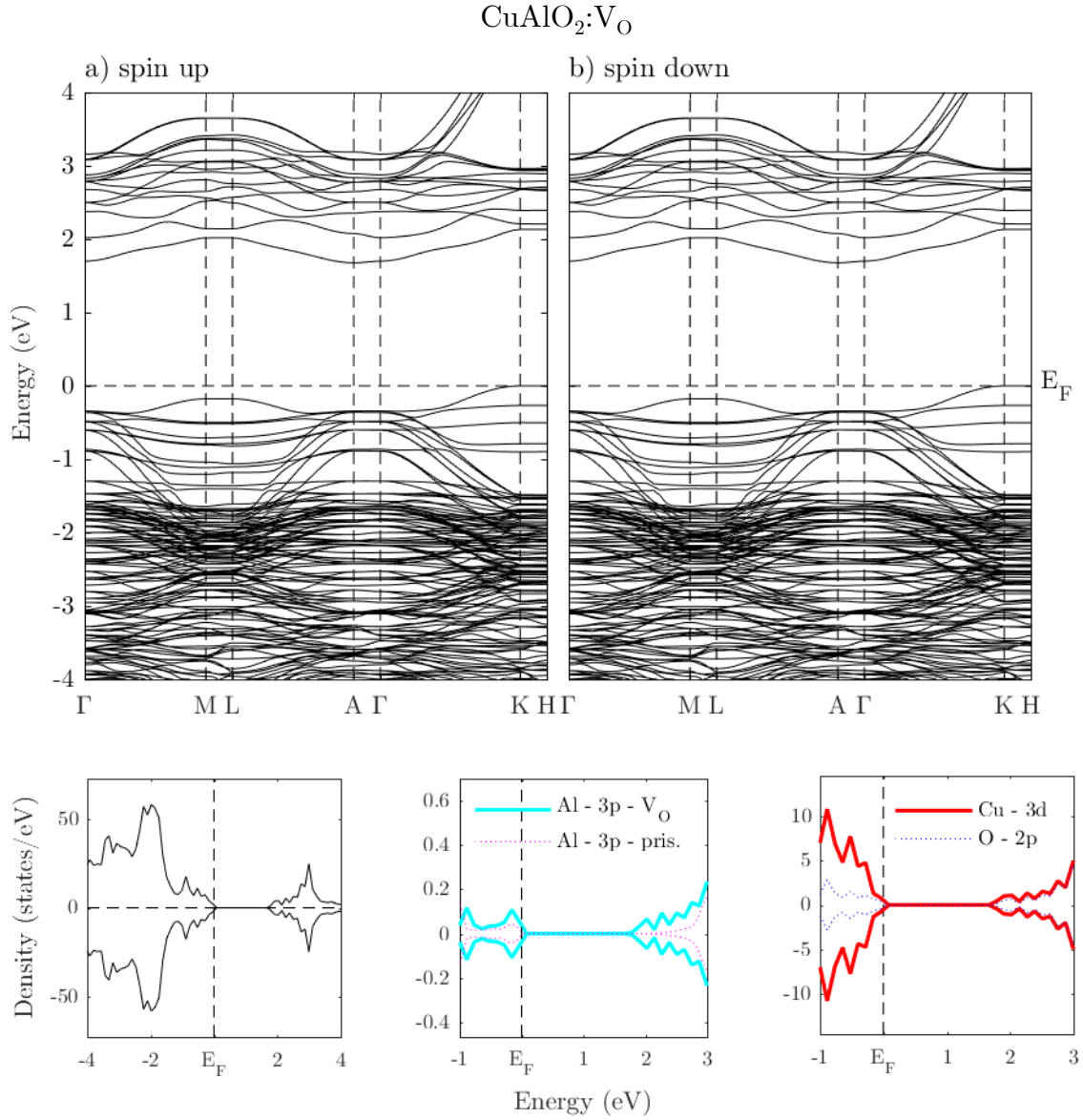


Figure 4.7: The electronic band structure and density of states for O-vacant CAO using PBE+U, where the Fermi energy,  $E_F$ , is set to zero and is defined as the maximum energy of a valence electron in the ground state.

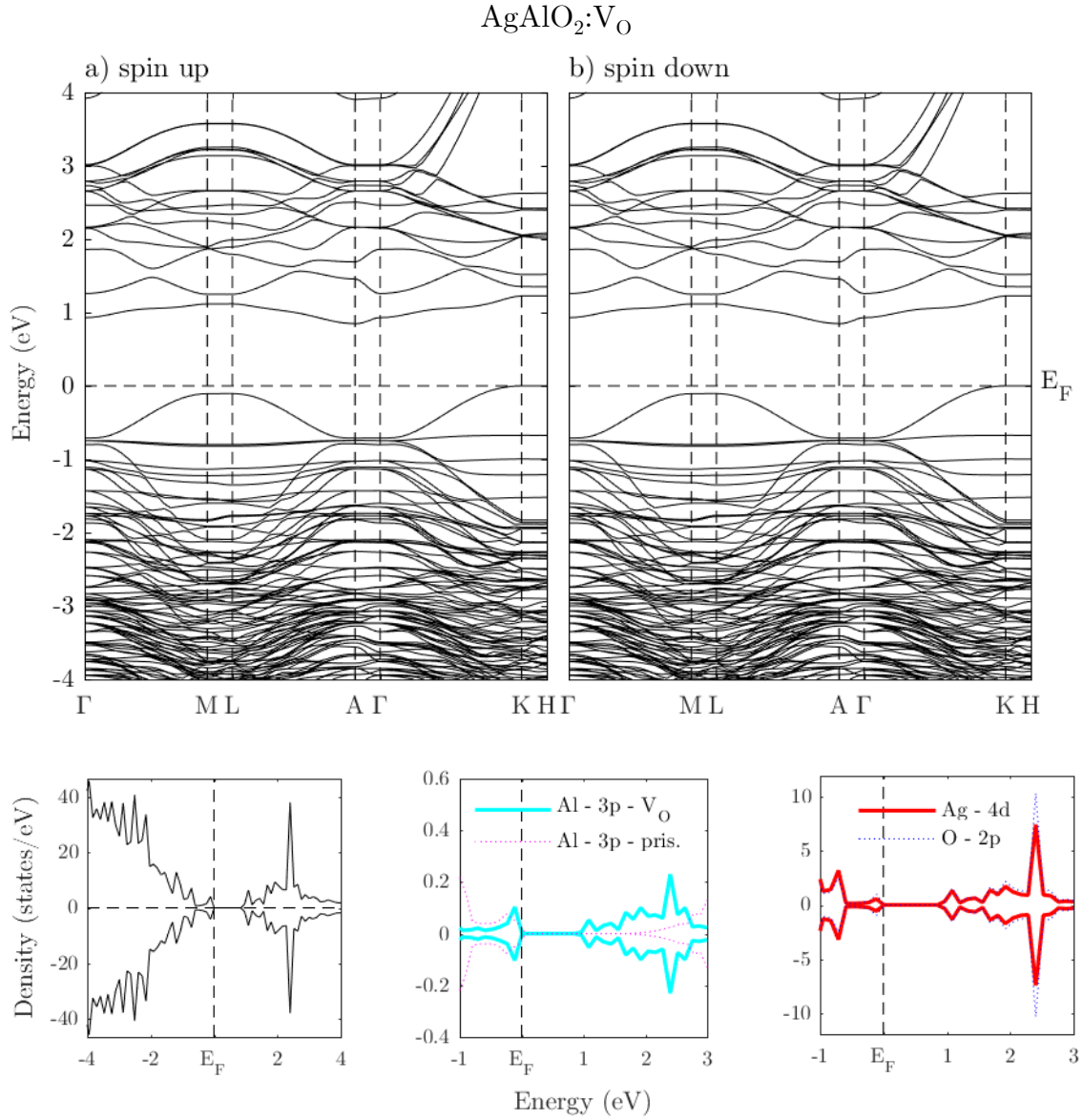


Figure 4.8: The electronic band structure and density of states for O-vacant AAO using PBE+U, where the Fermi energy,  $E_F$ , is set to zero and is defined as the maximum energy of a valence electron in the ground state.

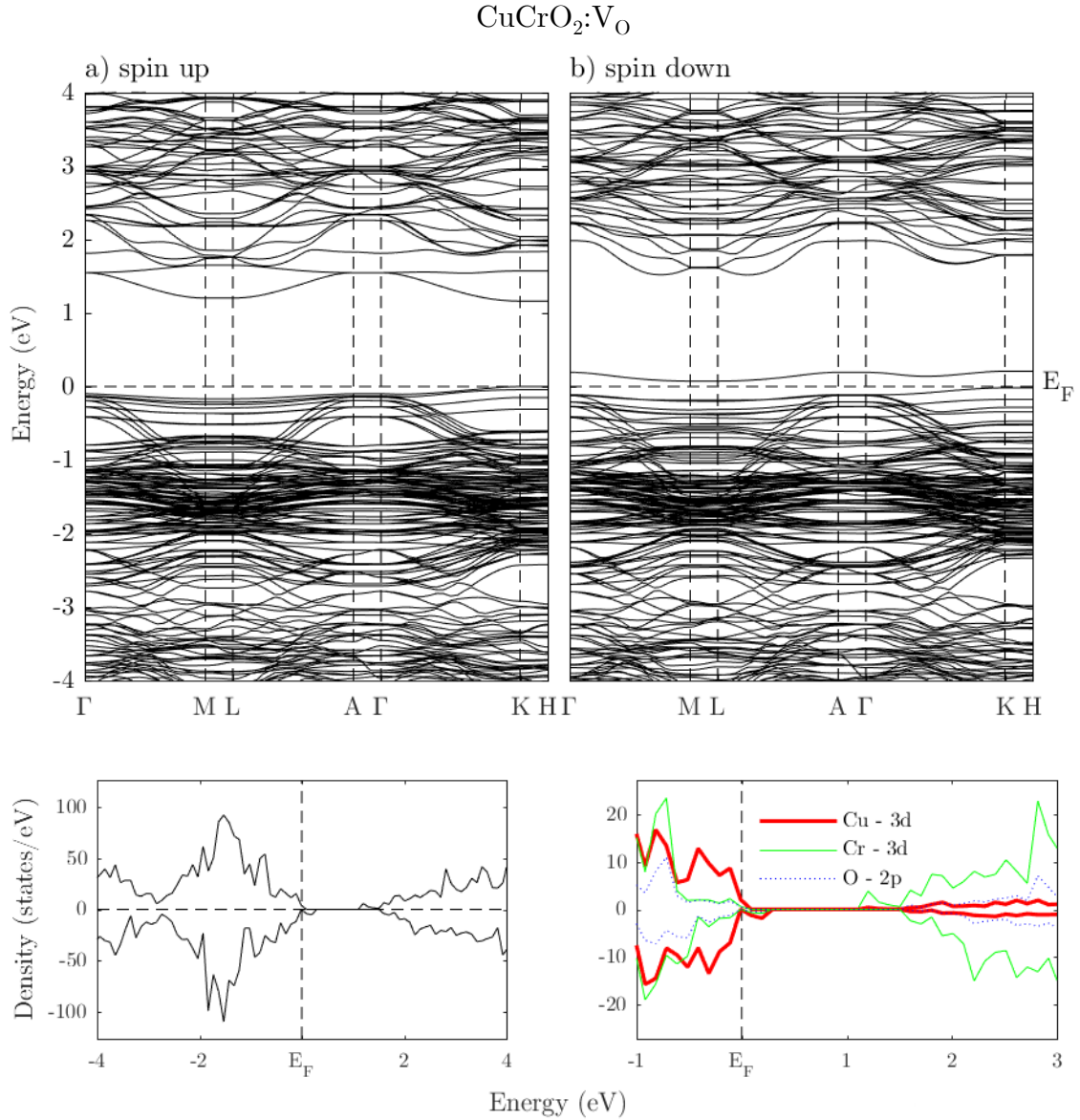


Figure 4.9: The electronic band structure and density of states for O-vacant CCO using PBE+U, where the Fermi energy,  $E_F$ , is set to zero and is defined as the maximum energy of a valence electron in the ground state.

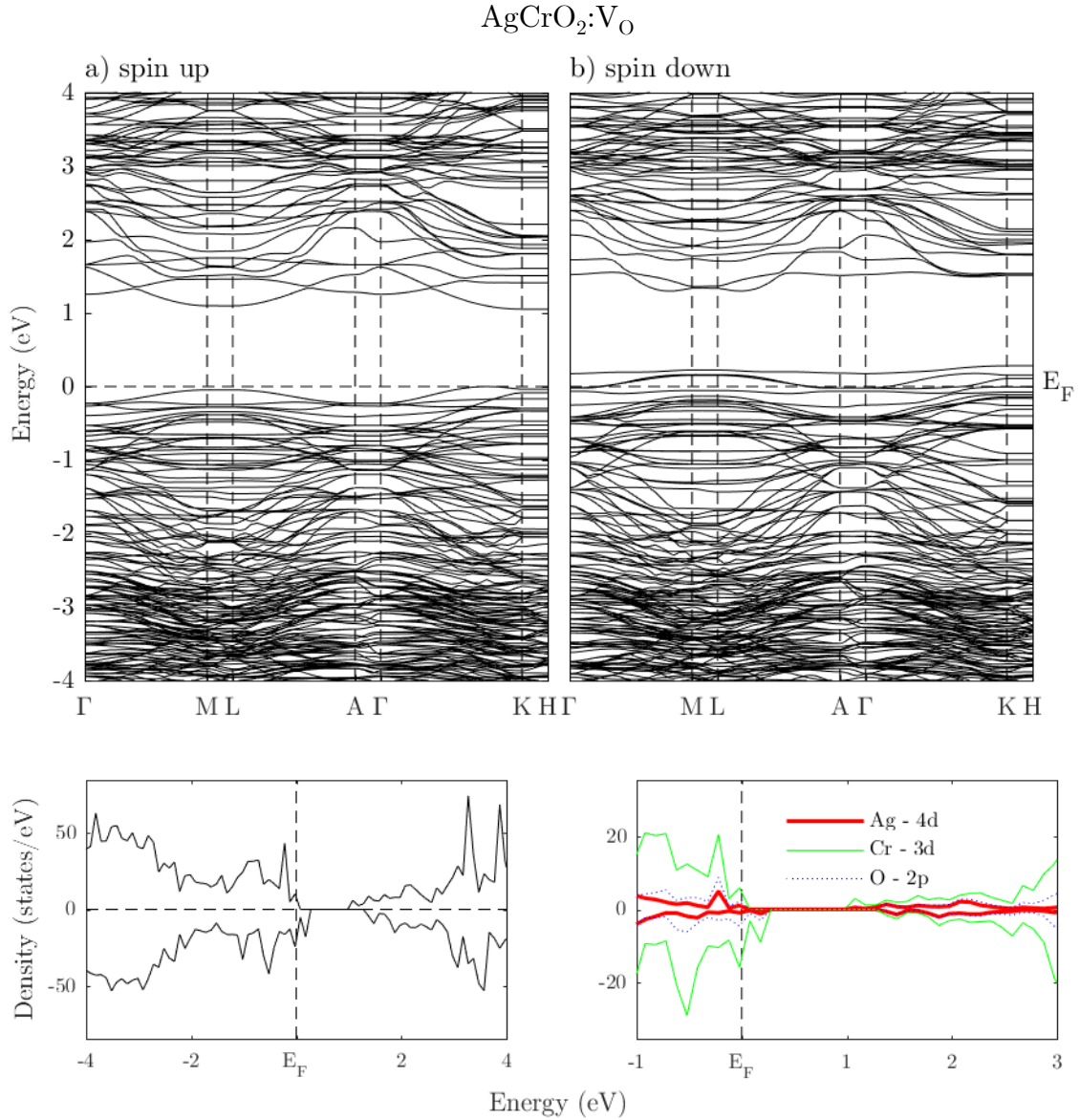


Figure 4.10: The electronic band structure and density of states for O-vacant ACO using PBE+U, where the Fermi energy,  $E_F$ , is set to zero and is defined as the maximum energy of a valence electron in the ground state.

#### 4.4. Hole Effective Masses

The hole effective masses, which are presented in Tab. 4.2 show that X vacancies in XTO increase the hole effective mass across the board compared to the values in Tab. 3.12. Additionally, in Cu-vacant CAO and Ag-vacant ACO, the hole effective masses become the heaviest in the [010] direction, indicating that in those materials conduction perpendicular to the O–X–O dumbbells may no longer be preferential. Although O-vacant XTO retains a similar average value of the hole effective mass of the pristine crystal with the exception of O-vacant CCO, the values in the [100] direction become larger while the [010] values become smaller. From the perspective of hole effective masses, O vacancies may do more to improve conduction than X vacancies.

Table 4.2: The hole effective masses for X- and O-vacant XTO using PBE+U, in units of  $m_e$ , the free electron mass.

	K(L){ $\Gamma$ } $\rightarrow$ $\Gamma$ (A){M} [100]	[010]	K(L){ $\Gamma$ } $\rightarrow$ H(M){A} [001]	avg.
CuAlO <sub>2</sub> :V <sub>Cu</sub> (off- $\Gamma$ )	10.11	10.32	4.89	8.44
AgAlO <sub>2</sub> :V <sub>Ag</sub> (off-K)	6.88	2.23	13.34	7.49
CuCrO <sub>2</sub> :V <sub>Cu</sub> (off-L)	3.48	4.05	18.66	3.14
AgCrO <sub>2</sub> :V <sub>Ag</sub> (off-L)	3.09	7.46	3.58	4.71
CuAlO <sub>2</sub> :V <sub>O</sub> (off-K)	1.82	1.46	1.29	1.52
AgAlO <sub>2</sub> :V <sub>O</sub> (off-K)	1.48	0.84	1.50	1.27
CuCrO <sub>2</sub> :V <sub>O</sub> (off-K)	3.59	2.56	3.10	3.08
AgCrO <sub>2</sub> :V <sub>O</sub> (off-K)	2.42	1.54	0.32	1.43

#### 4.5. Optical Properties

The static dielectric constants and refractive indices for X- and O- vacant XTO, which are shown in Tab. 4.3, are smaller for X-vacant XTO and larger in O-vacant XTO than the static values from the pristine crystal shown in Tab. 3.13.

For the remainder of this work, optical properties presented for the defective and doped systems will be plotted in a solid blue line for the in-plane components and dashed red for the perpendicular components, overlaid onto the

Table 4.3: The static dielectric constants,  $\epsilon_\infty$ , and refractive indices,  $n$ , in the directions a, b, and c, corresponding to the primitive lattice vectors  $\mathbf{b}_1$ ,  $\mathbf{b}_2$ , and  $\mathbf{b}_3$ , of X- and O- vacant XTO modeled in the primitive cell using PBE+U.

	$\epsilon_\infty^a$	$\epsilon_\infty^b$	$\epsilon_\infty^c$	$\epsilon_\infty^{\text{avg}}$	$n_a$	$n_b$	$n_c$	$n_{\text{avg}}$
CuAlO <sub>2</sub> :V <sub>Cu</sub>	4.9681	4.9685	4.2716	4.7361	2.2289	2.2290	2.0668	2.1749
AgAlO <sub>2</sub> :V <sub>Ag</sub>	5.0956	5.0932	5.2570	5.1468	2.2573	2.2568	2.2928	2.2690
CuCrO <sub>2</sub> :V <sub>Cu</sub>	7.2841	7.2867	6.1913	6.9207	2.6989	2.6994	2.4882	2.6288
AgCrO <sub>2</sub> :V <sub>Ag</sub>	7.4677	7.4654	7.1225	7.3519	2.7327	2.7323	2.6688	2.2713
CuAlO <sub>2</sub> :V <sub>O</sub>	5.7020	5.6969	5.0480	5.4823	2.3879	2.3868	2.2468	2.3405
AgAlO <sub>2</sub> :V <sub>O</sub>	6.1675	6.1659	7.4967	6.6100	2.4834	2.4831	2.7380	2.5682
CuCrO <sub>2</sub> :V <sub>O</sub>	8.1215	8.1223	6.8623	7.7020	2.8498	2.8500	2.6196	2.7731
AgCrO <sub>2</sub> :V <sub>O</sub>	8.4270	8.4258	8.3722	8.4083	2.9029	2.9027	2.8935	2.8897

pristine XTO crystal modeled in the SC scheme to facilitate evaluation. The Cu-vacancy in CAO results in slightly less extreme maxima in the in-plane component of the complex dielectric function as compared to pristine CAO. This lends a similar behavior to the remaining optical properties, where the local maxima on the in-plane components are also not as pronounced as in the pristine crystal. The Ag-vacancies in AAO produce the same decrease in the maximum in-plane values of the complex dielectric function as discussed for Cu-vacant CAO and are shown in Fig. 4.12. For the optical properties of Cu-vacant CCO, displayed in Fig. 4.13, both the in-plane and perpendicular components are lower than the pristine crystal across the spectrum. The in-plane component of the complex dielectric function if Ag-vacant ACO is less than the pristine ACO crystal out to 7 eV, and then takes on larger values. The perpendicular component of the complex dielectric function appears largely unaffected.

The optical properties of O-vacant CAO are similar to the pristine crystal with the exception of a new local maximum for both components at approximately 2.0 eV, which is shown in Fig. 4.15. As shown in Fig. 4.16, a similar new local maxima appears in both components of the complex dielectric function for O-vacant AAO, but at about 1.0 eV. A new but only marginally pronounced oscillation in the

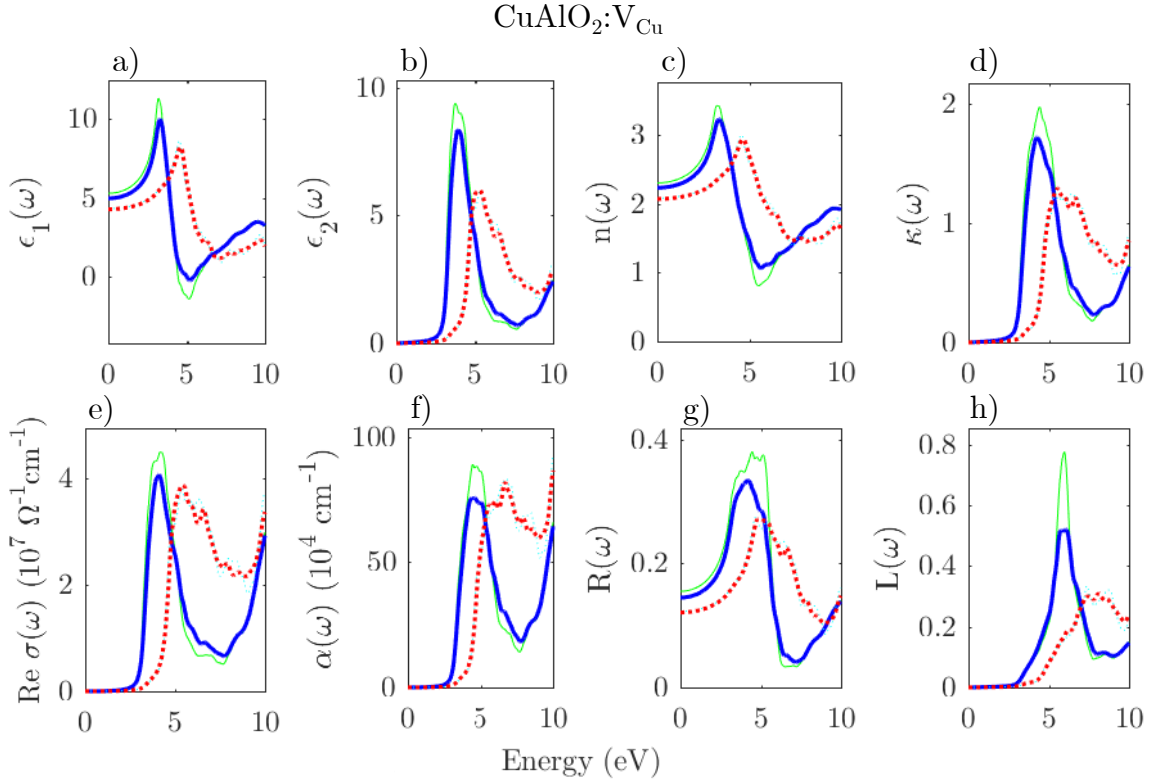


Figure 4.11: Frequency dependence of the a) real component of the complex dielectric function, b) imaginary component of the complex dielectric function, c) refractive index, d) extinction coefficient, e) optical conductivity, f) absorption coefficient, g) reflectivity, and e) loss function of Cu-vacant CAO. The in-plane components are drawn as a thick blue line and the perpendicular component is drawn by a thick red dashed line. The pristine supercell results are plotted in the same panels for comparison, with the in-plane components drawn as a thin green line and a thin cyan dashed line for the perpendicular component.

in-plane component of the complex dielectric function appears in O-vacant CCO, shown in Fig. 4.17, at about 2.0 eV. For O-vacant ACO, which is shown in Fig. 4.18, the new minor oscillation at 1.5 eV is in the perpendicular component of the complex dielectric function.

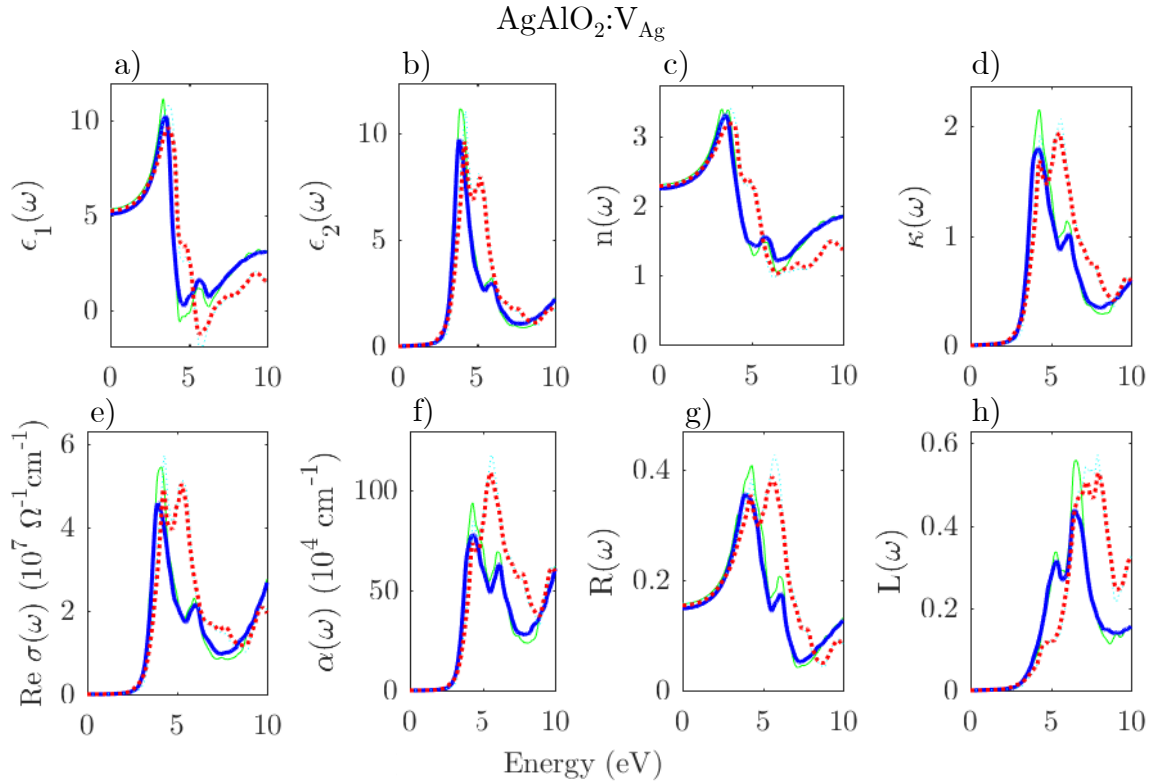


Figure 4.12: Frequency dependence of the a) real component of the complex dielectric function, b) imaginary component of the complex dielectric function, c) refractive index, d) extinction coefficient, e) optical conductivity, f) absorption coefficient, g) reflectivity, and e) loss function of Ag-vacant AAO. The in-plane components are drawn as a thick blue line and the perpendicular component is drawn by a thick red dashed line. The pristine supercell results are plotted in the same panels for comparison, with the in-plane components drawn as a thin green line and a thin cyan dashed line for the perpendicular component.

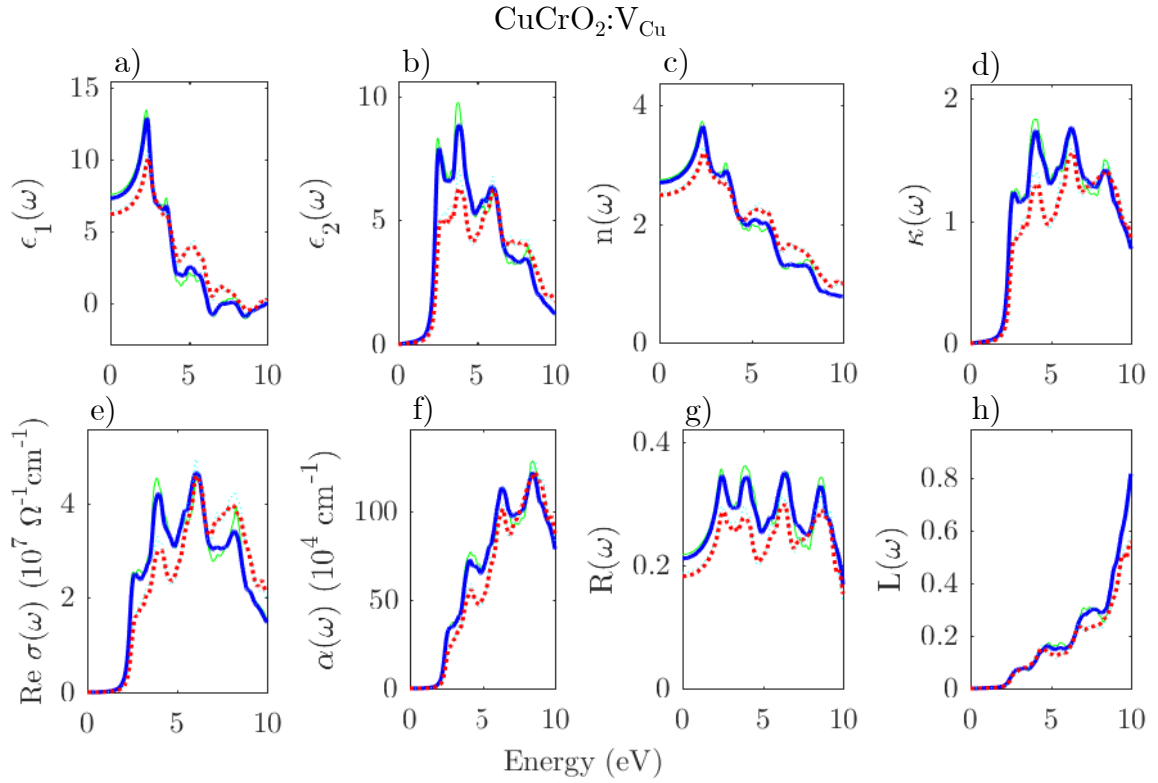


Figure 4.13: Frequency dependence of the a) real component of the complex dielectric function, b) imaginary component of the complex dielectric function, c) refractive index, d) extinction coefficient, e) optical conductivity, f) absorption coefficient, g) reflectivity, and e) loss function of Cu-vacant CCO. The in-plane components are drawn as a thick blue line and the perpendicular component is drawn by a thick red dashed line. The pristine supercell results are plotted in the same panels for comparison, with the in-plane components drawn as a thin green line and a thin cyan dashed line for the perpendicular component.

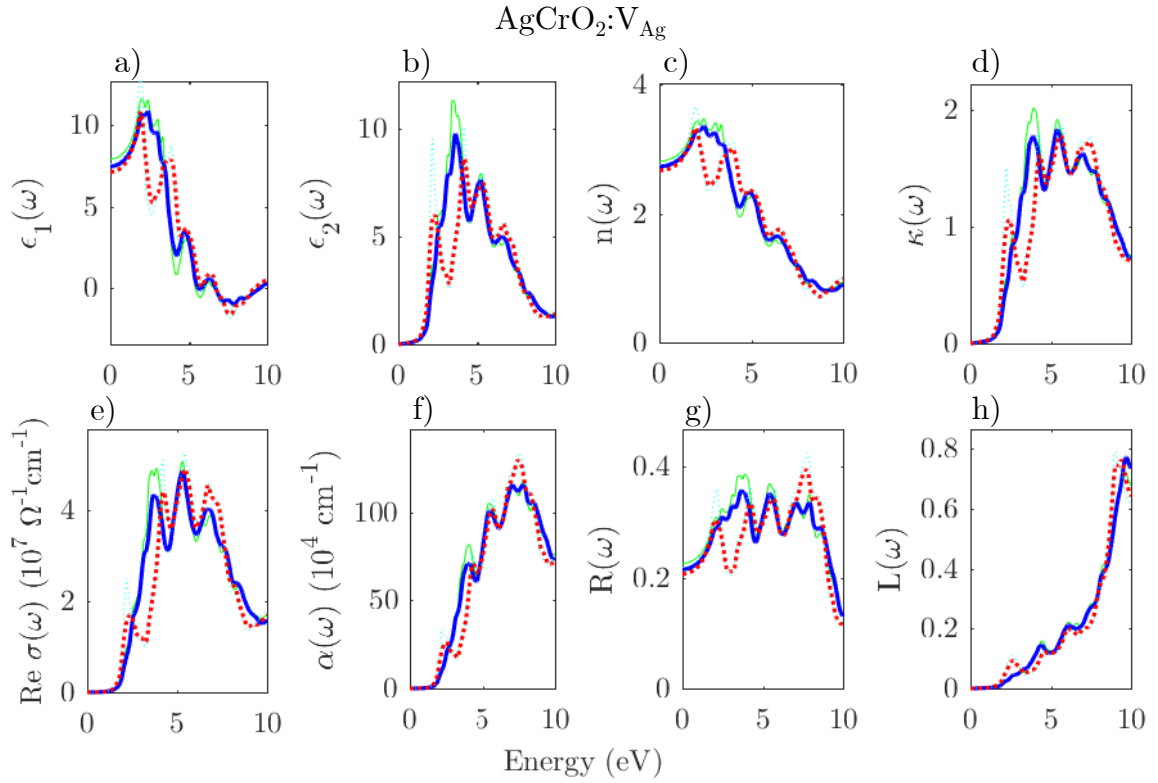


Figure 4.14: Frequency dependence of the a) real component of the complex dielectric function, b) imaginary component of the complex dielectric function, c) refractive index, d) extinction coefficient, e) optical conductivity, f) absorption coefficient, g) reflectivity, and e) loss function of Ag-vacant ACO. The in-plane components are drawn as a thick blue line and the perpendicular component is drawn by a thick red dashed line. The pristine supercell results are plotted in the same panels for comparison, with the in-plane components drawn as a thin green line and a thin cyan dashed line for the perpendicular component.

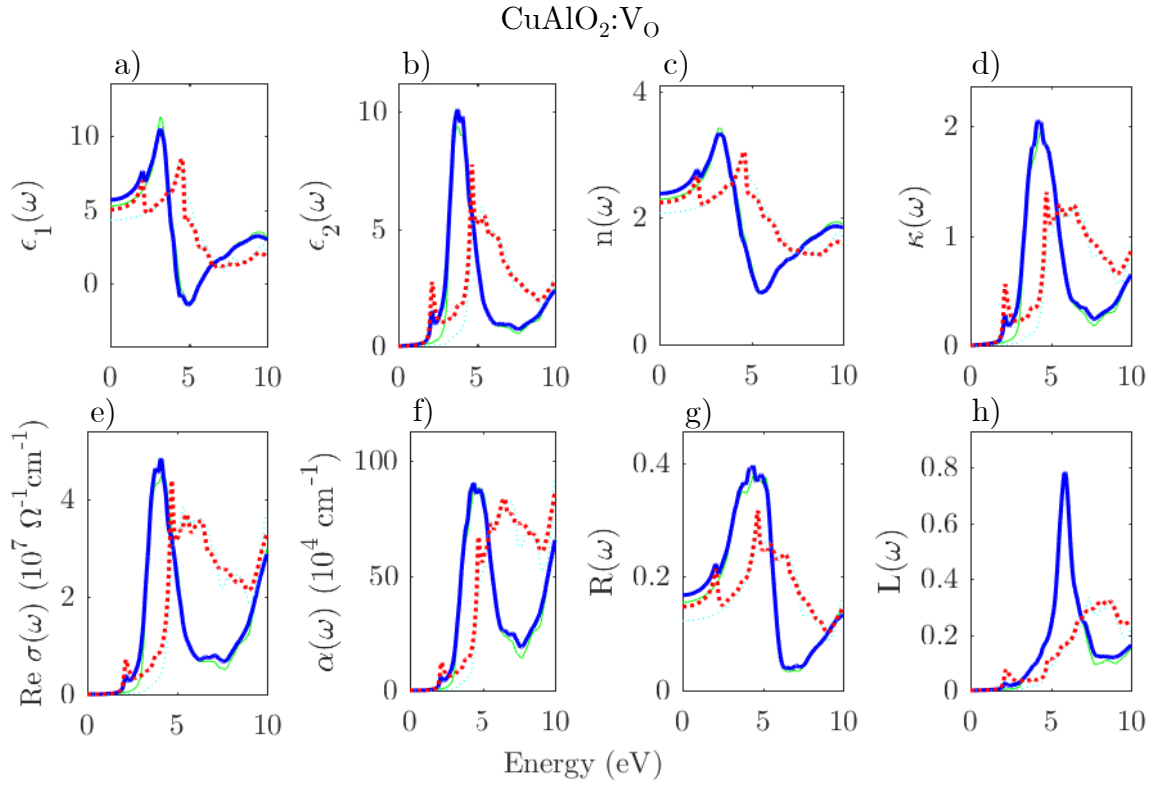


Figure 4.15: Frequency dependence of the a) real component of the complex dielectric function, b) imaginary component of the complex dielectric function, c) refractive index, d) extinction coefficient, e) optical conductivity, f) absorption coefficient, g) reflectivity, and h) loss function of O-vacant CAO. The in-plane components are drawn as a thick blue line and the perpendicular component is drawn by a thick red dashed line. The pristine supercell results are plotted in the same panels for comparison, with the in-plane components drawn as a thin green line and a thin cyan dashed line for the perpendicular component.

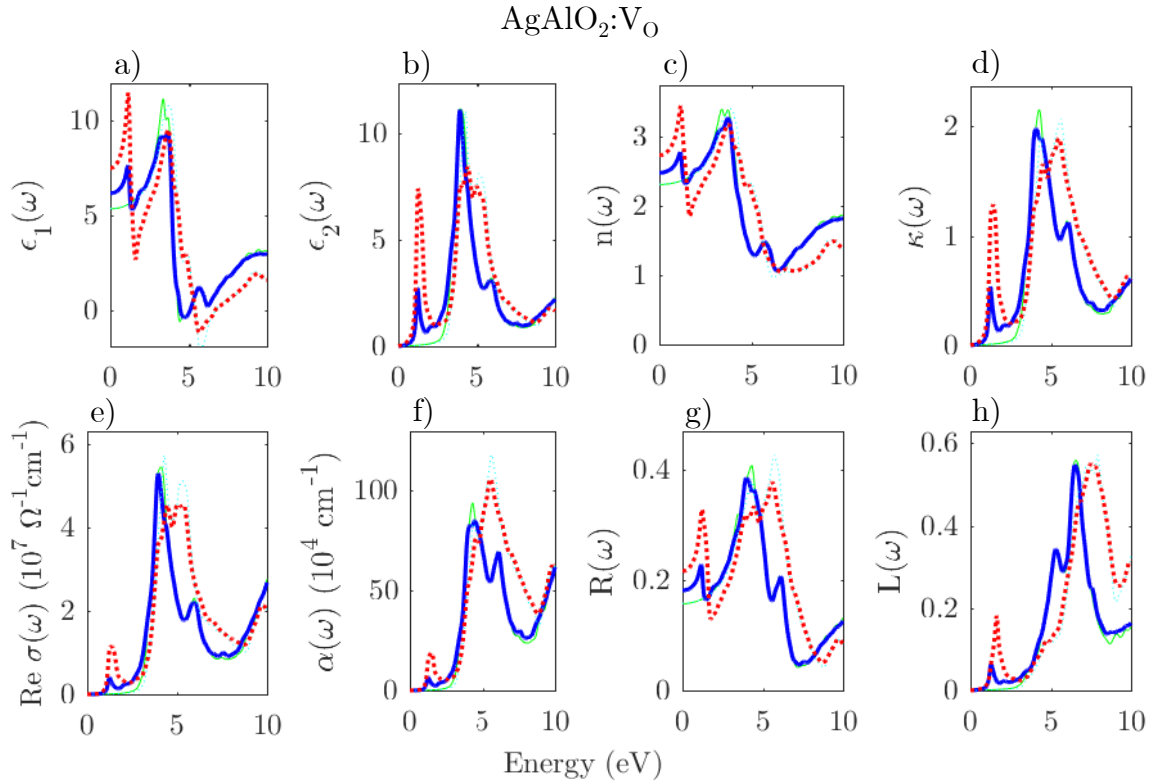


Figure 4.16: Frequency dependence of the a) real component of the complex dielectric function, b) imaginary component of the complex dielectric function, c) refractive index, d) extinction coefficient, e) optical conductivity, f) absorption coefficient, g) reflectivity, and h) loss function of O-vacant AAO. The in-plane components are drawn as a thick blue line and the perpendicular component is drawn by a thick red dashed line. The pristine supercell results are plotted in the same panels for comparison, with the in-plane components drawn as a thin green line and a thin cyan dashed line for the perpendicular component.

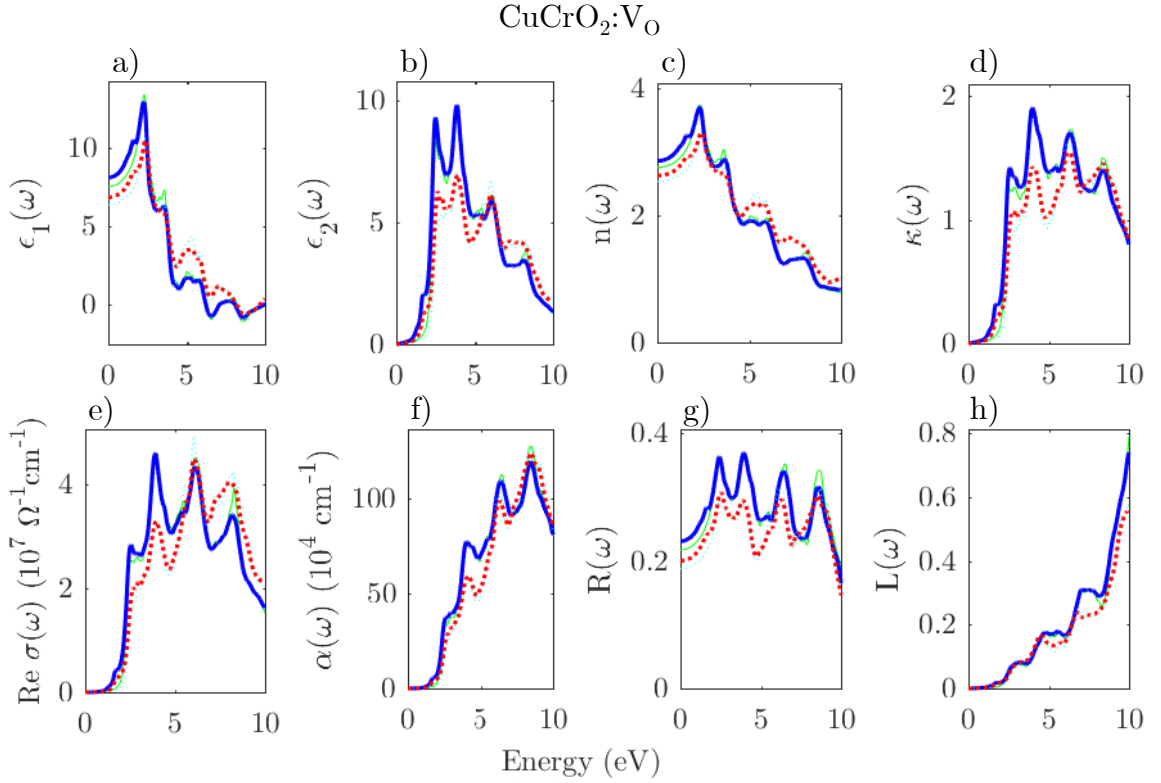


Figure 4.17: Frequency dependence of the a) real component of the complex dielectric function, b) imaginary component of the complex dielectric function, c) refractive index, d) extinction coefficient, e) optical conductivity, f) absorption coefficient, g) reflectivity, and h) loss function of O-vacant CCO. The in-plane components are drawn as a thick blue line and the perpendicular component is drawn by a thick red dashed line. The pristine supercell results are plotted in the same panels for comparison, with the in-plane components drawn as a thin green line and a thin cyan dashed line for the perpendicular component.

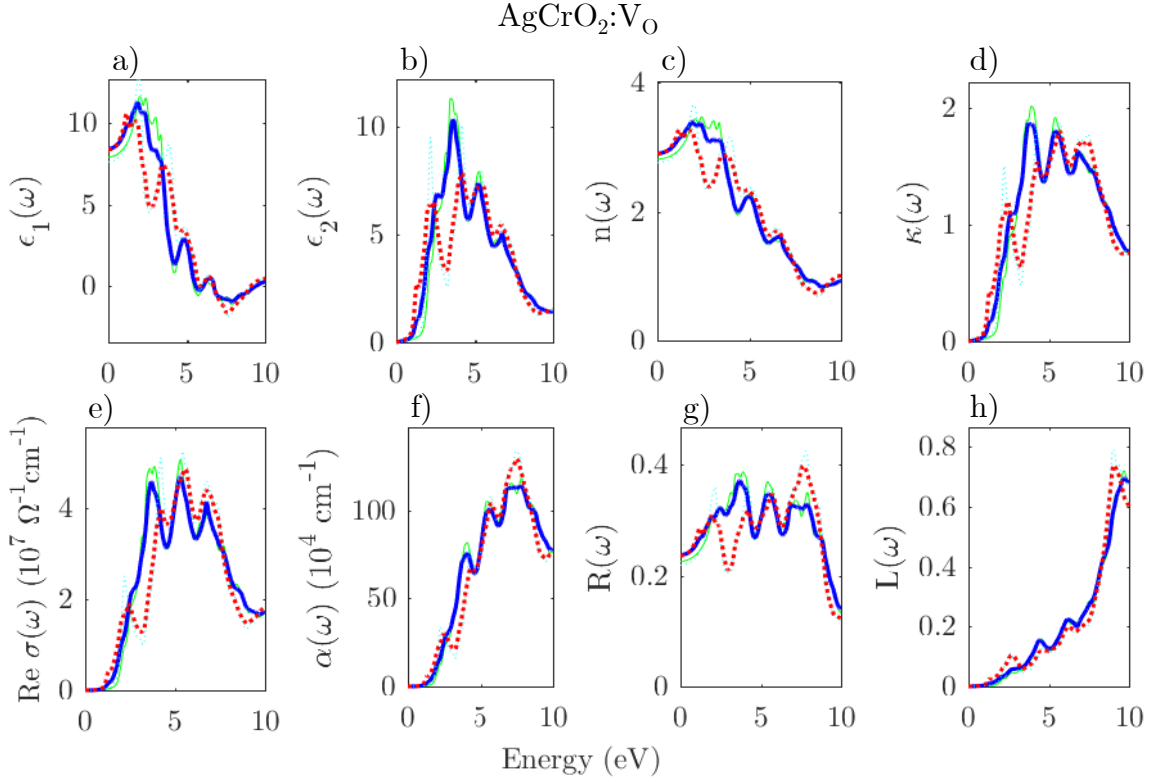


Figure 4.18: Frequency dependence of the a) real component of the complex dielectric function, b) imaginary component of the complex dielectric function, c) refractive index, d) extinction coefficient, e) optical conductivity, f) absorption coefficient, g) reflectivity, and h) loss function of O-vacant ACO. The in-plane components are drawn as a thick blue line and the perpendicular component is drawn by a thick red dashed line. The pristine supercell results are plotted in the same panels for comparison, with the in-plane components drawn as a thin green line and a thin cyan dashed line for the perpendicular component.

## 4.6. Summary of Results

The X and O vacancies produce acceptor states in XCO, and X vacancies also produce acceptor states in XAO by redistributing the charge density due to changes in the bond lengths of the ions around the vacancy site, and by acting as an electron acceptor. The hole effective masses for X-vacant XTO are larger than in the pristine crystal, while the hole effective masses for O-vacant XTO are not drastically changed overall, although the particular masses in the [100] and [010] have opposite trends to those in the pristine crystal. Even though the values of the hole effective masses suggest that oxygen vacancies may be beneficial to conductivity, the changes introduced to the electronic structure and optical properties are not favorable for transparent character. The oxygen vacancies in AAO greatly reduce the bandgap to less than 2.5 eV, and to a lesser degree decrease the band gap in CAO and XCO as well, which threatens the transparency of the material. The new Al-3*p* states on either side of the band gap in XAO have a difference in energy of about 1.0(2.0) eV, which corresponds to new local maxima in the visible portion of the spectrum for the optical properties in O-vacant CAO(AAO) and may indicate that the transitions of those states are direct (no change in wavenumber). Since Cr-3*d* states are already quite dominant in the pristine crystal, there is a small shift ( $< 0.5$  eV) in the onset of the optical transition towards 0 eV, but otherwise the overall character of the optical properties is not as drastically affected as in XAO. Overall then, the promotion of conduction holes and general preservation of optical properties around the visible spectrum imply that promoting X vacancies during crystal growth may improve conductivity and preserve transparent character, even though the increase in hole effective masses may act as a limiting factor. Due to O vacancies affecting transparency in XTO, crystal growth in O-rich environments may be crucial to preserve transparency.

## 5. MAGNESIUM IMPURITIES IN XTO

### 5.1. Introduction

The final defect to be studied in this work is 6.25% Mg doping replacing T. Similar to vacancies, the Mg dopant affects the bond lengths of the atoms around it and also donates an electron to the charge density. Both of these factors affect changes to the electronic structure and optical properties. Mg replaces Al in XAO and acts as a hole donor due to having one less valence electron available for conduction, ionizing to  $\text{Mg}^{2+}$ . Within XCO, Mg replaces Cr, again acting as a hole donor. However, in the case of XCO, the valence configuration of  $\text{Mg}^{2+}$ ,  $3s^0$ , also has three fewer electrons than the  $\text{Cr}^{3+}$  ion with a valence configuration of  $3d^34s^0$ . There is an upper saturation limit on how much Mg can be added to the XTO crystal before the semiconductor nature gives way to strong metallicity or even becomes fundamentally altered by taking on the character of an alloy.

### 5.2. Structural Properties

All of the Mg-O bond lengths, displayed with the other new bond lengths in Tab. 5.1, are longer than the T-O bond lengths in the pristine crystals by 3.41 – 4.58%. Additionally, the new T-O bond lengths surrounding the dopant are slightly shorter by 0.04 – 1.79%, and the new Cu(Ag)–O bond lengths are shorter(longer) for CTO(AAO) by 2.68 – 3.13%(0.22%), and also shorter for ACO by 0.44%.

Table 5.1: The X-O and T-O bond lengths,  $d_{\text{X-O}}$  and  $d_{\text{T-O}}$  respectively, of Mg-doped XTO in the PBE+U method. % Diff. refers to the difference between the values reported here and the associated values from the pristine crystals reported in Tab. 3.6.

	$d_{\text{X-O}}$ (Å)	% Diff.	$d_{\text{T-O}}$ (Å)	% Diff.	$d_{\text{Mg-O}}$ (Å)	% Diff.
$\text{CuAl}_{0.94}\text{Mg}_{0.06}\text{O}_2$	1.8308	2.68	1.9074	1.06	2.0140	4.37
$\text{AgAl}_{0.94}\text{Mg}_{0.06}\text{O}_2$	2.1261	0.22	1.9383	0.04	2.0300	4.58
$\text{CuCr}_{0.94}\text{Mg}_{0.06}\text{O}_2$	1.8375	3.13	2.0022	0.09	2.0770	3.58
$\text{AgCr}_{0.94}\text{Mg}_{0.06}\text{O}_2$	2.1161	0.44	1.9829	1.79	2.0888	3.41

### 5.3. Electronic Properties

The replacement of a T atom with Mg does not exhibit much more than a marginal change to the charge density in the T plane. Charge density contour plots for Mg-doped XTO are depicted in Fig. 5.1.

The band structure and DOS presented in Fig. 5.2 for Mg-doped CAO show acceptor states in the spin up channel, but otherwise the major contribution to the DOS remains Cu-3*d* states in the upper valence bands and equal parts Cu-3*d* and O-2*p* states in the lower conduction bands. Shown in Fig. 5.3 are the band structure and DOS for Mg-doped AAO. The acceptor states reside in the spin down channel, and the dominant contribution to the DOS in the upper valence bands are Ag-4*d* and O-2*p* states, with the lower conduction states remaining equal parts Ag-4*d* and O-2*p* states. Similar to O-vacant CCO, Mg-doped CCO, shown in Figure 5.4, has acceptor states in the spin up channel and strong Cu-3*d* contribution in the upper valence bands with Cr-3*d* and O-2*p* states in roughly equal measure. In the lower valence bands the Cr-3*d* states dominate over Ag-4*d* and O-2*p* states which are present in equal amounts. Lastly, the electronic structure of Mg-doped ACO are presented in Fig. 5.5. The acceptor states in the spin down channel are barely distinguishable in the partial DOS, and for that reason a small inset plot is included in the plot of the partial DOS that emphasizes this acceptor states. Below the Fermi energy the DOS is highly Cr-3*d* in character down to -1.0 eV, with slightly more O-2*p* states than Ag-4*d* moving towards the Fermi energy. In the lower conduction bands, the Cr-3*d* states are the greatest contribution, followed closely by Ag-4*d* and O-2*p*.

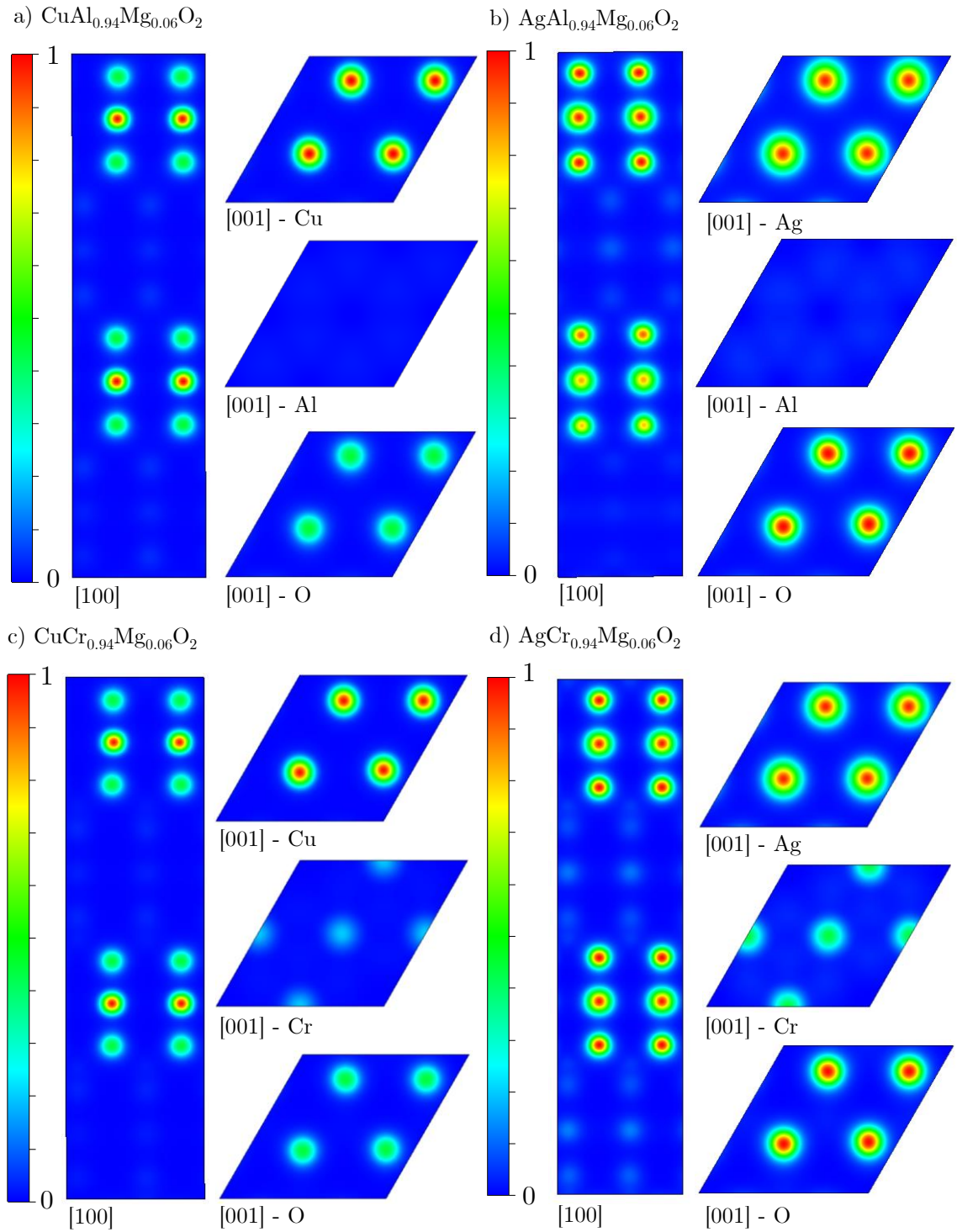


Figure 5.1: Charge density contour plots for Mg-doped a) CAO, b) AAO, c) CCO, and d) ACO  $2 \times 2 \times 2$  supercells using PBE+U. The direction presented with each contour plot indicates a direction perpendicular to the plot and the atomic symbol indicates the ion in the plot.

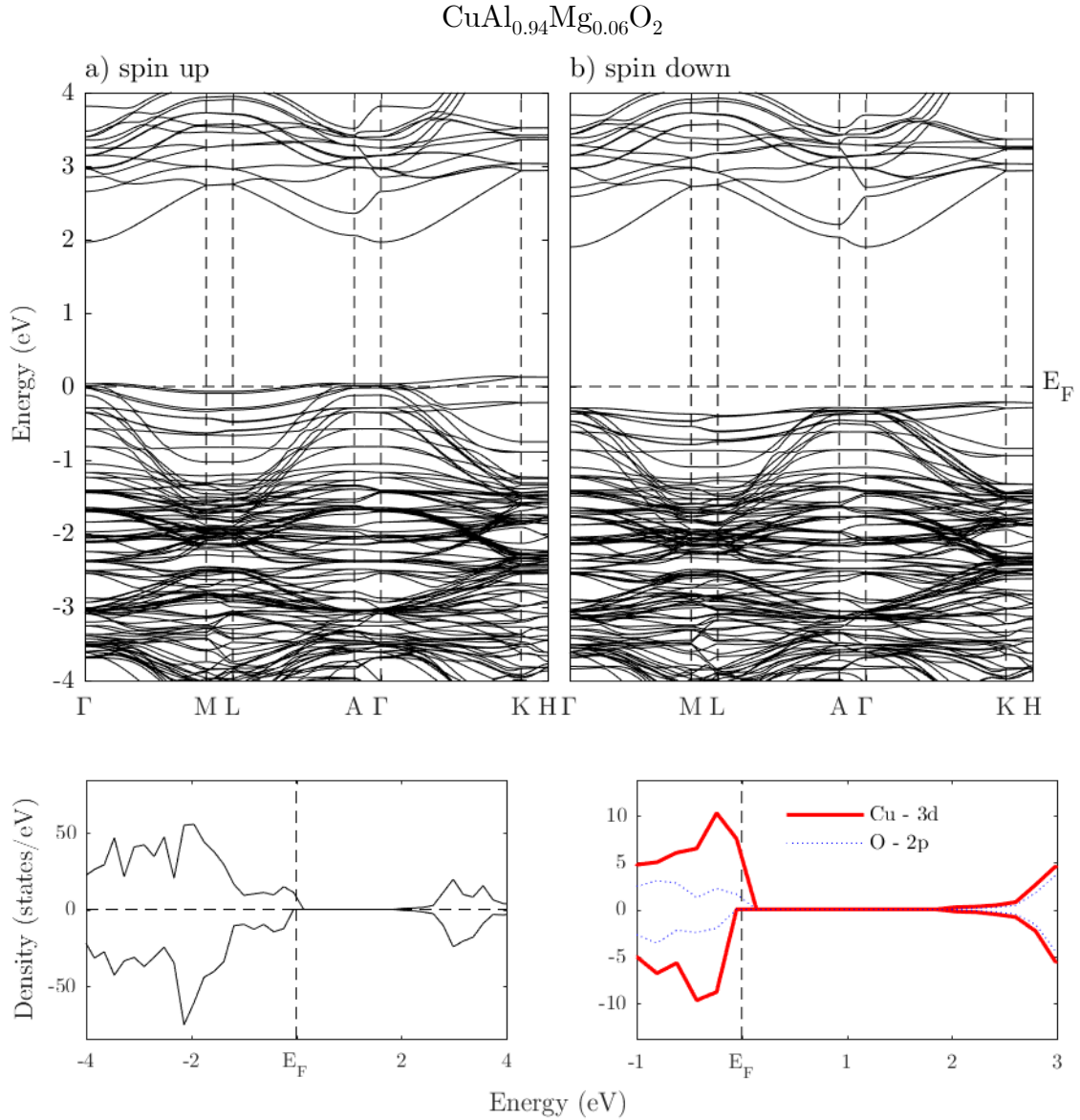


Figure 5.2: The electronic band structure and density of states for Mg-doped CAO using PBE+U, where the Fermi energy,  $E_F$ , is set to zero and is defined as the maximum energy of a valence electron in the ground state.

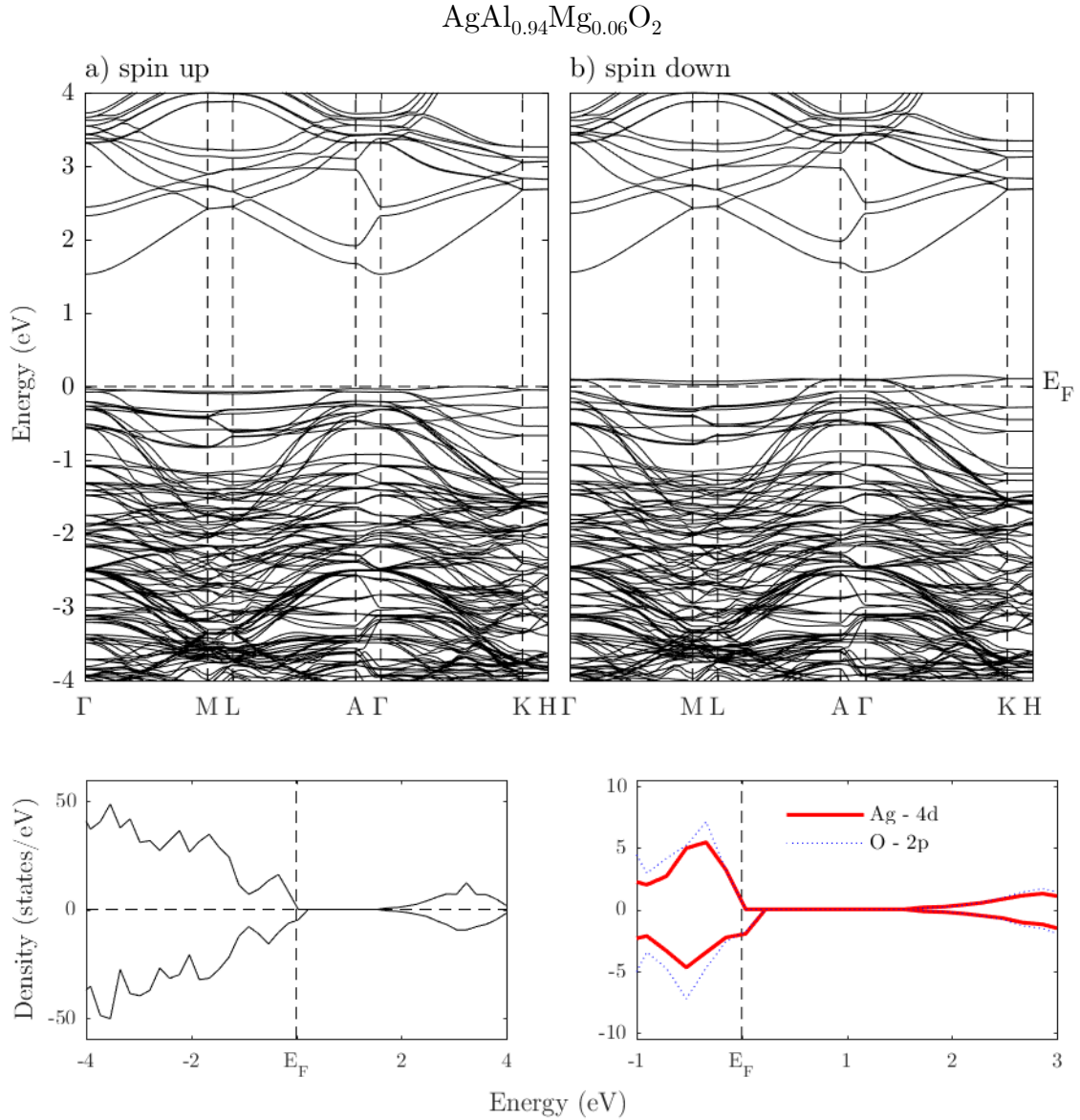


Figure 5.3: The electronic band structure and density of states for Mg-doped AAO using PBE+U, where the Fermi energy,  $E_F$ , is set to zero and is defined as the maximum energy of a valence electron in the ground state.

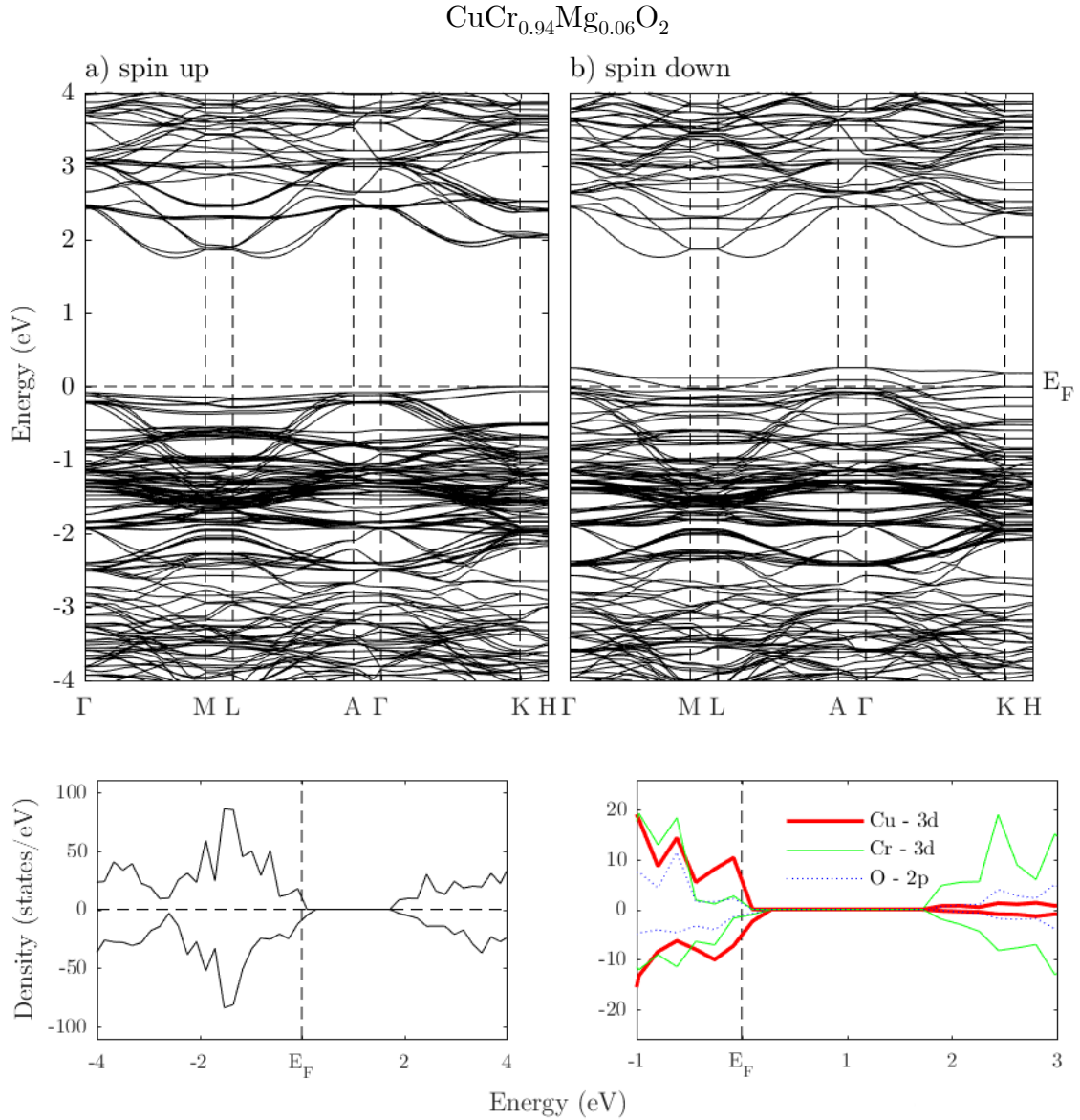


Figure 5.4: The electronic band structure and density of states for Mg-doped CCO using PBE+U, where the Fermi energy,  $E_F$ , is set to zero and is defined as the maximum energy of a valence electron in the ground state.

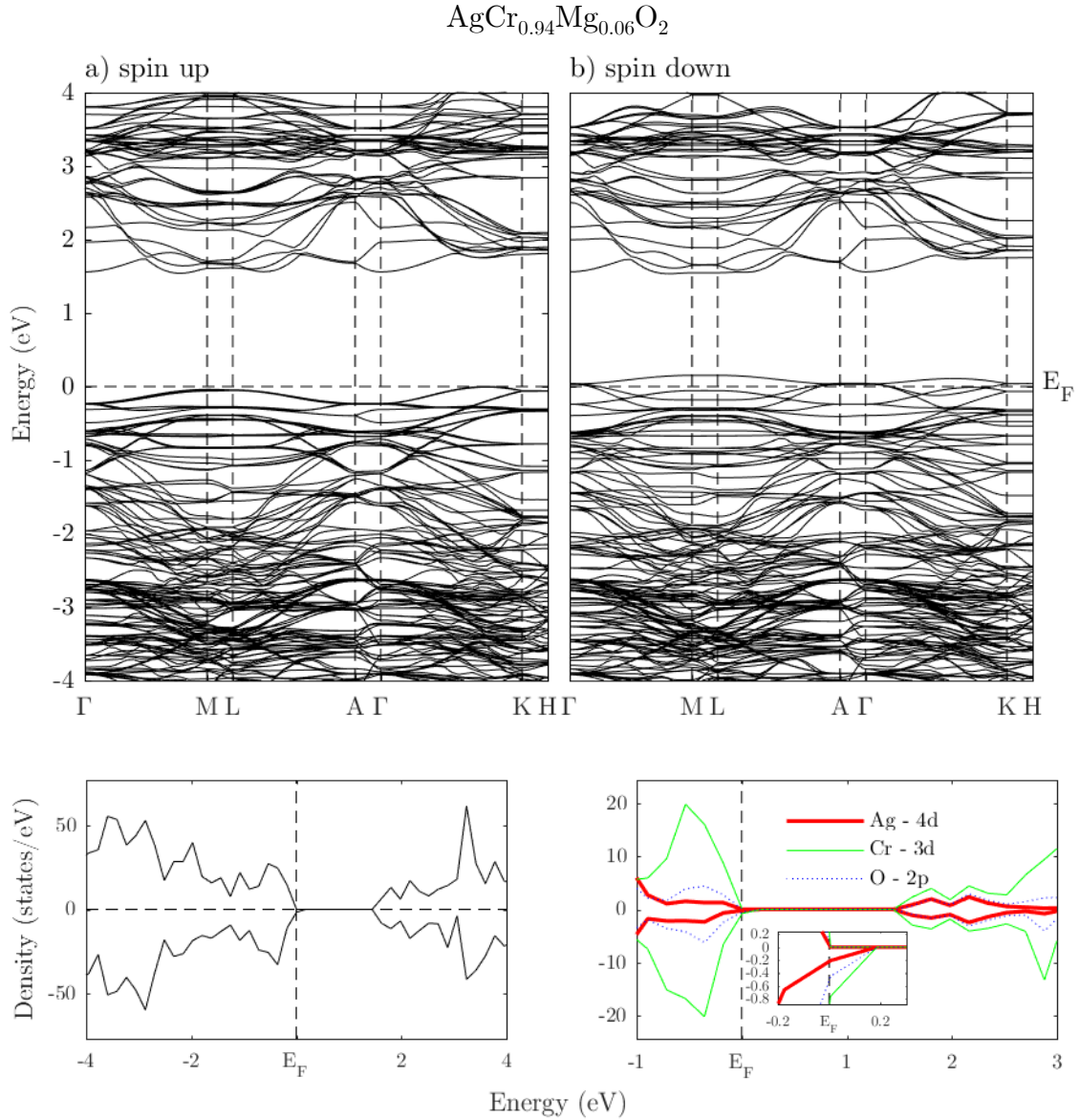


Figure 5.5: The electronic band structure and density of states for Mg-doped ACO using PBE+U, where the Fermi energy,  $E_F$ , is set to zero and is defined as the maximum energy of a valence electron in the ground state.

## 5.4. Hole Effective Masses

The average hole effective masses, presented with the other hole effective mass values for Mg-doped XTO in Tab. 5.2, are higher than their counterparts in pristine XTO for XAO and CCO. The hole effective masses also become larger in the [100] and [001] directions and smaller in the [010] direction. For Mg-doped ACO, the trend is reversed, and the overall hole effective mass is lower than in the pristine crystal as a result. In ATO and CCO, the hole effective masses become smaller in the [001] direction than they are in the [100] direction. These trends support hole conduction still being favorable in the  $a - b$  plane, but in the [010] direction instead of the [100] direction as in the pristine crystals, except with ACO, where the hole effective masses are lowest in the [001] direction, indicating that hole conduction may be more favorable parallel to the O–X–O dumbbells.

Table 5.2: The hole effective masses for Mg-doped XTO using the supercell scheme, in units of  $m_e$ , the free electron mass.

	K $\rightarrow$ $\Gamma$ [100]	[010]	K $\rightarrow$ H [001]	avg.
CuAl <sub>0.94</sub> Mg <sub>0.06</sub> O <sub>2</sub>	2.62	0.76	3.11	2.16
AgAl <sub>0.94</sub> Mg <sub>0.06</sub> O <sub>2</sub>	8.27	0.34	6.34	4.99
CuCr <sub>0.94</sub> Mg <sub>0.06</sub> O <sub>2</sub>	7.77	0.54	6.04	4.78
AgCr <sub>0.94</sub> Mg <sub>0.06</sub> O <sub>2</sub>	0.92	1.88	0.53	1.11

Despite the increase in hole effective masses in XTO as a result of Mg doping, it may still be the case that conductivity is increased overall. Liu *et al.* report [84] that hole concentration in pristine CAO increases from  $3.52 \times 10^{16}$  to  $1.79 \times 10^{18} \text{ cm}^{-3}$  in CuAl<sub>0.94</sub>Mg<sub>0.06</sub>O<sub>2</sub>. Considering the highly ionic character of the charge density, it may be reasonable to assume that the mean scattering time for charge carriers in Mg-doped CAO may be largely unchanged from the pristine crystal, such that the two-order-of-magnitude increase in hole concentration more than makes up for a nearly two-fold increase in hole effective masses. Referring back

to Eqn. 2.3.9, the potential increase in conductivity is

$$\sigma_{\text{doped}}/\sigma = 33.20. \quad (5.4.1)$$

## 5.5. Optical Properties

The static dielectric constants and refractive indices in Mg-doped XAO, which are shown in Tab. 5.3 are lower than those in the pristine crystals by about 1 – 2%.

Table 5.3: The static dielectric constants,  $\epsilon_{\infty}$ , and refractive indices,  $n$ , in the directions a, b, and c, corresponding to the primitive lattice vectors  $\mathbf{b}_1$ ,  $\mathbf{b}_2$ , and  $\mathbf{b}_3$ , of Mg-doped XAO in the PBE+U method.

	$\epsilon_{\infty}^a$	$\epsilon_{\infty}^b$	$\epsilon_{\infty}^c$	$\epsilon_{\infty}^{\text{avg}}$	$n_a$	$n_b$	$n_c$	$n_{\text{avg}}$
CuAl <sub>0.94</sub> Mg <sub>0.06</sub> O <sub>2</sub>	5.3057	5.3188	4.4073	5.0106	2.3034	2.3036	2.0994	2.2364
AgAl <sub>0.94</sub> Mg <sub>0.06</sub> O <sub>2</sub>	5.3554	5.3536	5.4348	5.3813	2.3142	2.3138	2.3313	2.3198

The optical properties obtained for Mg-doped CAO are displayed in Fig. 5.6 and show a new local maximum at approximately 5.0 eV for the in-plane component of the complex dielectric function. This local maximum in the optical properties may correspond to the two local maximums in the total DOS presented in Fig. 5.2 on either side of the band gap which are separated by roughly 5.0 eV, indicating that those states may share the same wave number and be related via a direct transition across the band gap. Otherwise, the results match those of pristine CAO. Figure 5.7 presents the optical properties for Mg-doped AAO, which are identical to the pristine crystal with the exception of a slight decrease in the maximum values of the in-plane component of the complex dielectric function. There are no optical properties to present for Mg-doped XCO due to problems with the calculations that persisted until the printing of this work and led to erroneous results. It may be the case that 6.25% Mg doping in XCO may be beyond the solubility limit for Mg in XCO. Although Sun *et al.* report that 7.0% Mg doping in layers of CCO stacked on both sides of a thin Ag layer results in improvement in the

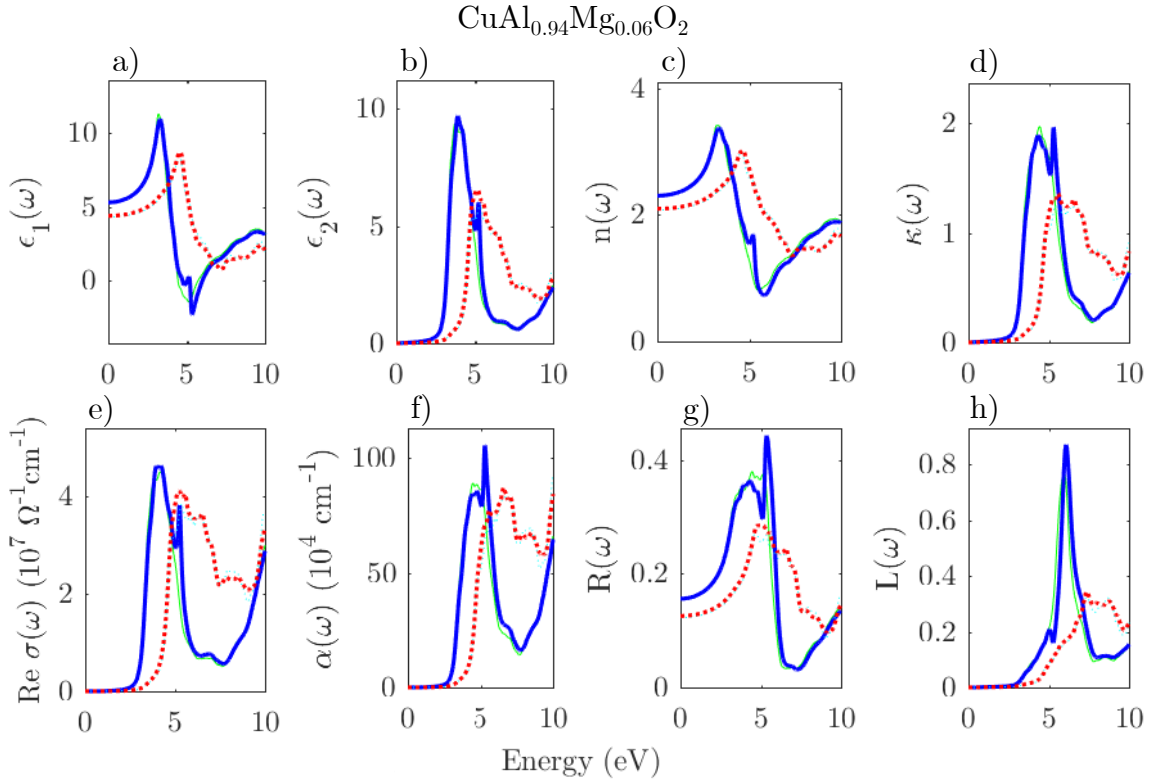


Figure 5.6: Frequency dependence of the a) real component of the complex dielectric function, b) imaginary component of the complex dielectric function, c) refractive index, d) extinction coefficient, e) optical conductivity, f) absorption coefficient, g) reflectivity, and e) loss function of Mg-doped CAO. The in-plane components are drawn as a thick blue line and the perpendicular component is drawn by a thick red dashed line. The pristine supercell results are plotted in the same panels for comparison, with the in-plane components drawn as a thin green line and a thin cyan dashed line for the perpendicular component.

optoelectronic character [11], Maignan *et al.* report that the saturation level of Mg in CCO is much closer to 1.0% [85], indicating that the 6.25% Mg doping in this study may be beyond the saturation level for bulk XCO and is the source of the problem in calculating the optical properties of Mg-doped XCO.

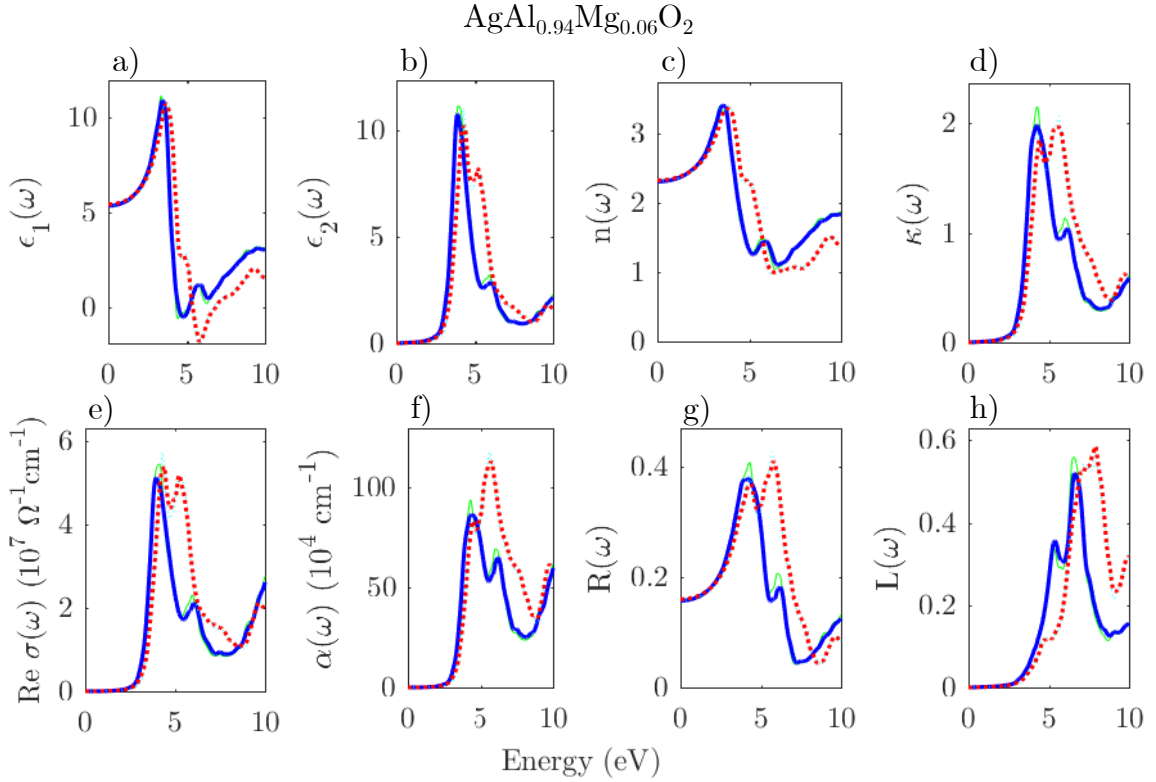


Figure 5.7: Frequency dependence of the a) real component of the complex dielectric function, b) imaginary component of the complex dielectric function, c) refractive index, d) extinction coefficient, e) optical conductivity, f) absorption coefficient, g) reflectivity, and h) loss function of Mg-doped AAO. The in-plane components are drawn as a thick blue line and the perpendicular component is drawn by a thick red dashed line. The pristine supercell results are plotted in the same panels for comparison, with the in-plane components drawn as a thin green line and a thin cyan dashed line for the perpendicular component.

## 5.6. Summary of Results

Although the hole effective masses increase in Mg-doped XAO, the increase in charge carriers that results from Mg doping may still result in an increase in conductivity for XAO, and the optical properties remaining unchanged in the visible portion of the spectrum suggests that the optical properties are only negligibly affected by the Mg-dopant. Although the same rationale concerning the hole effective masses and charge carriers may be true in XCO, the calculations of the optical properties remained problematic up to the printing of this work, and so the

effects of Mg doping on the optical properties of XCO remains inconclusive.

## 6. CONCLUSIONS AND PERSPECTIVES

An introduction to the necessary physics of basic DFT in the PAW method using various approximations for the exchange and correlation energy functionals as well as the extended physics that are associated with the many properties that may be derived from the total ground state charge densities obtained through DFT have been presented. The implementation of DFT by the VASP code has also been discussed, along with the various pieces of software associated with the post-processes in determining many of the derived quantities presented in this work, such as the determination of screened Hubbard corrections for XTO using the ATOM code, the equation of state fitting for optimizing structural parameters by minimizing the total ground state energy via the Gibbs2 code, and the method of band unfolding as implemented by the BandUP code.

All XAO polymorphs have been optimized using PBE, and the optimized lattice constants agree very well with the available experimental results. The adoption of the PBE+U method for the study of 2H XTO as well the simple AFM configuration for XCO has been justified by demonstrating that these configurations correspond to the lowest ground state total energies and also give the most semiconductor-like behavior. The PBE+U optimized lattice parameters and direct band gaps compare favorably to the experimental results from literature. Hole effective masses and optical properties have been determined for XTO, and new predictions are offered in this work concerning XCO hole effective masses and ACO optical properties that may benefit the literature. The hole effective masses, strong X- $d$  and O- $2p$  contributions to the density of states in XTO, and optical properties support a model of hole conduction that is perpendicular to the O–X–O dumbbells.

Native defects in the form of 6.25% X and 3.13% O vacancies have been investigated from the perspective of the changes in structural properties, emergence of shallow acceptor states, changes in the band gap, specific state contributions to

the DOS, and changes in hole effective masses and optical properties. X vacancies resulted in the O anions near the vacancy site moving closer to the T planes. The changes to the charge density result in the emergence of shallow acceptor states which should promote hole conduction, however, there is also a slight increase to the hole effective masses, and without information on how the carrier concentration is affected by the X vacancy it is not possible to evaluate the change in conductivity. Although there is a slight increase in the static dielectric constants and refractive indices, the optical properties of XTO remain largely unaffected indicating that the transparent character is preserved. O vacancies, however, only promote shallow acceptor states in one spin channel of XCO, likely the result of the abundance and dominance of Cr-3*d* states along with the Cu(Ag)-3(4)*d* states surrounding the band gap, but also decrease the band gap in the other spin channel. In all cases the band gap decreases overall, drastically so in AAO and to a lesser degree in CAO, due to the three Al ions near the O vacancy site retaining one electron each, raising the energy of those states and introducing more Al-3*p* states to the immediate vicinity of the band gap. In all cases of the introduction of O vacancies, the in-plane components of the optical properties experience a slight decrease in their local maxima, as well as the emergence of a strong oscillation at around 2.0(1.5) eV for XAO(XCO). This oscillation is localized around the optical transition in all materials and likely inhibits transparent behavior in XTO. For this reason, this work predicts that a growth environment slightly deficient in X but saturated in O may benefit the conductivity in XTO.

Lastly, the effects of 6.25% Mg doping on the structural, electronic, and optical properties have been presented and discussed. The defect site has the effect of pushing the O and X ions in the immediate vicinity away from the T planes. Similarly to X vacancies, Mg doping promotes shallow acceptor states in XTO and has a negligible effect on the visible portion of the optical properties for XAO.

Although the hole effective masses are also predicted to generally increase by a factor of two as compared to the pristine crystal, the increase in hole concentration of Mg-doped CAO over its pristine counterpart suggests that the conductivity in Mg-doped CAO still increases by a factor of 33.20, and thus conductivity may increase for all XTO despite the rise in hole effective masses. Thus, 6.25% Mg doping is expected to further increase the conductivity in XTO in addition to promoting X vacancies and discouraging O vacancies.

Concerning the future outlook for this work, it is proposed that a more thorough investigation concerning the magnetic ordering of XCO be undertaken, in order to understand the shortcomings of the simple AFM configuration used in this work, from the perspective of adopting a supercell and implementing its study using the non-colinear version of the VASP code and scrutinizing the electronic structure against the simple model. Since band gaps are still too underestimated in the case of XCO, even within the PBE+U approach adopted here, it is suggested that a hybrid functional be used to improve the description of pristine XCO as well as the defective and doped XTOs. It was determined during the final stages of this work that rigorous estimates of the acceptor state binding energies could be determined by identifying states deep within the valence bands of the pristine XTO crystal with strong *s* character that would not be affected by the introduction of defects and dopants and comparing the changes in Fermi energy with regard to that deep state across pristine and defect systems. Adding the maximum acceptor state energy to the change in Fermi energy across systems (all calculated at the same *k*-point) should then account for the binding energy of the acceptor state. All of the required parameters needed to calculate defect and impurity formation energies should be available after estimating the chemical potential of each element within the pristine, defect, and doped systems. Additionally, a study on the effects of different concentrations of Mg doping on XCO should be conducted for the purposes of

evaluating the saturation level of the Mg dopant in the bulk crystal from the perspective of first principles calculations.

## REFERENCES

- [1] K. H. L. Zhang, K. Xi, M. G. Blamire and R. G. Egdell, *P-type transparent conducting oxides*, Journal of Physics: Condensed Matter **28** (2016) (38), pp. 383002–19
- [2] N. Wolff, D. Klimm and D. Siche, *Thermodynamic investigations on the growth of CuAlO<sub>2</sub> delafossite crystals*, Journal of Solid State Chemistry **258** (2017) (September 2017), pp. 495–500
- [3] D. Xiong, X. Zeng, W. Zhang, H. Wang, X. Zhao, W. Chen and Y.-B. Cheng, *Synthesis and Characterization of CuAlO<sub>2</sub> and AgAlO<sub>2</sub> Delafossite Oxides through Low-Temperature Hydrothermal Methods*, Inorganic Chemistry **53** (2014) (8), pp. 4106–4116
- [4] A. P. Amrute, Z. Łodziana, C. Mondelli, F. Krumeich and J. Pérez-Ramírez, *Solid-state chemistry of cuprous delafossites: Synthesis and stability aspects*, Chemistry of Materials **25** (2013) (21), pp. 4423–4435
- [5] D. Xiong, H. Wang, W. Zhang, X. Zeng, H. Chang, X. Zhao, W. Chen and Y.-B. Cheng, *Preparation of p-type AgCrO<sub>2</sub> nanocrystals through low-temperature hydrothermal method and the potential application in p-type dye-sensitized solar cell*, Journal of Alloys and Compounds **642** (2015) (0), pp. 104–110
- [6] Hiroshi Kawazoe, Masahiro Yasukawa, Hiroyuki Hyodo, Masaaki Kurita, Hiroshi Yanagi and Hideo Hosono, *P-type electrical conduction in transparent thin films of CuAlO<sub>2</sub>*, Letters to Nature **389** (1997), pp. 939–942
- [7] H. Yanagi, S.-I. Inoue, K. Ueda and H. Kawazoe, *Electronic structure and optoelectronic properties of transparent p-type conducting CuAlO<sub>2</sub>*, Journal of Applied Physics **88** (2000) (7), pp. 4159–4163
- [8] M. Diantoro, P. E. Yuwita, D. Olenka and Nasikhudin, *Fabrication of CuAl<sub>1-x</sub>M<sub>x</sub>O<sub>2</sub> (M = Fe, Cr)/Ni film delafossite compounds using spin coating and their microstructure and dielectric constant*, in *AIP Conference Proceedings* (2014), vol. 1617, pp. 170–174
- [9] Z. Deng, X. Zhu, R. Tao, W. Dong and X. Fang, *Synthesis of CuAlO<sub>2</sub> ceramics using sol-gel*, Materials Letters **61** (2007) (3), pp. 686–689
- [10] A. N. Banerjee, R. Maity and K. K. Chattopadhyay, *Preparation of p-type transparent conducting CuAlO<sub>2</sub> thin films by reactive DC sputtering*, Materials Letters **58** (2004) (1-2), pp. 10–13
- [11] H. Sun, M. A. P. Yazdi, S.-C. Chen, C.-K. Wen, F. Sanchette and A. Billard, *Ag composition gradient CuCr<sub>0.93</sub>Mg<sub>0.07</sub>O<sub>2</sub>/Ag/CuCr<sub>0.93</sub>Mg<sub>0.07</sub>O<sub>2</sub> coatings with improved p-type optoelectronic performances*, Journal of Materials Science **52** (2017) (19), pp. 11537–11546

- [12] D. O. Scanlon and G. W. Watson, *Conductivity Limits in CuAlO<sub>2</sub> from Screened-Hybrid Density Functional Theory*, Journal of Physical Chemistry Letters **1** (2010) (21), pp. 3195–3199
- [13] J. Tate, H. L. Ju, J. C. Moon, A. Zakutayev, A. P. Richard, J. Russell and D. H. McIntyre, *Origin of p-type conduction in single-crystal CuAlO<sub>2</sub>*, Physical Review B - Condensed Matter and Materials Physics **80** (2009) (16), pp. 165206–165214
- [14] J. Pellicer-Porres, A. Segura, C. Ferrer-Roca, A. Polian, P. Munsch and D. Kim, *XRD and XAS structural study of CuAlO<sub>2</sub> under high pressure*, Journal of Physics: Condensed Matter **25** (2013) (11), pp. 115406–10
- [15] R. Wei, X. Tang, L. Hu, J. Yang, X. Zhu, W. Song, J. Dai, X. Zhu and Y. Sun, *Facile chemical solution synthesis of p-type delafossite Ag-based transparent conducting AgCrO<sub>2</sub> films in an open condition*, J. Mater. Chem. C **5** (2017) (8), pp. 1885–1892
- [16] A. H. Reshak, *First Principle Calculations of Transition Metal Oxide , AgAlO<sub>2</sub>, as Active Photocatalyst : Sustainable Alternative Sources of Energy*, International Journal of Electrochemical Science **8** (2013), pp. 9371–9383
- [17] K. Momma and F. Izumi, *VESTA 3 for three-dimensional visualization of crystal, volumetric and morphology data*, Journal of Applied Crystallography **44** (2011) (6), pp. 1272–1276
- [18] Q. J. Liu, Z. T. Liu, L. P. Feng, H. Tian, W. T. Liu and F. Yan, *Density functional theory study of 3R- and 2H-CuAlO<sub>2</sub> under pressure*, Applied Physics Letters **97** (2010) (14), pp. 141917–141920
- [19] F. A. Benko and F. P. Koffyberg, *Opto-electronic properties of CuAlO<sub>2</sub>*, Journal of Physics and Chemistry of Solids **45** (1984) (1), pp. 57–59
- [20] J. Pellicer-Porres, A. Segura, A. S. Gilliland, A. Muñoz, P. Rodríguez-Hernández, D. Kim, M. S. Lee and T. Y. Kim, *On the band gap of CuAlO<sub>2</sub> delafossite*, Applied Physics Letters **88** (2006) (18), pp. 181904–181907
- [21] J. R. Smith, T. H. Van Steenkiste and X. G. Wang, *Thermal photocatalytic generation of H<sub>2</sub> over CuAlO<sub>2</sub> nanoparticle catalysts in H<sub>2</sub>O*, Physical Review B - Condensed Matter and Materials Physics **79** (2009) (4), pp. 2–5
- [22] T. Suriwong, T. Thongtem and S. Thongtem, *Thermoelectric and optical properties of CuAlO<sub>2</sub> synthesized by direct microwave heating*, Current Applied Physics **14** (2014) (9), pp. 1257–1262
- [23] C. K. Ghosh, D. Sarkar, M. K. Mitra and K. K. Chattopadhyay, *Electronic structure and optical properties of CuAlO<sub>2</sub> under biaxial strain*, Journal of Physics: Condensed Matter **24** (2012), pp. 235501–9

- [24] K. C. Bhamu, R. Khenata, S. A. Khan, M. Singh and K. R. Priolkar, *Electronic, Optical and Thermoelectric Properties of 2H-CuAlO<sub>2</sub>: A First Principles Study*, Journal of Electronic Materials **45** (2016) (1), pp. 615–623
- [25] W. C. Sheets, E. S. Stampler, M. I. Bertoni, M. Sasaki, T. J. Marks, T. O. Mason and K. R. Poeppelmeier, *Silver delafossite oxides*, Inorganic Chemistry **47** (2008) (7), pp. 2696–2705
- [26] S. Ouyang, N. Kikugawa, D. Chen, Z. Zou and J. Ye, *A Systematical Study on Photocatalytic Properties of AgMO<sub>2</sub> (M = Al, Ga, In): Effects of Chemical Compositions, Crystal Structures, and Electronic Structures*, The Journal of Physical Chemistry C **113** (2009) (4), pp. 1560–1566
- [27] H. F. Jiang, C. Y. Gui, Y. Y. Zhu, D. J. Wu, S. P. Sun, C. Xiong and X. B. Zhu, *First-principle study on O – A – O dumbbell of delafossite crystal*, Journal of Alloys and Compounds **582** (2014), pp. 64–68
- [28] K. Bhamu and K. Priolkar, *Electronic and optical properties of AgAlO<sub>2</sub>: A first-principles study*, Materials Chemistry and Physics **190** (2017), pp. 114–119
- [29] S. Ouyang and J. Ye,  *$\beta$ -AgAl<sub>1-x</sub>Ga<sub>x</sub>O<sub>2</sub> Solid-Solution Photocatalysts: Continuous Modulation of Electronic Structure toward High-Performance Visible-Light Photoactivity*, Journal of the American Chemical Society **133** (2011), pp. 7757–7763
- [30] O. Crottaz and F. Kubel, *Crystal structure of copper(I) chromium(III) oxide, 3R-CuCrO<sub>2</sub>*, Zeitschrift für Kristallographie - Crystalline Materials **211** (1996) (7)
- [31] R. Nagarajan, A. D. Draeseke, A. W. Sleight and J. Tate, *P-type conductivity in CuCr<sub>1-x</sub>Mg<sub>x</sub>O<sub>2</sub> films and powders*, Journal of Applied Physics **89** (2001) (12), pp. 8022–8025
- [32] M. O’Sullivan, P. Stamenov, J. Alaria, M. Venkatesan and J. M. Coey, *Magnetoresistance of CuCrO<sub>2</sub>-based delafossite films*, Journal of Physics: Conference Series **200** (2010) (SECTION 5), pp. 6–10
- [33] D. O. Scanlon and G. W. Watson, *Understanding the p-type defect chemistry of CuCrO<sub>2</sub>*, Journal of Materials Chemistry **21** (2011) (11), p. 3655
- [34] A. Barnabé, Y. Thimont, M. Lalanne, L. Presmanes and P. Tailhades, *P-Type conducting transparent characteristics of delafossite Mg-doped CuCrO<sub>2</sub> thin films prepared by RF-sputtering*, J. Mater. Chem. C **3** (2015) (23), pp. 6012–6024
- [35] Y. Xu, G. Z. Nie, D. Zou, J. W. Tang and Z. Ao, *N-Mg dual-acceptor co-doping in CuCrO<sub>2</sub> studied by first-principles calculations*, Physics Letters, Section A **380** (2016) (45), pp. 3861–3865

- [36] S. H. Lim, S. Desu and A. C. Rastogi, *Chemical spray pyrolysis deposition and characterization of p-type  $\text{CuCr}_{1-x}\text{Mg}_x\text{O}_2$  transparent oxide semiconductor thin films*, Journal of Physics and Chemistry of Solids **69** (2008) (8), pp. 2047–2056
- [37] M. Frontzek, G. Ehlers, A. Podlesnyak, H. Cao, M. Matsuda, O. Zaharko, N. Aliouane, S. Barilo and S. V. Shiryaev, *Magnetic structure of  $\text{CuCrO}_2$ : a single crystal neutron diffraction study*, Journal of Physics: Condensed Matter **24** (2012) (1), pp. 016004–8
- [38] C. Kittel, *Introduction to Solid State Physics*, 8 ed. (Wiley, 2010)
- [39] A. Kokalj, *XCrySDen - a new program for displaying crystalline structures and electron densities*, J. Mol. Graph. Model. **17** (2000) (3-4), pp. 176–179, 215–216
- [40] A. Kokalj, *Computer graphics and graphical user interfaces as tools in simulations of matter at the atomic scale*, Computational Materials Science **28** (2003) (2), pp. 155–168
- [41] A. F. J. Levi, *Applied Quantum Mechanics*, 2 ed. (Cambridge University Press, 2006)
- [42] F. Giustino, *Materials Modeling using Density Functional Theory: Properties and Predictions*, 1 ed. (Oxford University Press, 2014)
- [43] J. D. Jackson, *Classical Electrodynamics*, 3 ed. (Wiley, 2014)
- [44] P. Hohenberg and W. Kohn, *Inhomogeneous electron gas*, Physical Review B **136** (1964), pp. 864–871
- [45] W. Kohn and L. J. Sham, *Self-consistent equations including exchange and correlation effects*, Physical Review **140** (1965) (4A), pp. 1133–1138
- [46] J. C. Slater, *A simplification of the Hartree-Fock method*, Physical Review **81** (1951) (3), pp. 385–390
- [47] D. C. Langreth and M. J. Mehl, *Easily implementable nonlocal exchange-correlation energy functional*, Physical Review Letters **47** (1981) (6), pp. 446–450
- [48] J. P. Perdew, K. Burke and M. Ernzerhof, *Generalized gradient approximation made simple*, Physical Review Letters **77** (1996) (18), pp. 3865–3868
- [49] V. I. Anisimov, J. Zaanen and O. K. Andersen, *Band theory and Mott insulators: Hubbard  $U$  instead of Stoner  $I$* , Physical Review B **44** (1991) (3), pp. 943–954
- [50] J. Heyd, G. E. Scuseria and M. Ernzerhof, *Hybrid functionals based on a screened Coulomb potential*, Journal of Chemical Physics **118** (2003) (18), pp. 8207–8215

- [51] F. Tran and P. Blaha, *Accurate band gaps of semiconductors and insulators with a semilocal exchange-correlation potential*, Physical Review Letters **102** (2009) (22), pp. 5–8
- [52] A. D. Becke and M. R. Roussel, *Exchange holes in inhomogeneous systems: A coordinate-space model*, Physical Review A **39** (1989) (8), pp. 3761–3767
- [53] G. Kresse and J. Hafner, *Ab initio molecular dynamics for liquid metals*, Physical Review B **47** (1993) (1), pp. 558–561
- [54] G. Kresse and J. Hafner, *Ab initio molecular-dynamics simulation of the liquid-metal–amorphous-semiconductor transition in germanium*, Physical Review B **49** (1994) (20), pp. 14251–14269
- [55] G. Kresse and J. Furthmüller, *Efficient iterative schemes for ab initio total-energy calculations using a plane-wave basis set*, Physical Review B **54** (1996) (16), pp. 11169–11186
- [56] G. Kresse and J. Furthmüller, *Efficiency of ab-initio total energy calculations for metals and semiconductors using a plane-wave basis set*, Computational Materials Science **6** (1996) (1), pp. 15–50
- [57] P. E. Blöchl, *Projector augmented-wave method*, Physical Review B **50** (1994) (24), pp. 17953–17979
- [58] D. R. Hamann, *Generalized norm-conserving pseudopotentials*, Physical Review B **40** (1989) (5), pp. 2980–2987
- [59] R. Car and M. Parrinello, *Unified Approach for Molecular Dynamics and Density-Functional Theory*, Physical Review Letters **55** (1985) (22), pp. 2471–2474
- [60] P. Pulay, *Convergence acceleration of iterative sequences. the case of scf iteration*, Chemical Physics Letters **73** (1980) (2), pp. 393–398
- [61] F. Birch, *Finite elastic strain of cubic crystals*, Physical Review **71** (1947) (11), pp. 809–824
- [62] F. D. Murnaghan, *The Compressibility of Media under Extreme Pressures*, Proceedings of the National Academy of Sciences **30** (1944) (9), pp. 244–247
- [63] P. V. Medeiros, S. Stafström and J. Björk, *Effects of extrinsic and intrinsic perturbations on the electronic structure of graphene: Retaining an effective primitive cell band structure by band unfolding*, Physical Review B - Condensed Matter and Materials Physics **89** (2014) (4), pp. 041407–4
- [64] P. V. Medeiros, S. S. Tsirkin, S. Stafström and J. Björk, *Unfolding spinor wave functions and expectation values of general operators: Introducing the unfolding-density operator*, Physical Review B - Condensed Matter and Materials Physics **91** (2015) (4), pp. 041116–5

- [65] T. B. Boykin and G. Klimeck, *Practical application of zone-folding concepts in tight-binding calculations*, Physical Review B - Condensed Matter and Materials Physics **71** (2005) (11)
- [66] O. Rubel, A. Bokhanchuk, S. J. Ahmed and E. Assmann, *Unfolding the band structure of disordered solids: From bound states to high-mobility Kane fermions*, Physical Review B - Condensed Matter and Materials Physics **90** (2014) (11), pp. 1–8
- [67] F. Wooten, *Optical Properties of Solids*, 1 ed. (Academic Press, 1972)
- [68] M. Gajdoš, K. Hummer, G. Kresse, J. Furthmüller and F. Bechstedt, *Linear optical properties in the projector-augmented wave methodology*, Physical Review B - Condensed Matter and Materials Physics **73** (2006) (4), pp. 1–9
- [69] G. Kresse and J. Hafner, *Norm-conserving and ultrasoft pseudopotentials for first-row and transition elements*, Journal of Physics: Condensed Matter **6** (1994) (40), pp. 8245–8357
- [70] G. Kresse and D. Joubert, *From ultrasoft pseudopotentials to the projector augmented-wave method*, Physical Review B **59** (1999) (3), pp. 1758–1775
- [71] J. M. Soler, E. Artacho, J. D. Gale, A. García, J. Junquera, P. Ordejón and D. Sánchez-Portal, *The SIESTA method for ab initio order-N materials*, Journal of Physics: Condensed Matter **2745** (2002) (14), pp. 2745–2779
- [72] A. Janotti, D. Segev and C. G. Van De Walle, *Effects of cation d states on the structural and electronic properties of III-nitride and II-oxide wide-band-gap semiconductors*, Physical Review B - Condensed Matter and Materials Physics **74** (2006) (4), pp. 1–9
- [73] T. Ishiguro, A. Kitazawa, N. Mizutani and M. Kato, *Single-Crystal Growth and Crystal Structure Refinement of  $\text{CuAlO}_2$* , Journal of Solid State Chemistry **40** (1981), pp. 170–174
- [74] A. Otero-De-La-Roza and V. Luaña, *Gibbs2: A new version of the quasi-harmonic model code. I. Robust treatment of the static data*, Computer Physics Communications **182** (2011) (8), pp. 1708–1720
- [75] A. Otero-De-La-Roza, D. Abbasi-Pérez and V. Luaña, *Gibbs2: A new version of the quasiharmonic model code. II. Models for solid-state thermodynamics, features and implementation*, Computer Physics Communications **182** (2011) (10), pp. 2232–2248
- [76] A. V. Krukau, O. A. Vydrov, A. F. Izmaylov and G. E. Scuseria, *Influence of the exchange screening parameter on the performance of screened hybrid functionals*, Journal of Chemical Physics **125** (2006) (22), pp. 224106–224111

- [77] D. O. Scanlon, B. J. Morgan and G. W. Watson, *Modeling the polaronic nature of p-type defects in Cu<sub>2</sub>O: The failure of GGA and GGA+U*, The Journal of Chemical Physics **131** (2009) (12), p. 124703
- [78] B. J. Ingram, T. O. Mason, R. Asahi, K. T. Park and A. J. Freeman, *Electronic structure and small polaron hole transport of copper aluminate*, Physical Review B - Condensed Matter and Materials Physics **64** (2001) (15), pp. 1551141–1551147
- [79] R. Laskowski, N. E. Christensen, P. Blaha and B. Palanivel, *Strong excitonic effects in CuAlO<sub>2</sub> delafossite transparent conductive oxides*, Physical Review B - Condensed Matter and Materials Physics **79** (2009) (16), pp. 1–7
- [80] Q.-J. Liu, Z. Jiao, F.-S. Liu and Z.-T. Liu, *Influences of S, Se, Te and Po substitutions on structural, electronic and optical properties of hexagonal CuAlO<sub>2</sub> using GGA and B3LYP functionals*, Physical Chemistry Chemical Physics **18** (2016), pp. 14317–14322
- [81] K. Capelle, *A bird's-eye view of density-functional theory* (2006), URL: <http://arxiv.org/abs/cond-mat/0211443>
- [82] J. P. Perdew, *Climbing the ladder of density functional approximations*, MRS Bulletin **38** (2013) (9), pp. 743–750
- [83] T. F. T. Cerqueira, S. Lin, M. Amsler, S. Goedecker, S. Botti and M. a. L. Marques, *Identification of Novel Cu, Ag, and Au Ternary Oxides from Global Structural Prediction*, Chemistry of Materials **27** (2015) (13), pp. 4562–4573
- [84] R. Liu, Y. Li, B. Yao, Z. Ding, Y. Jiang, L. Meng, R. Deng, L. Zhang, Z. Zhang, H. Zhao and L. Liu, *Shallow Acceptor State in Mg-Doped CuAlO<sub>2</sub> and Its Effect on Electrical and Optical Properties: An Experimental and First-Principles Study*, ACS Applied Materials & Interfaces **9** (2017) (14), pp. 12608–12616
- [85] A. Maignan, C. Martin, R. Frésard, V. Eyert, E. Guilmeau, S. Hébert, M. Poienar and D. Pelloquin, *On the strong impact of doping in the triangular antiferromagnet CuCrO<sub>2</sub>*, Solid State Communications **149** (2009) (23-24), pp. 962–967